Year : 2020

RADIATION FIELD CHARACTERISATION IN HOSPITAL THEATRES USING HYBRID PIXEL DETECTOR

Nowak Marie

Nowak Marie, 2020, RADIATION FIELD CHARACTERISATION IN HOSPITAL THEATRES USING HYBRID PIXEL DETECTOR

Originally published at : Thesis, University of Lausanne

Posted at the University of Lausanne Open Archive http://serval.unil.ch
Document URN : urn:nbn:ch:serval-BIB_7502185199351

UNIL | Université de Lausanne
Faculté de biologie et de médecine

Institut de radiophysique

RADIATION FIELD CHARACTERISATION IN HOSPITAL THEATRES USING HYBRID PIXEL DETECTOR

Thèse de doctorat ès sciences de la vie (PhD)

présentée à la

Faculté de biologie et de médecine
de l'Université de Lausanne

par

Marie NOWAK

Master ès Science en physique, Université de Rennes I, Rennes
Master ès Science en physique médicale, Université de Lille I, Lille

Jury de thèse

Prof. Reto Meuli, Président (CHUV – UNIL)
Prof. Francis R. Verdun, Directeur (CHUV – UNIL)
Dr Jérôme Damet, Co-directeur (CHUV – CERN – Université d'Otago, NZ)
Prof. Richard Brenner, Expert (Université d'Uppsala, SE)
Dr Rafael Duran, Expert (CHUV – UNIL)

Lausanne 2020

UNIL | Université de Lausanne
Faculté de biologie et de médecine

Institut de radiophysique

RADIATION FIELD CHARACTERISATION IN HOSPITAL THEATRES USING HYBRID PIXEL DETECTOR

Thèse de doctorat ès sciences de la vie (PhD)

présentée à la

Faculté de biologie et de médecine
de l'Université de Lausanne

par

Marie NOWAK

Master ès Science en physique, Université de Rennes I, Rennes
Master ès Science en physique médicale, Université de Lille I, Lille

Jury de thèse

Prof. Reto Meuli, Président (CHUV – UNIL)
Prof. Francis R. Verdun, Directeur (CHUV – UNIL)
Dr Jérôme Damet, Co-directeur (CHUV – CERN – Université d'Otago, NZ)
Prof. Richard Brenner, Expert (Université d'Uppsala, SE)
Dr Rafael Duran, Expert (CHUV – UNIL)

Lausanne 2020

UNIL | Université de Lausanne
Faculté de biologie et de médecine

Ecole Doctorale
Doctorat ès sciences de la vie

Imprimatur

Vu le rapport présenté par le jury d'examen, composé de

Président·e	Monsieur	Prof.	Reto	**Meuli**
Directeur·trice de thèse	Monsieur	Prof.	Francis	**Verdun**
Co-directeur·trice	Monsieur	Dr	Jérôme	**Damet**
Expert·e·s	Monsieur	Prof.	Richard	**Brenner**
	Monsieur	Dr	Rafael	**Duran**

le Conseil de Faculté autorise l'impression de la thèse de

Madame Marie Simone Yvonne Nowak

Master Sts Mention physique Spécialité physique médicale, Université Rennes I, France

intitulée

Radiation field characterisation in hospital theatres using hybrid pixel detector

Lausanne, le 18 mai 2020

pour le Doyen
de la Faculté de biologie et de médecine

Prof. Niko GELDNER
Directeur de l'Ecole Doctorale

Il y a des mots qui font vivre
Et ce sont des mots innocents
Le mot chaleur, le mot confiance
Amour, justice et le mot liberté
Le mot enfant et le mot gentillesse
Et certains noms de fleurs et
certains noms de fruits
Le mot courage et le mot découvrir
Et le mot frère et le mot camarade
Et certains noms de pays de villages
Et certains noms de femmes et d'amis.

Paul Eluard

Remerciements

Je remercie en premier lieu mon directeur de thèse, le Professeur Francis R. Verdun, pour ses conseils avisés et sa vision sur ce projet. Ses remarques et son expérience m'ont toujours contribué à l'amélioration de mon travail et à son aboutissement. Je remercie également mon co-directeur de thèse, le Docteur Jérôme Damet, sans qui ce projet n'aurait pas vu le jour. Merci d'avoir su mettre à ma disposition toutes les clefs pour réussir, d'avoir toujours cru en moi et de m'avoir guidée à travers toutes les étapes d'un tel travail. Tes conseils, nos discussions scientifiques, tes encouragements, ta disponibilité et les heures passées à relire ce document m'ont permis de mener à bien cette aventure. Merci à Pierre Carbonez, mon superviseur CERN, pour l'accompagnement dont j'ai bénéficié tout au long de ces années et pour son implication. Merci pour ton enthousiasme et ta confiance qui m'ont portée jusqu'à l'aboutissement de ce projet, et ont contribué au plaisir de me rendre au CERN.
Je tiens à remercier les membres de mon jury de thèse et à leur exprimer ma gratitude de m'avoir fait l'honneur d'évaluer ce travail.

Je tiens à remercier chaleureusement toutes les personnes avec qui j'ai eu la chance de travailler, que ce soient mes collègues de l'IRA ou ceux du CERN. Merci de m'avoir tant appris, et permis d'évoluer dans une ambiance professionnelle agréable. Plus particulièrement merci à Laurent Desorgher pour toutes ses simulations, Nicolas Cherbuin pour ses conseils cliniques, à Jérôme Alozy et Lucas Tlustos, d'avoir pris tant de temps à m'expliquer le fonctionnement du détecteur, ou encore appris à coder. Tout cela n'aurait pas été possible sans le Professeur Bochud qui m'a accueillie au sein de l'IRA et sans le Professeur Campbell qui m'a ouvert les portes du groupe Medipix. Merci à vous.
La nuance peut parfois être mince entre contact professionnel et amitié, aussi je voudrais particulièrement remercier mes collègues et amis, qui ont été là tant pour me conseiller lors de ce travail que pour partager de bons moments en dehors du bureau. Merci à Anaïs, Camille, Damien, Josh, Laurent C, Mathieu, Maude, Nick, Patrik, Siria, Valentin, Viros.

Je remercie le Tchoutchougroupe (Anne, Christian, Christine, Chico, David (qui restera pour moi à jamais dans le train Fribourg-Lausanne), Gérard, Marc, Mathieu, Iris, Laurent, Pauline, Thomas, Dimitri, Néjib) pour toutes ces discussions animées, plus ou moins profondes nous en conviendrons, le matin comme le soir. Merci pour ces moments de rire, et de culture, me permettant chaque jour de m'intégrer un peu plus dans ce beau pays qu'est la Suisse.

Je remercie Catherine et Gil, qui comme j'aime à les appeler sont en quelques sorte ma famille d'adoption Genevoise. Je vous remercie d'avoir toujours eu une place pour moi, et accueillie à bras ouvert. Merci pour les repas, pour les discussions, les débriefings de régates, et tellement plus. Je remercie aussi Bastian pour son soutien et pour notre partage d'une passion commune.

Merci à mes amis les plus proches pour leur soutien inconditionnel, et leur écoute (et ils savent à quel point cela peut être chronophage). Merci d'avoir été tant de petites mains tendues qui m'ont aidée à gravir cette montagne. Je remercie plus spécialement Charlotte, Pauline, Bhakti, Lucile et Pierre.
J'aimerais remercier Julien sans qui je n'aurais pas osé me lancer dans ce travail. Merci de m'avoir tant fait découvrir, sur le monde aussi bien que sur mes propres limites, parfois jusqu'à l'évanouissement. Merci pour ces années.

Plus que tout, et avec émotion, je remercie mes parents, Annie et Dominique. Vous avez fait de moi une personne curieuse, et m'avez toujours encouragé à aller au bout de mes idées. Vous avez été là à chaque instant clef de ma vie, et si je peux être fière de cette réussite aujourd'hui, c'est en grande partie grâce à vous. Merci à mon petit frère, Simon, pour savoir égayer chacun des instants de ma vie juste par sa présence. Merci de m'avoir toujours prêté ta console et tant de fois débloquée dans Python. Merci à vous trois pour avoir toujours cru en moi et pour votre soutien tout au long de mes études, mais encore plus particulièrement lors de cette dernière année de thèse. Je remercie aussi mon grand-père, mes oncles, mes tantes, mes cousins, mes cousines, et Caroline pour m'avoir permis de m'épanouir dans un environnement riche et chaleureux, merci pour votre soutien et vos encouragements.

Pour finir, un grand merci à vous tous de m'avoir permis de mener à bien ce projet et de devenir la femme que je suis aujourd'hui.

Institutions & funding

This PhD project took place in the framework of the collaboration between the Institute of Radiation Physics of the Lausanne University Hospital (IRA/CHUV) and the Radiation Protection Group of the Occupational Health & Safety and Environmental Protection Unit at CERN (HSE-RP).

This Project has been funded by the CERN Budget for Knowledge Transfer to Medical Applications

CONTENTS

Abstract

Certain improvements in patient management are reflected in an increase in the use of X-ray imaging, something which significantly contributes to a regular increase in the average annual effective dose per inhabitant. Although early on, medical imaging was used for purely diagnostic purposes, it is now more and more used to guide therapeutic procedures. This poses two problems: on the one hand is patient exposure, in which tissue reactions may appear due to exposure to ionizing radiation, depending on the complexity of the procedure, and on the other hand is staff exposure, who are close to patients and also involved in numerous procedures over the course of the year. To address this, radiation protection for both patients and staff has been the subject of numerous advances, both from a technological and a behavioural point of view.

To limit exposure of a patient's skin, a hardening of the primary radiation is now systematically proposed for interventional radiology or cardiology procedures. While this measure is very effective, it makes it more difficult to predict the primary X-ray spectrum, which is moreover delivered in the form of short pulses.
When interacting with the patient, X-rays diffuse within the tissues and generate secondary radiation (or scattered radiation) which is responsible for exposure to the medical staff. Although the spectral content of the scattered radiation is well documented when using standard radiology spectra (50 - 100 kV; total filtration 2.5 mm Eq. Al), this is much less so for the spectra resulting from the use of highly hardened beams like those used in interventional radiology or cardiology. This situation is particularly critical when we want to accurately estimate the exposure of medical staff during fluoroscopically-guided procedures. While such procedures tend to become more and more complex, they allow replace surgical interventions which might carry more serious patient risks.

Among medical personnel, the majority of people professionally exposed to ionizing radiation receive very low doses which are far below the legal limits. For this category of people, it is entirely acceptable to estimate the radiation exposures with a tolerance which can be wide. This means that current dosimetry resources ensure optimal management of their radiological risk. However, a certain percentage of the personnel is exposed to a dose which approaches or may even exceed current dose limits. This is especially the case for certain operators who may exceed the dose limit for the eye lens if they do not take special precautions. In such a context, it is imperative to have a dosimetric arsenal to improve the estimation of doses. The objective of this work is part of this dynamic.

At first it seemed important to us to better understand the context of clinical exposure situations. To do this, a study was conducted to obtain measures of occupational exposure in hospitals and to compare them with data from the literature. The results of these measurements confirm the

need to better characterise the spectral content of the scattered radiation produced around the patient during fluoroscopy-guided interventions.

The spectral characterisation of the radiation produced by X-ray tubes, especially when they are emitted in the form of short pulses, remains very difficult for several reasons. First, instant fluence generally exceeds the characteristics of commercially available instruments. In addition, it is often necessary to cool the dosimeters with liquid nitrogen to obtain satisfactory spectral resolution.

The innovative aspect of this work is to use a spectral detector to better characterise the scattered radiation spectra produced in the catheterisation room. This detector was originally developed at CERN for tracking particles in the large hadron collider and has also been used to obtain images from prototype spectral CT installations. However, its performance in detecting scattered radiation fields for dosimetry purposes had yet to be assessed. To do this, a complete characterisation of the detector was necessary. This work constitutes the heart of this thesis. It has been the subject of several scientific presentations and one publication. Finally, once the detector was characterized, a study was done to better understand the spatial spectral variation of the radiation produced by the patient during an interventional radiology procedure. The ultimate objective of this work is to be able to improve the dosimetry of the eye lens of operators using fluoroscopy by introducing calibration factors representative of practical situations.

Keywords: energy spectrum, scattered radiation, interventional radiology, hybrid pixel detector, Timepix3, dose.

Résumé

L'amélioration de la prise en charge des patients se traduit par une augmentation de l'utilisation de l'imagerie utilisant les rayons X qui contribue, de manière non négligeable, à une augmentation régulière de la dose efficace annuelle moyenne par habitant. Si au début de son utilisation, l'imagerie médicale était employée à des fins purement diagnostiques, elle est maintenant de plus en plus utilisée pour guider des procédures thérapeutiques ce qui pose deux problèmes : d'une part l'exposition du patient où, selon la complexité de la procédure, des réactions tissulaires liées à l'exposition aux rayonnements ionisants peuvent apparaître et d'autre part l'exposition du personnel qui se trouve à proximité du patient et qui prend en charge de nombreuses procédures durant l'année.

Pour faire face à cette situation, la radioprotection tant du patient que du personnel a fait l'objet de nombreux progrès tant d'un point de vue technologique que d'un point de vue comportemental.

Pour limiter l'exposition de la peau du patient, un durcissement du rayonnement primaire est maintenant systématiquement proposé pour les procédures de radiologie ou cardiologie interventionnelles. Si cette mesure s'avère très efficace, elle rend cependant plus difficile la prédiction du spectre de rayons X primaires qui est en outre délivré sous forme de courtes impulsions.

En interagissant avec le patient les rayons X diffusent au sein des tissus et génèrent un rayonnement secondaire (ou rayonnement diffusé) responsable de l'exposition du personnel. Si le contenu spectral du rayonnement diffusé est bien documenté lors de l'utilisation de spectres standards de radiologie (50 – 100 kV ; filtration totale 2.5 mm Eq. Al), ils le sont beaucoup moins pour les spectres issus de l'utilisation des qualités de faisceau fortement durcis comme ceux utilisés en radiologie ou cardiologie interventionnelles. Cette situation s'avère particulièrement critique lorsque l'on veut estimer avec précision l'exposition du personnel lors de l'exécution de procédures qui tendent à devenir de plus en plus complexes mais qui se substituent à des actes chirurgicaux dont les risques seraient plus importants.

Parmi le personnel soignant, la majorité des personnes professionnellement exposées aux rayonnements ionisants reçoit des doses très faibles qui sont largement en-dessous des limites légales. Pour cette catégorie de personnes il est tout à fait acceptable d'estimer les expositions avec une tolérance qui peut être large. Ainsi, les moyens de dosimétrie actuellement utilisés assurent une prise en charge optimale de leur risque radiologique. En revanche, une fraction de personnel est exposée à des niveaux de doses proches, ou qui peuvent même dépasser les limites de dose actuelles. C'est le cas en particulier de certains opérateurs qui sans précaution particulière peuvent voir la limite de dose au cristallin largement dépassée. Dans un tel contexte il est impératif de se doter d'un arsenal dosimétrique permettant d'améliorer l'estimation des doses. L'objectif de ce travail s'inscrit dans cette dynamique.

Dans un premier temps, il nous a semblé important de mieux connaître le contexte des situations d'exposition cliniques. Pour ce faire, une étude a été menée afin d'obtenir des mesures d'exposition professionnelle en milieu hospitalier et de les comparer aux données de la littérature. Le bilan de ces mesures confirme la nécessité de mieux caractériser le contenu spectral du rayonnement diffusé produit autour du patient lors d'actes guidés par fluoroscopie. La caractérisation spectrale du rayonnement produit par les tubes à rayons X, surtout lorsque ceux-ci sont émis sous la forme de courtes impulsions, reste très difficile pour plusieurs raisons. En premier lieu, la fluence instantanée dépasse généralement les caractéristiques des instruments commercialement disponibles. En outre, il est souvent nécessaire de refroidir les dosimètres à l'azote liquide pour obtenir une résolution spectrale satisfaisante.
L'aspect novateur de ce travail est d'utiliser un détecteur spectral développé au CERN pour le suivi des particules dans le grand collisionneur de hadrons, et qui est aussi utilisé pour l'obtention d'images provenant d'installations prototypes CT spectral, pour mieux caractériser les spectres de rayonnement diffusé produits en salle de cathétérisme. Pour ce faire, une caractérisation complète du détecteur a été nécessaire. Ce travail constitue le cœur de cette thèse. Il a fait l'objet de plusieurs présentations scientifiques ainsi que d'une publication. Enfin, une fois le détecteur caractérisé, une étude visant à mieux comprendre la variation spectrale dans l'espace du rayonnement produit par le patient lors d'un examen standard de radiologie interventionnelle a été entrepris. L'objectif ultime de ce travail étant de pouvoir améliorer la dosimétrie du cristallin des opérateurs utilisant les installations de radioscopie par l'introduction de facteurs d'étalonnage représentatifs des situations pratiques.

Mots clefs : spectre en énergie, rayonnement diffusé, radiologie interventionnelle, détecteur à pixels hybrides, Timepix3, dose.

Résumé vulgarisé

La découverte en 1896 des rayonnements ionisants a permis, notamment grâce à l'utilisation des rayons X, d'imager les structures anatomiques du corps humain. Cette avancée technologique permet au radiologue ou au cardiologue non seulement d'obtenir des images pour poser un diagnostic mais aussi de le guider pour effectuer des procédures chirurgicales minimalement-invasives évitant ainsi le recours à la chirurgie ouverte.

Cependant, cette technique avantageuse conduit inéluctablement le patient et le personnel médical à une exposition aux rayonnements ionisants. Lors de chaque examen, le tube à rayons X émet un faisceau primaire, constitué de photons, qui en interagissant avec les structures anatomiques du patient crée une image radiologique. L'interaction des rayons X qui traversent le patient génère, en chemin, un champ de radiations secondaires de rayons X (le rayonnement diffusé) qui est émis dans toutes les directions. Ce rayonnement produit par le patient s'étend dans la salle d'examen et peut ainsi exposer le personnel médical à des doses relativement élevées, surtout lorsque celui participe de manière répétée à des opérations relativement complexes. Pour être en mesure de quantifier de manière précise la quantité de rayonnement auquel le personnel est exposé, il est nécessaire de pouvoir évaluer la distribution des rayons X en fonction de leur énergie : leurs « spectres » d'énergie.

Si ces spectres d'énergie sont bien connus pour les installations standards de radiologie ce n'est pas le cas pour les installations modernes qui exploitent les propriétés des rayons X pour réduire au minimum l'exposition du patient. La détermination des spectres d'énergie s'avère toujours difficile et ce même avec l'arsenal dosimétrique disponible actuellement. Les instruments de mesures utilisés jusqu'alors nécessitent l'utilisation de forts systèmes de refroidissement, et des mesures dans des conditions très restrictives (grandes distances, collimation du faisceau), ne permettant pas ainsi de connaitre précisément l'énergie et le nombre de photons émis. L'objectif de ce travail visait à caractériser de manière extensive un nouveau type de détecteur, développé au CERN, afin d'investiguer son potentiel d'utilisation pour améliorer la dosimétrie du personnel médical.

En effet, la grande majorité du personnel médical reçoit des doses très largement en-dessous des limites légales. Dans ce contexte leur dosimétrie n'exige pas d'efforts particuliers pour connaître précisément la dose reçue. Néanmoins, pour une petite fraction des radiologues ou cardiologues, il est nécessaire d'estimer leur exposition de manière plus précise puisqu'ils risquent d'atteindre des niveaux d'exposition proches des limites légales qui assurent leur protection radiologique.

Le travail effectué dans le cadre de cette thèse comporte deux volets : d'une part l'étude et l'optimisation des conditions d'utilisation d'un détecteur spectral pour la caractérisation de spectres produits à proximité du patient en radiologie ou cardiologie interventionnelles, et d'autre part l'utilisation de ce détecteur en situation clinique pour évaluer la variabilité du contenu spectral en salle de radiologie interventionnelle. Ce travail devrait servir de base au développement d'un dosimètre adapté à une utilisation en routine clinique.

List of Acronyms

APD	Active Personal Dosimeter
ASIC	Application Specific Integrated Circuit
CdTe	Cadmium Telluride
CERN	European Organization for Nuclear Research
CHUV	Lausanne University hospital
CONCERT	European Concerted Programme on Radiation Protection Research
CZT	Cadmium Zinc Telluride
EURADOS	European Radiation Dosimetry Group
FOPH	Federal Office of Public Health
GaAs	Gallium Arsenide
HPD	Hybrid pixel detector
HPGe	High Purity Germanium
HUG	Geneva University Hospitals
IC	Interventional Cardiology
ICRP	International Commission on Radiological Protection
ICRU	International Commission on Radiation Units and measurements
IR	Interventional Radiology
IRA	Institute of Radiation Physics
LHC	Large Hadron Collider
MC	Monte Carlo
Odosim	Ordinance on individual dosimetry
ORaP	Ordinance on Radiation Protection
PODIUM	Personal Online Dosimetry Using computational Methods
TLD	Thermoluminescent Dosimeter
TOA	Time of arrival
TOT	Time over threshold
UNSCEAR	United Nations Scientific Committee on the Effects of Atomic Radiation

List of figures

Figure *27* - Dose comparison between DoseAware (pink), TLD (green), DMC3000 (yellow) and Timepix3 (blue) detectors. For different tube current intensities at 100 kV.

1 Introduction

1.1 Clinical context

Image-guided procedures with X-ray offer a strong alternative compared to invasive surgical procedures, with a lower risk of infection and faster recovery times, *i.e.* shorter hospitalisation times. Most of these procedures are often outpatient. The number of interventional radiology (IR) procedures has thus been constantly on the rise over the recent years. Image-guided procedures are used for both diagnostic and therapeutic purposes and cover a wide range of specialties such as IR, angiology, interventional cardiology (IC), interventional neuroradiology and urology.

The benefits of image-guided procedures for patients are accompanied, however, to exposure to ionizing radiations. In 2010, a report from the United Nations Scientific Committee on the Effects of Atomic Radiation (UNSCEAR) showed that medical imaging procedures using ionizing radiation is the greatest radiation exposure to humans through artificial sources [1].

During image-guided procedures the medical staff in the IR suite is exposed to the scattered radiation field generated within the patient. Many procedures require that part of the staff remains close to both the patient, and the X-ray tube. The development of more complex and longer procedures combined with the higher number of patients inevitably leads to an increase in exposure of hospital staff members. This is confirmed by a national survey presenting the exposure of the Swiss population to ionizing radiation in medical imaging [2]. One of the graphics indicates, for example, the dose from medical examinations in IR increased by 14% in Switzerland between 2008 and 2013. A 2020 report showed that in 50% of audited hospitals, interventions involving high doses were regularly, even very often, performed [3].

A Federal Office of Public Health (FOPH) mandate to estimate the doses received by radiologists and cardiologists was conducted by the Institute of Radiation Physics (IRA) of Lausanne University hospital (CHUV) in 2006 and resulted in a snapshot of the staff exposure in large hospitals. This study showed in particular that among the radiologist population, 58% received an annual dose lower than 20 mSv measured with the dosimeter worn above their protective apron. The average dose (above the apron) was 2.1 mSv/month whereas the maximum dose reached 10.8 mSv/month. These results are consistent with those published by Sanchez *et al.*[4] who conducted a similar study and showed that more than 50% of the monitored radiologists exceeded a dose of 20 mSv over the protective apron in a year. Concerning the cohort of cardiologists, only 15% of them received an annual dose lower than 20 mSv measured with the dosimeter worn above their protective apron. The average dose

(above the apron) was 0.8 mSv/month, whereas the maximum dose reached 7 mSv/month. It is clear that even if some of these values are high, they seldom exceed the annual limit on personal effective dose limit. Considering the dose measured above the protective apron was representative of the exposure of the unprotected area of the body, and of the equivalent dose for the eye lens. These results showed that the former annual equivalent dose limit of 150 mSv was not exceeded and that no special measures had to be taken at the time.

Epidemiological studies support the fact that there is a significant increase in the rate of diagnosed cases of partial or total opacity of the eye lens in the setting of chronic radiation exposure [5–8]. The International Commission on Radiological Protection (ICRP) lowered the annual equivalent dose limit for the eye lens (from 150 to 20 mSv) in 2011 [9], resulting in changes to the legal limits in Europe and Switzerland. This was of particular relevance in IR where it is well established that staff doses can be significant.

With the entry into force on January 1st, 2018 of the new radiation protection ordinance [10], and the ordinance on personal dosimetry [11], people in the immediate vicinity of a source of ionizing radiation during IR procedures must wear a second dosimeter above the protective apron. In order to guide the services in implementing this ordinance, a pilot study was carried out in 2019 at the CHUV and Geneva University Hospital (HUG). Results indicate that 25% and 14.3% of the values measured above the apron exceed 20 mSv per year for spinal and vascular surgeons in the operating room at CHUV, respectively. Similar findings were observed in 12.5% of radiologists and 15.8% of cardiologists at the HUG. These values, however, are extrapolated and do not integrate the possible use of individual radiation protection gear like leaded glasses or visors, which may reduce eye lens exposure.
This study lead to the identification of two categories of staff in operating rooms. The first population, representing the majority of the workers, have dosimetry records well below the limits and even below the reporting thresholds per monitoring period. A second population, often working closer to the patient and the X-ray tube or performing complex procedures, represent a small percentage of the staff and have dosimetry records close to or exceeding the limits. Risk management for the latter population must therefore be more precise and more suitable to correctly monitor the eye lens exposure. When worker dose records approach or exceed the annual limits, knowledge of the radiation fields to which they are exposed is necessary in order to accurately determine their exposure. Characterising the radiation fields allows not only to optimise the protection of the patient, but also to adapt the protective gear of the staff.

1.2 State of the art of X-ray beam spectral characterisation

The use of X-rays has led the scientific community to characterise the radiation beams both at the exit of the tube (primary beam) and near the patient (secondary or scattered beam). Knowledge of the spectral characteristics of the primary beam where it enters the patient makes it possible to better control skin exposure while maintaining an adequate clinical image quality level. At the same time, a better characterisation of the spectral component of the scattered radiation should enable the use of more optimised radiation protection gear and a better risk management with improved staff dose assessments.

The first spectral measurements of primary radiation were reported at the beginning of the 20th century [12,13], and were based on measurements of attenuation curves. Forty years later, the first Monte-Carlo (MC) simulations were proposed [14–16], accompanied by the first measurements using spectrometric detectors based on NaI or Germanium (Ge) crystals [17–19]. Today, similar measurements have been performed by many groups with High Purity Germanium (HPGe) or Silicium (Si) [18,20,21], NaI [22], Cadmium Telluride (CdTe) [23,24] or photodiode [25] detectors. The characterisation of the primary beam is nowadays of limited use as the X-ray tubes that are used in clinical devices provide standard beam qualities with inherent filtrations ranging from 0.50 to 2.55 mm Al equivalent. Figure 1 presents the energy spectra for the primary beam of a standard diagnostic X-ray tube of 80 kVp. Moreover, the HPGe, Si, and NaI detectors necessitate the use of a highly collimated beam and large distances from the source to manage their limitations in terms of instantaneous fluences. These detectors require significant cooling systems based on the use of liquid nitrogen. In terms of detectors operated at room temperature, semiconductor technology may suffer from pile up effects due to data acquisition saturation effects that then result in spectral distortions. It is interesting to note that Terini *et al.* [25] presented measurements based on the use of a photodiode to provide spectra at room temperature despite a limited detection efficiency. For all detector types doing measurements of the primary beam, complex corrections are needed such as detector efficiency, Compton scattering effect, escape effect…

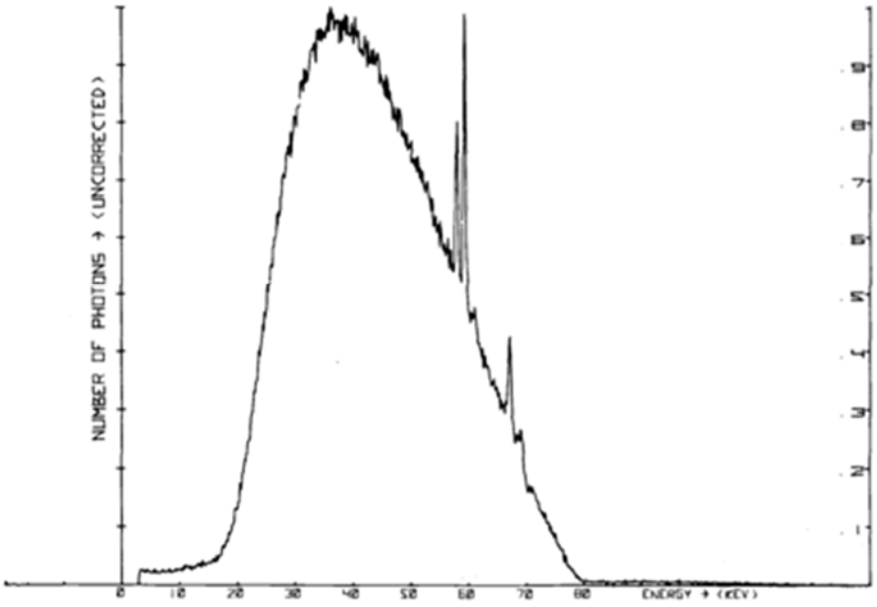

Figure 1 - Energy spectra of the primary beam for a typical 80 kVp diagnostic X-ray [21].

1.3 Example of spectral characterisation

As mentioned in the previous section, energy spectra measured with standard beam qualities used in the field of radiology are available in the literature. The article by T. Fewell *et al*. [21] compared spectra at the entrance and exit of the patient (Figure 2), as well as in the scattered radiation, which is of particular interest for the evaluation of the staff exposure.

These measurements were performed with an HPGe which enables the acquisition of good quality X-ray spectra but requires restrictive conditions of use. In order to avoid excessive spectral distortion, the team set up a small beam opening as well as a large distance from the source. The spectra were established by measuring only the Compton scattering photons. For this, the primary beam must be strongly collimated and interact with a material dense enough to create the Compton effect. The spectra obtained are then corrected for the photoelectric effect. As expected, the interaction within the body of the patient modifies the shape of the energy spectrum. Indeed, the average energy moves from 44 keV in the primary beam to 49 keV for the scattered field at 20° upwards from the patient, and to 58 keV at the exit of the patient (in contact with the body) (field that is collected by the detector and is used for imaging). The personnel are exposed to a lower fluence than that at tube exit, but to a higher photon energy.

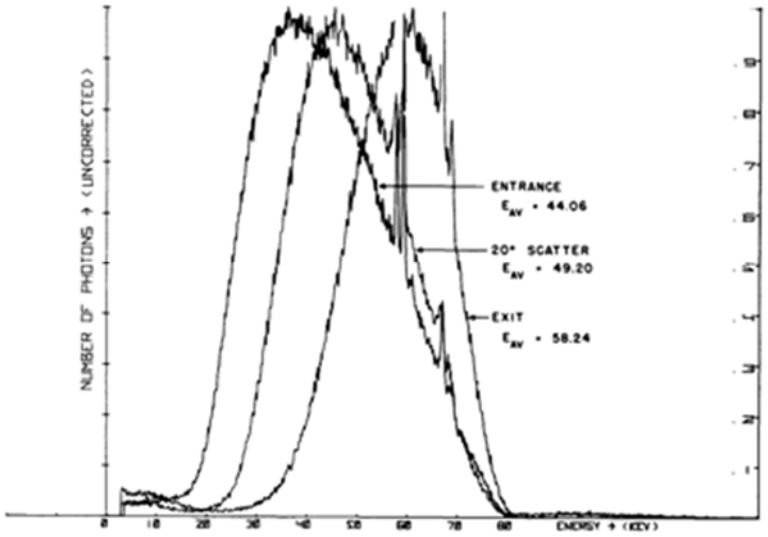

Figure 2 - Energy spectra, from left to right, of incident, exit, and scattered X-ray spectra [21].

Available data on the characterisation of the primary beams is sparse, and a survey of the literature indicates even fewer publications on direct measurements for the scattered radiation field. The first measurements of the scattered radiation field were made in 1923 by A. Compton [26] in order to prove its existence. The theory proposed by A. Compton was that scattered radiation exists since each quantum of X-ray interaction in a material is scattered by an individual electron [27]. Scattered radiations were obtained by recording the interactions of the primary radiation with a crystal. These measurements, carried out with an ionisation chamber, required a strong collimation of the beams and allowed spectra to be obtained without indication of fluence, as relative measurements.

Subsequently, several studies have presented an assessment of the energy spectra of scattered radiation around an X-ray tube using MC simulations [14–16]. This method is widely used to model ionising radiation interactions in matter, the calculations of the scattered spectrum does require a heavy computational power and often long calculation times to get enough statistics. In addition, the filtering inherent in the tube is no longer a known parameter, making MC simulations very delicate. However, the results of Zagorska *et al.* [28] make it possible to compare spectra measured in primary radiation and spectrum estimated for scattered radiation, for an inherent filtration of 3 and 4.5 mm of aluminium. McCaffrey *et al*. [29] investigated the alteration of the spectrum of the scattered radiation through the protective gear worn by medical staff. The study showed that the photon number is attenuated by 95% with 0.5 mm Pb equivalent but with an alteration of the spectrum. It also presents a comparison of the spectra of the primary and scattered radiation with results that are in good agreement with those presented by Zagorska *et al*.

Experimental verification of spectra simulated by MC code is a burdensome task, and few articles provide details on the measurement constraints and challenges to be faced. In 1957 Cormack *et al.* [30] measured the spectra in the scattered radiation beam using a scintillation spectrometer. The experimental setup required collimation of the detector directly connected to the cylinder water phantom in order to measure the radiation scattered at very precise angles. A very fine opening and a tin collimator were necessary. The fluence was reduced to the minimum in order not to saturate the detector. Marshall *et al*. [31] measured energy spectra using an HPGe detector for different positions of the tube; results are presented in Figure 3. In addition to a lead collimation of the beam, and a large distance to the source, the detector required cooling with liquid nitrogen. Photons can only enter the detector through a pinhole, in order to ensure the reduction of the fluence to match the detector response and avoid spectrum distortion due to saturation. Collimation allows only scattered measurements at very precise solid angles, so an overall measurement of scattered radiation requires a very large number of measurements for a given position. Bhat *et al.* [32] explained that the HPGe detectors must be limited to 1500 counts/s in order to avoid pile up. Those measurements provide information that help validate the shape of the spectra obtained through MC simulations but cannot provide information on the fluence.

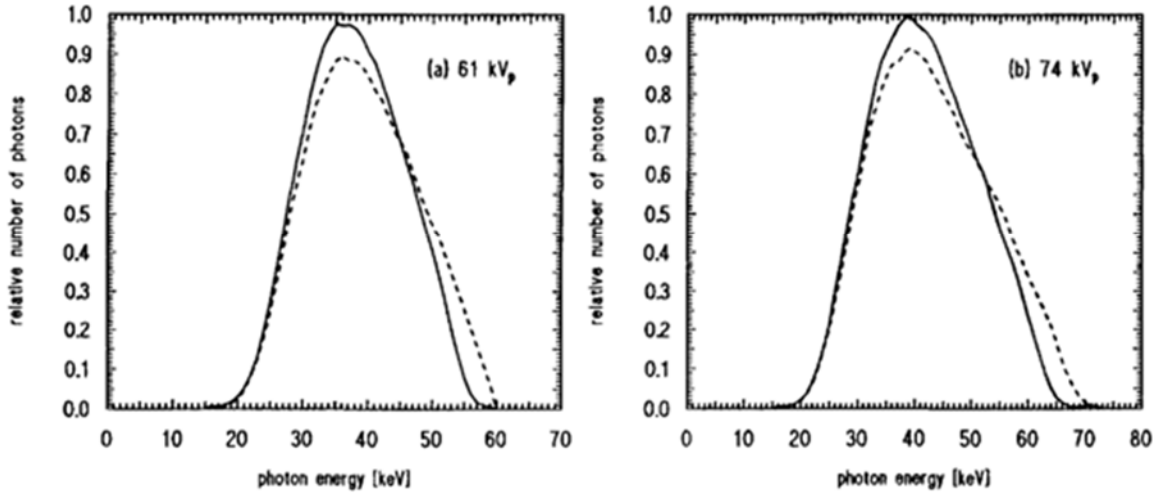

Figure 3 - Scattered X-ray spectra measured by Marshall *et al.* [31] with the X-ray tube under couch, for two different geometries. – and --- represent, respectively, the spectra where the detector made an angle of 90° and 135 ° with the primary beam.

1.4 Risk management tool

The risk management is driven by the knowledge of the effects of ionising radiation on the human body and the environment. A keen understanding of the interaction mechanisms is essential for assessing the risks associated with exposure to ionising radiation.

Research programs in radiobiology and epidemiology surveys have contributed to the development of models for evaluating the radiation-induced risks and establishing protective measures. The aim of the models is to decrease the probability of stochastic effects to levels deemed acceptable. The models that are used to define such limits have been developed on available data sets. The main cohort is composed of the Hiroshima and Nagasaki population [33,34]. Additional data comes from the epidemiology studies of astronauts exposed to cosmic radiation, of workers and the population affected by the Chernobyl accident, or the radium girls who were exposed via radioactive substance intake when painting the dials and hands for the watch industry [35–37]. The limits are constantly re-evaluated to adapt protection in accordance with any knowledge of possible health effects. A better understanding of the effects of ionising radiation on the organism and organs led the ICRP to revise the dose limits both for the general public and for workers on several occasions [38]. These limits have been regularly lowered both for the effective dose and for organs that were previously thought to be less sensitive to radiation, as was the case recently for the eye lens [39].

The occurrence of opacities in the eye lens have been investigated in several domains [5–8,40–42]. Based on these results, the ICRP decided to lower the dose limit for the eye lens in 2011, making it equal to the annual dose limit for the whole body [39]. The new limit value raised many practical questions along with new challenges for dosimetry. Indeed, before this change, dosimetry management of eye lens exposure was not directly measured. As the former limit of 150 mSv was well above the limit of 20 mSv for the whole body exposure, there was a general consensus that respecting the effective dose limit using a routine personal dosimeter worn on the chest would implicitly result in respecting the dose limit to the eye lens.
For the few workers who came close or exceeded the 20mSv value measured with their personal dosimeter worn at chest level over the apron, this change led to several questions: Is it possible to use current personal dosimeters that are calibrated to measure deep and shallow dose equivalent and extrapolate those values to estimate eye lens exposure? Is it necessary to create a new operational quantity to monitor eye lens exposure? In the specific case of the medical staff working in an IR suite and exposed to a heterogeneous radiation field [43], is it possible to estimate the eye lens dose with a single dosimeter worn on the chest? Working groups have been created in Switzerland and across Europe to investigate these questions and propose strategies. Furthermore, the impact of the use individual protection gear such as protective glasses should be taken into account for the appropriate estimation of the eye lens dose and an additional dedicated correction factor for goggles needs to be defined.

Risk management and identifying who are at risk of exceeding the annual limits require an accurate dose measurement. The dosimetry management should evolve along with the new recommendations and tools for dose assessment should be adapted to face these new challenges.

The next section presents an analysis of the different type of detectors currently used by dosimetry services.

1.4.1 Dosimeters

Two types of dosimeter technologies with complementary characteristics are commonly used to monitor worker exposure: passive and active dosimeters. Passive dosimeters measure the radiation dose integrated over a time interval. The dose is then determined by an approved personal dosimetry service, i.e. the dose cannot be read directly from the dosimeter itself. In many countries, the dose value from the passive dosimeter is considered the official or legal dose that is counted for the period during which it was worn. Active dosimeters allow real-time measurements with a direct display of the dose (or both the dose and dose rate) value. In Switzerland, all requirements for establishing a dosimetry management program and performing individual monitoring for external exposure are defined in the ordinances and guidelines published by the authorities [44].

1.4.1.1 Passive Dosimeters

Among the different types of passive dosimeters that are used by the seven dosimetry services in Switzerland [45], most of the systems are based on Thermoluminescent Dosimeters (TLDs) representing the majority of the 97'000 workers whose exposure is monitored professionally [46]. The operating principle is based on the fact that electronic excited states are created in crystalline materials when exposed to ionising radiation. The electrons that are trapped in the crystal lattice, are releasing their energy in the form of photons (light) when the material is heated at a given temperature and heating ramp. The amount of photoluminescence is directly proportional to the amount of radiation, that can be accounted as the dose. The principle is illustrated on Figure 4.

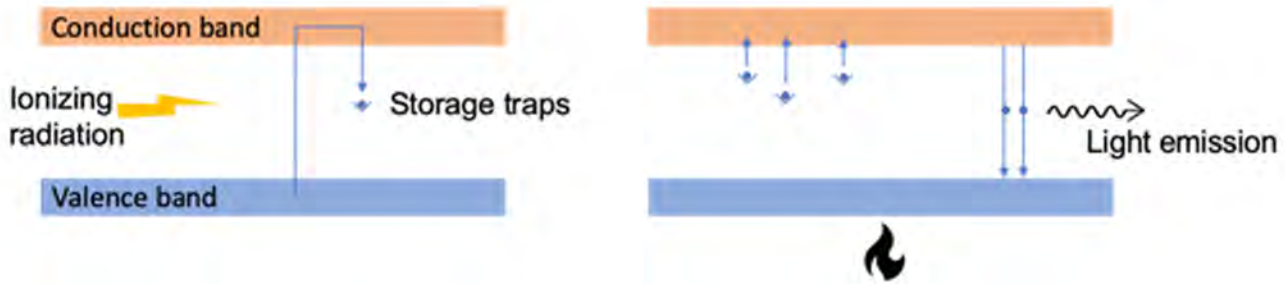

Figure 4 - Diagram of the working principle of TLD dosimetry.

The material that is often used is Lithium fluoride doped with magnesium and titanium (LiF:Mg,Ti) as it offers a good compromise for dosimetry, especially being tissue equivalent

and easy to produce in a large scale at a low cost. The use of different types of Lithium ions (Li6 and Li7) provides an additional interesting feature for dosimetry as it enables determining the dose from neutron exposure.

The crystals are produced in small chips that can be placed under filters of different thicknesses in order to obtain a rough spectral evaluation (depending on the number of chips and filters). A specific algorithm is developed for each type of dosimeter design to process the collected data from each chip and to calculate the operational dosimetry quantities $H_p(10)$ (deep dose) and $H_p(0.07)$ (skin dose).

During the heating phase, the information store in the TLD chip is erased, and it can be used again. The chip is considered as annealed after the first reading in personal dosimetry applications. There is no possibility of a second reading.

TLDs measure photon energies from 20 to 10^4 keV. Although their energy response curve is energy dependent up to 200 keV, an over response rate of 20% is recorded at 80 keV [47]. For this reason, their calibration is carried out at higher energies (often with Co-60 or Cs-137), where the response curve of the detector is stable. Recent work shows that the angle with which the photons reach the dosimeters is important and its action cannot be neglected. Most radiology rooms are equipped with an X-ray tube located under the table. The incidence angle of the incoming photons would then be greater than 75 ° for different positions of the workers in the room. In some cases, the photons would then not enter the badge dosimeters through the windows provided for this purpose but through the lower part and the measured dose could be wrong. Radio photo luminescent dosimeter can also be found, they are based on a silver doped glass dosimeter, with non-destructive reading.

Table 1 – Advantages and disadvantages of passive dosimeters

Advantages	Disadvantages
Easy to obtain dose	Dose erased after reading (TLD)
Tissue equivalent	Energy corrections
Reusable	Angular correction
Cost effective	No real-time reading
	Handling

1.4.1.2 Active dosimeters

Active Personal Dosimeters (APD) (sometimes called operational dosimeters or EPD which stands for Electronic Personal Dosimeters) provide a direct display of the cumulative dose and/or dose rate and in most cases can be programmed with alarms. These features offer

significant advantages compared to passive dosimetry. The user is aware of his exposure and cumulative dose in real time. These devices can help local radiation protection experts better analyse these parameters and optimize the work procedures in order to minimise the dose. In the case of IR, they allow staff to adapt their work in real time, for example by readjusting the radiation protection gear that may have moved during the procedure. Some of these dosimeters, such as Dose Aware (Philips, Amsterdam, Netherlands), are used for pedagogical purposes to train the staff and improve radiation protection awareness. The Dose Aware toolkit is composed of a base station and small Bluetooth connected badges. The staff can visualise the colour coded (green, orange, red) real time information about the wearer's exposure on a control screen visible by the whole team. Workers using this technology will immediately see the effects on the dose rate and cumulative dose by using a protective screen or by positioning themselves differently in the room. The information provided by the system may not be used as a legal dose recording.

Whole body active dosimeters are commonly worn on the chest and give a dose or dose rate information in terms of $H_p(10)$ and $H_p(0.07)$. They often integrate vibrating alarms, with audible and visual signals. Active dosimeters can also be worn on the fingers to monitor extremity doses in real time in order to minimise the dose to this part of the body, which is the most exposed for an interventional radiologist. A novel example is the ED3 extremity dosimeter (John Caunt Scientific Ltd, Lancashire, England) for eye lens dosimetry that is currently only monitored passively with TLD’s.

These dosimeters are often based on diode semiconductor technology (see Part 1.6) and unlike TLDs, this technology is not tissue equivalent and is more expensive. Because of its screen and alarms, this type of dosimeter is a larger device compared to a passive dosimeter. Depending on the model, data saved in the internal dosimeter’s memory makes it possible to analyse the wearer's exposure time by time. Unlike TLDs, data are not deleted each time the dosimeter is read.

These dosimeters are sensitive to a wide range of energy, from 15 keV to 7 MeV for example for the DMC 3000, with a dose increment of 1 uSv [48]. They can therefore be used for a large number of applications. However, some restrictions should be taken into account as the literature has highlighted the rapid saturation and inaccuracy of some of these detectors when used in pulsed fields [49]. Hupe's article supports this point by studying the influence of pulsed radiation fields on measurements made with various active dosimeters; most of them present an insufficient dead time correction [50]. Additionally, like for passive dosimeters, corrective factors as well as angular corrections must be applied if they are used in conditions which differ from the way and energies at which they have been calibrated.

Table 2 - Advantages and disadvantages of active dosimeters

Advantages	Disadvantages
Dose display in real time	Energy corrections
Can be programmed with Alarms (sound or vibrating)	Angular correction
Dose range from uSv to tens of Sv	Expensive
Models with dose rate information	Pulsed field dependant
Models with dose history over time	

1.4.2 Operational quantities

The concept of risk management is based on the principles of radiation protection: Justification of practice, Optimization of protection and safety, and Limitation of the dose. The annual limits concerning the exposure of the public or workers with occupational exposure is given in terms of effective dose for the (whole) body and personal equivalent dose for specific parts of the body (extremities, skin, and eye lens) (Annex1). The effective dose was first introduced by the ICRP to set limits for radiation protection purposes. It is a derived quantity or mathematical construct and not a physical, measurable quantity. The formula for calculating effective dose to a reference model incorporates terms to account for all radiation type [51,52]. Operational quantities for individual dosimetry were introduced to relate the primary quantities (*i.e.* effective dose and equivalent dose) to the quantities measured in practice with conventional radiation protection instrumentation. They represent the equivalent dose in a tissue at a given depth. The dose equivalent is determined for three depths: at 0.07 mm deep for skin, 3 mm deep for the eye lens, and at 10 mm deep for internal organs and considered to be representative for the whole-body dose.

The doses measured with active or passive dosimeters are counted in terms of operational quantities $H_p(d)$ which must then be linked to primary dosimetry quantities. As defined in section 1.11.2 of the Swiss Ordinance on Radiation Protection (ORaP) "The personal dose equivalent $H_p(10)$ is used as an estimate of the effective dose. The personal dose equivalent $H_p(0.07)$ is used as an estimate of the dose to the skin and to the lens of the eye. Alternatively, the personal dose equivalent $H_p(3)$ may be used as an estimate of the dose to the lens of the eye." [10]

This simplified approach is valid when the recorded values remain below the legal dose limits. When limits are exceeded, further investigations must be carried out. This is specified in Section 2.4 of the ORaP "If the dose values determined […] are above the relevant limits, then the effective dose or equivalent doses for the person concerned must be individually determined by a radiation protection expert, in cooperation with the supervisory authority, using calculation methods and dose coefficients in accordance with the current state of science and technology.

The value thus determined is decisive in establishing whether or not a dose limit has been exceeded". [10]

The current operational quantities defined on the International Commission on Radiation Units and measurements (ICRU) 4-element soft tissue sphere offer a pragmatic and reasonable approach to estimate the values of the operational quantities. However, they overestimate the effective dose for external exposure to photons below 100 keV, by up to a factor of 5, as illustrated in Figure 5 [53-56].

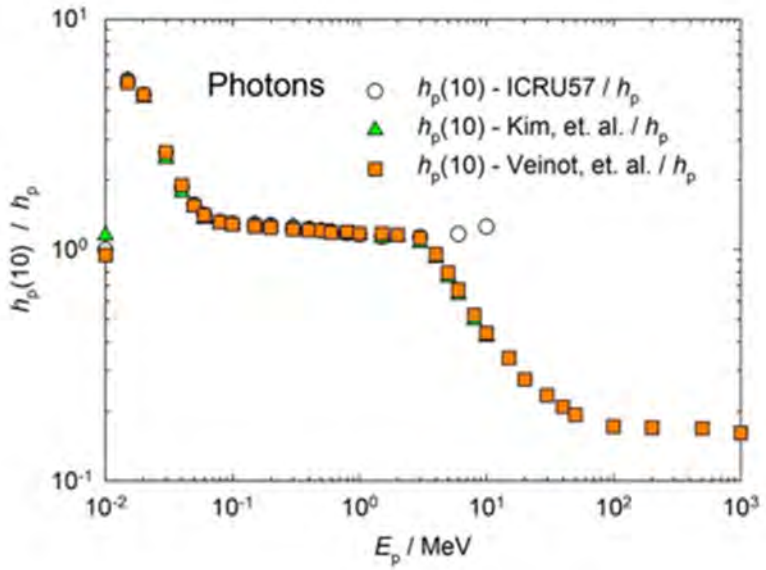

Figure 5 - Comparison of conversion coefficient $h_p(10)$ for photons [53–56].

A joint report from the ICRU and the ICRP on operational quantities for external radiation exposure was released in 2017 [53]. This report suggests new operational quantities that would provide a better estimate of the actual dose delivered to the body and therefore an enhanced tool to manage the risk of stochastic effects. The proposed quantities are derived directly from the characteristics of the radiation field using conversion factors, between the radiation fluence and the effective dose. These factors have been calculated with Monte Carlo (MC) simulations and mathematical phantoms. The proposed new operational quantities will have an impact on staff exposure as there is a strong impact on the low energy photon range which is of interest for medical applications (< 100 keV) [57]. The new effective dose value could be up to a factor four lower that the present $H_p(10)$ value. This new approach, which is still currently under discussion, will affect routine radiation measurement practices in the medical field, and will undoubtedly trigger the development of a new generation of instruments.

1.5 Dosimetry surveillance

Dosimetry surveillance programs are regulated at the national level. Each country has its own legal structure and laws in this area. The radiation exposure must be determined individually over a given period for individuals with occupational exposure and this is the responsibility of any contractor with professionally exposed employees. In the Swiss system, the ordinance on personal dosimetry [11] specifies that the dosimeter should be worn at the chest level (or at the abdomen level during pregnancy).
If the dose measured by the routine dosimeter is not representative of the effective dose of the operator, *i.e.* in case of an inhomogeneous radiation field, the supervisory authority may request the worker wear additional dosimeters. Similarly, hospital staff, who are working in the immediate proximity of X-ray generators in IR theatres and wearing a protective apron, are required to wear a second dosimeter. In Switzerland, the concept of so-called double dosimetry was introduced in 2001 [58].
Currently, the equivalent dose to the eye lens is considered equivalent to the skin dose measured by the dosimeter worn on the chest above the protective apron even though we know that this equivalence has limitations [43]. Another possibility is to measure the dose directly with a dosimeter carried as close as possible to the eye lens. A correction factor will be taken into account if the workers are wearing protective glasses.

In terms of recommendations for the position of the dosimeter, or even for the type of dosimeter to be used, the legislation is not harmonized between European countries [59]. Each country has different practices. In Switzerland, the FOPH recommends wearing the personal dosimeter on the chest, and imposes a double dosimetry for staff close to the patient, while France requires staff to wear an additional active dosimeter in controlled areas (art R 4451 - 111 of the working code [60]), and Germany requires staff to wear a single dosimeter under the apron. As for eye lens dosimetry, Spain, Belgium and a majority of European countries recommend wearing a thyroid dosimeter while double dosimetry is used in Switzerland [61].

A survey conducted by the European Radiation Dosimetry Group network (EURADOS) [49] highlights a large disparity of practices in terms of where active dosimeters are worn by hospital medical staff. The majority of hospital workers (53%) wear it above the apron at the chest level, 11% wear it at the neck level, 11% on the waist, and 16% wear it under the apron.

Depending on the country, the doses measured with APD are counted in national dosimetry registries or not. In France, this is declared together with passive doses in their national registry called SISERI [62]. Whereas in Switzerland, actives doses are considered only as an indication for the worker and used for optimisation, the dose records are not transferred into the National Swiss dosimetry database. Moreover, there is no European consensus on the algorithm to be

used to calculate the effective dose when using a double dosimetry system. At CERN, the active dosimeter is mandatory to access to controlled area.
These differences in guidelines for dosimetry surveillance were further accentuated with the appearance of new limits for the eye lens. There is currently no strict guidance on how to address the challenges of efficiently measuring the dose to the eye lens. In Switzerland, the equivalent dose to the eye lens is assumed to be the equivalent of the individual surface dose $H_p(0.07)$ measured by the whole-body dosimeter worn at the chest level (combined values of the under and above dosimeter in case of double dosimetry). In the case of inhomogeneous radiation fields when the dosimeter on the chest is not representative of the eye lens dose, the supervisory authority may require staff to wear a dedicated dosimeter at the eye level on a case-by-case basis. For France, a dedicated eye lens $H_p(3)$ dosimeter had to be worn for each worker of category A [63].

The evolution of dosimetric monitoring requires medical personnel to wear several dosimeters. This is a daily challenge and a constraint for the staff. To avoid having medical staff wear multiple dosimeters and address the uncertainties which arise from different dosimeter positions, the PODIUM (Personal Online Dosimetry Using computational Methods) project was launched within the framework of CONCERT: the European Joint Programme for the Integration of Radiation Protection Research. The project investigates new ways to assess the radiation exposure of medical staff using MC calculation based on motion detection and staff tracking in the IR theatres.

Currently available commercial active dosimeters like the DMC3000 provide a dose and a dose rate but the value displayed does not take into account the spectral information of the incoming radiation. Those instruments will have to be resigned to comply with the recommendations of the ICRU and ICRP and provide a dose calculated from the fluence and photon energy. Current active and passive dosimetry are missing important information as they measure a dose which does not integrate the energy spectrum. The need for a dosimeter able to measure both fluence and energy is becoming more and more crucial now that the shortcomings of our current dosimetry have been highlighted.

1.6 Hybrid pixel detector

To address the problems related to current dosimetry practices, this thesis focuses on a new type of dosimeter based on the technology of a hybrid pixel detector (HPD). This type of detector can record the following data for different particles: time of detection, spatial distribution, energy information. Developed in 1980 at the CERN, it was used for particle tracking in high energy physics experiments at the Large Hadron Collider (LHC) [64–66]. An HPD is composed of two separate layers: the sensor and the electronic readout system. Each of

these layers are produced and can be optimized separately. Each single pixel of the semiconductor layer is connected to its own readout chip, the Application Specific Integrated Circuit (ASIC), developed at CERN [67], and are assembled with a bump-bonding process. When this project began, this stage of the Timepix chips was very delicate. This was not a mass produced, commercially available system. Any error in this process and defect on the wafer would automatically lead to a noisy or dead pixel that would have to be discarded from the matrix.

The sensor layer can be made of different materials such as silicon (Si), Ge, gallium arsenic (GaAs), Cadmium Zinc Telluride (CZT), CdTe, or diamond, depending on the application field of interest.

Semiconductors require only a small amount of energy to create an electron hole pair (in Si 3.6 eV) which means that even a small energy photon can be detected [68]. The diagram of a semiconductor is presented in Figure 6. When a particle crosses the sensor and deposits energy, an electron-hole pair is created. The number of electron-hole pairs is dependent on the particle and its energy, but also on the ionization energy specific to the sensor material. The current applied through the sensor, called the bias current, allows the movement of electrons from a lower potential to a higher one and creates an electric field. The signal obtained is proportional to the number of electron-hole pairs and thus to the energy and the type of incident particles.

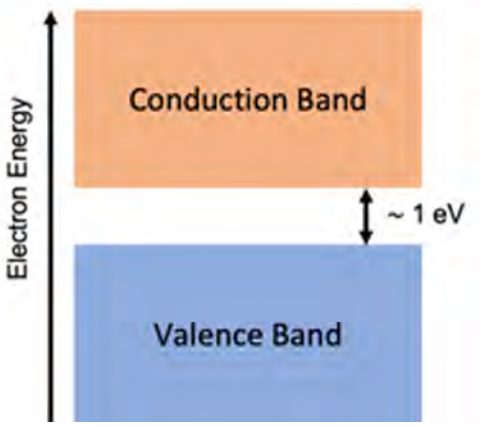

Figure 6 - Theoretical scheme of a semiconductor. Valence and conduction band are represented.

Each pixel of the diode structure bump bonds to a corresponding pixel on the readout chip [69]. Figure 7 represents a view of the architecture of a HPD, and a photo of bump-bonds.

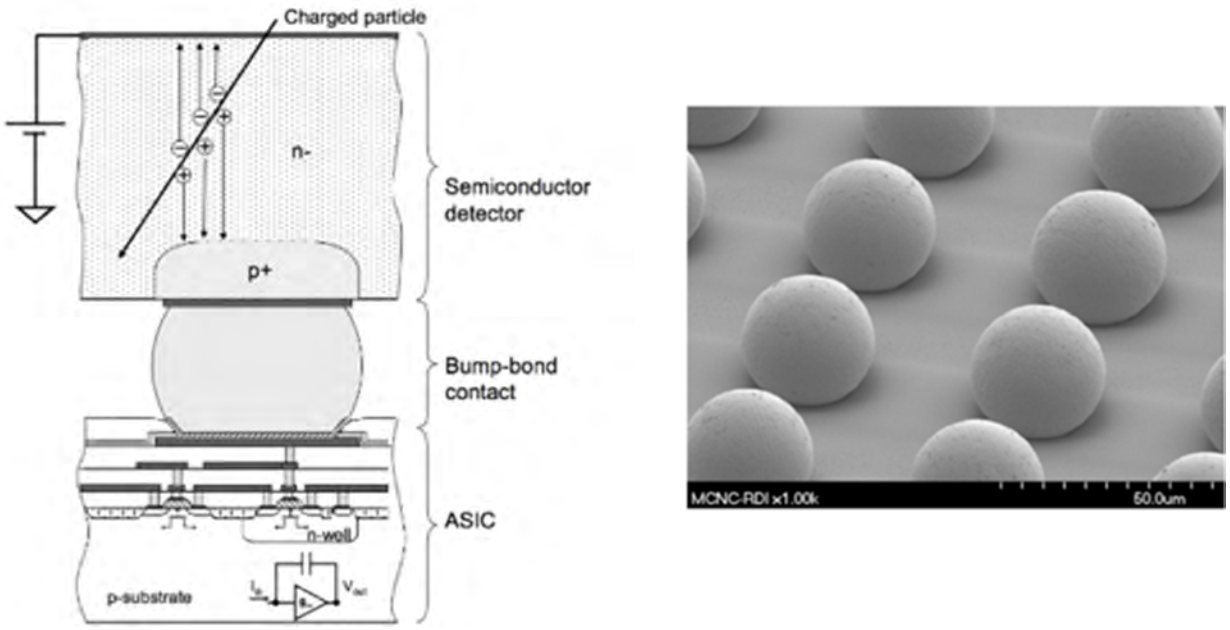

Figure 7 - Schematic view [70] of an HPD on the left, semi-conductor sensor connected to the readout electronic (ASIC) by bump bonds. A picture of the bump-bonds is presented on the right.

When a particle crosses several neighboring pixels, a signal is generated in one and each of them, creating a cluster of pixels. The charge sharing among the pixel boundaries must be corrected (see Section 2.4.2). In order to record only the interactions due to radiation, the threshold chosen must be high enough compared to background noise. This will be explained in Section 2.1.

1.6.1 Timepix3

The Medipix collaboration was created in 1997 to explore the possibility of photon counting X-ray imaging. Since then, four international collaborations have emerged, resulting in the development of specific ASIC designs and detectors for a growing number of applications in high energy physics, medical imaging, space dosimetry, material analysis, and education [71–74]. This work focused on the use of the most recent chip developed at the time by the Medipix framework at CERN [64], the Timepix3 chip with an embed general-purpose ASIC that can be operated in several acquisition modes depending on the application.

This chip is composed of a pixel matrix of 256 x 256 square pixels of 55 µm side; a large number of small pixels enable a better tracking precision as well as high flux capabilities. This HPD can be used both in Time of arrival (TOA) or Time-over-Threshold (TOT) mode. In TOA mode, the arrival time of each particle is measured compared to the closing of the shutter. The TOT mode makes it possible to estimate the energy deposition by measuring the time during which the signal is above a given threshold. This mode will be further developed in Part 2.1. Timepix3 is a driven readout, which means that rather than reading the entire image once the

acquisition is completed, a data set that includes pixel coordinates, TOT and TOA is created for each hit, and is sent directly out of the chip. This reduces the reading time and therefore the dead times, meaning the chip remains active for a long period of measurement. The pixel dead time due to pulse processing and packet transfer is 475 ns, with the signal collected in 10 ns [68], leading to a maximum count rate of 85.3 Mhits/s/chip, with a minimum time resolution of 1.56 ns.

Timepix3 works with the Pixet Software (Advacam, Prague, Czech Republic) which makes it possible to modify the intrinsic parameters of the detector (threshold, Ikrum, etc) but also to hide noisy pixels. The software has a real-time display of the measured spectra, and extracts the data according to the chosen mode (TOT, TOA ...). As indicated in Part 1.6., HPD can be equipped with different materials for the sensor. Timepix3 sensors are most often in Si, or CdTe.

Figure 8 - Picture of the Timepix3 detector.

1.6.2 Advantages and disadvantages

The technology of HPDs are convenient for providing information on photon energy spectrum and fluence. This tool is interesting for dosimetry and yet unmatched by any other detectors.

This technology offers a strong benefit compared to the current passive and active systems. An additional interesting feature resides in the fact that the detection limits of HPDs can be very low, down to 0.5 keV [75], compared to current dosimeters with an energy range starting, for the best instruments, at 15 keV [48].

Compared to other spectral detectors [17–24], the Timepix3 has the advantage of not requiring beam collimation with heavy pinhole shielding. It can be used at any distance from the radiation source in the scattered field and the spectra are obtained from the first seconds of measurement.

Besides these obvious advantages, the cost of the detector used in this study is quite significant and it remains fragile. The Timepix3 is still undergoing R&D and the current model needs to be cooled using a small portable fan. Its size, associated with the cooling system, and a high voltage power supply currently prevent its routine use in a clinical environment. Collaboration with the Medipix team, however, allows us to work on the detector in order to miniaturize it.

Table 3 - Advantages and disadvantages of Timepix3 HPD

Advantages	Disadvantages
Fluence and energy spectra information	No water equivalent
Real time reading	Cost
Large dose range measurements	Fragile
No calibration on phantoms	Cooling system
	Power supply

1.6.3 From spectra to dose

Dosimetry with spectral information obtained with the Timepix3 will take on its full extent with the appearance of the new ICRU / ICRP factors based on fluence.
The measured fluence and energy spectrum are used to calculate the associated dose. The measured spectrum is segmented into energy bins of 0.5 keV, then corrected for absorption efficiency and for the pixel sharing effect (see part 2.4). Each corrected energy bin is multiplied by the factors available in the literature [53].

1.7 Goal of the PhD thesis

The results of the first article completed in the context of this work confirm that some of the medical staff members are strongly exposed when performing image-guided medical procedures. The experiment itself facilitated a better understanding of the challenges of radiation protection in situations where other vital risk management has to be considered.
The second article included in this manuscript highlights the limits of current dosimetry and led us to adapt a HPD developed by CERN for high-energy radiation fields (TeV to MeV) into a spectral dosimeter for the medical community using fluoroscopy units where radiation energy ranges from 30 to 120 keV.
The Timepix3 chip with a Si sensor layer was the best suitable available device at the start of this work. After adapting this chip to the requirements previously mentioned (work in operating room with fluoroscopy units) together with the team in charge of the development, the chip had to be fully characterised. It was first calibrated with radioactive sources and fluorescence of various metallic foils covering the energy range of interest for medical applications. Measurements were carried out to compare the spectra obtained with those from the literature or simulated by MC code. The proper functioning of the detector made it possible to validate the proof of concept. The second part of the work focused on calculating correction factors inherent to the detector or due to the variation of environmental parameters. Thus, the absorption efficiency as well as the correction for pixel sharing were estimated. The effect of changes in temperature, angle and detector illumination were also assessed.

The final part of this work focuses on the measurements carried out in a hospital environment that enabled us to characterise the radiation field (fluence and energy spectra) at various positions where hospital staff members stand around a patient during routine fluoroscopy guided procedures guided. We created a fluence mapping in an IR room. In addition, we were able to link the energy spectra measured with the detector to a dose.

This thesis lays the foundations for further developments of a novel dosimeter that would provide a better characterisation of the radiation fields to which the medical team is exposed in interventional radiology and cardiology. The outcome of this work could provide a way to respond to dosimetric monitoring in line with the proposed new dosimetry operational quantities. The results paved the road towards an active dosimeter using the HPD technology.

2 Materials and method

As mentioned in the introduction section, the detectors of the Medipix family are designed and developed from a wide range of applications. From LHC measurements to the space station as well as medical imaging [64–66,72,74].
The relevant parameterisation and calibration of the detector is the responsibility of the user. Discussions with the Medipix team at CERN resulted in the selection of the Timepix3 detector as the best option for single-photon spectroscopy with relevant energy resolution for the medical field (0-100 keV). One of the goals of this work was to assess the performance of that detector in scattered radiation beams where radiation directionality is absent in comparison to its use as an image detector. The Timepix3 ASIC was mounted on a 300 µm thick Si layer and was operated in a TOT mode.

The next sections detail those features, as well as the choice of the sensor material, and its calibration, or the correction factors used for measurements.

2.1 TOT mode

The spectroscopic features of the Timepix3 detector rely on measuring the time the signal remains above a given threshold. The higher the dose, the longer the TOT. Indeed, the amplitude and the time width of the pulse produced by the interaction of X-rays with the Si layer are proportional to the energy of the incoming photon. For each incident photon, a cascade of electron-hole pairs (see Part 1.6) is created in the sensor layer. The applied electric field on the sensor allows a fast drift of the cascade and a fast collection of the signal with low spatial spread. During detector equalization, which occurs to avoid threshold dispersion, and affects both the noise and the energy resolution of the full chip, a threshold is determined. The threshold is set to eliminate background noise and takes only the photons originating from radiation events into account.

In the TOT mode, the energy deposited is estimated by measuring the time during which the signal is above a selected threshold. The counter of each pixel is incremented by one each time the pulse exceeds the defined threshold and the amplitude of the signal is proportional to the energy of the incident particle (Figure 9).

The TOT feature depends on the radiation fluence, as the probability of several incoming photons on a single pixel increases, the pile-up probability increases as well. This phenomenon can lead to an overestimation of the TOT. The signal of two particles can be summed if they arrive in a too short lapse of time on the same pixel and the signal of the first particle had not

yet decreased enough to fall below the set threshold (Figure 9). Timepix3 saturation is over 40 Mhits/s/cm^2. The optimal response of the detector in a primary radiation beam, such as the one encountered in the primary beam of radiological units, is then no longer guaranteed and will require special data processing and corrections.

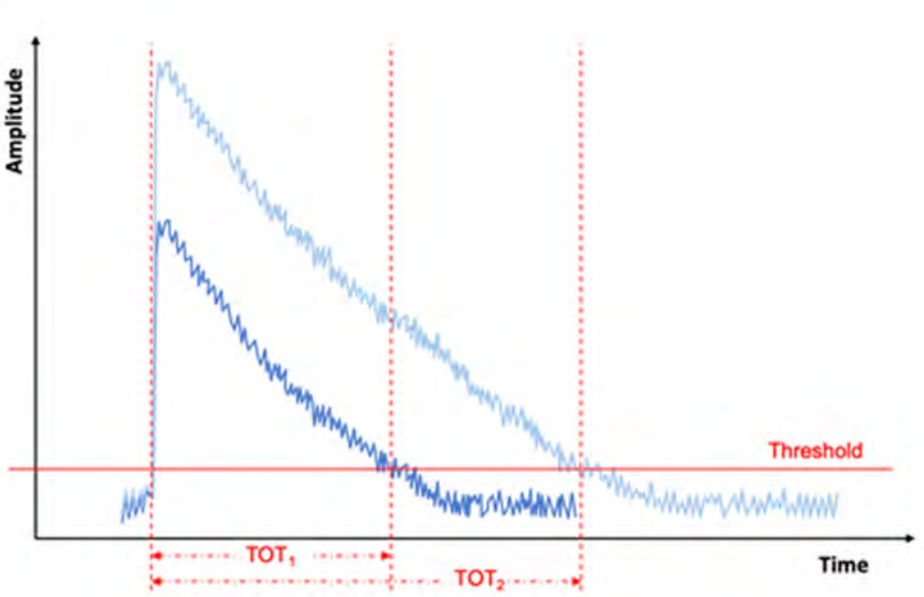

Figure 9 - Blue lines represent two signals with different amplitudes and their related TOT.

2.2 Sensor material

The selection of material for the sensor is a compromise between several factors, such as the cross section, mechanical properties, availability, and price. This part will explain our choice for a Si sensor.

The scattered energy in clinical conditions ranges from 20 to 100 keV. As seen Annex 2, Figure 29, for an energy of 50 keV, the photoelectric effect will be 10 times greater than the Compton effect. However, around 100 keV, these two effects will start to compete with each other, with a slight predominance of the photoelectric effect. This behaviour is illustrated Annex 2, Figure 35 for Si material. The importance of the predominant effect will enable an understanding of the interactions within the detector to adapt the correction factors when necessary.

The predominance of the photoelectric effect compared to the Compton effect allows us to know that if the particle interacts with the detector, its energy will be deposited at the position of interaction. Even if an electron is created in the medium, this electron deposits its energy locally, unlike the Compton effect where part of the energy can escape the detector medium under the form of a scattered photon. This phenomenon leads to an underestimation of the particle energy. This scattered photon can also remain within the detector medium but can also interact in another pixel. The resulting information will be that the interaction of two photons

of different energies have interacted with the sensors. This can be observed in the spectrum and is called “Compton edge”.

One of the factors impacting the response of the detector is the probability of particle interaction within the sensor. Figure 10 shows the absorption efficiency curves as a function of the photon energy for different interacting thicknesses and materials. This graphic shows that the absorption efficiency for Si drops drastically compared to Ge, GaAs or CdTe. Moreover, the probability of fluorescence reactions depends on the chosen materials. Those fluorescence photons can interact at other pixel positions than that of the incident photon. Spatial but also energy information of the incident photon are then modified. Despite its low energy absorption, the response of the Si detectors is quite stable since only 4% of the photons will lead to fluorescence processes compared to 50% for GdAs or 80 to 87% for CdTe. In addition, the average free path of a fluorescence photon is 10 µm with Si compared to 110 µm with CdTe, leading to large spatial errors.

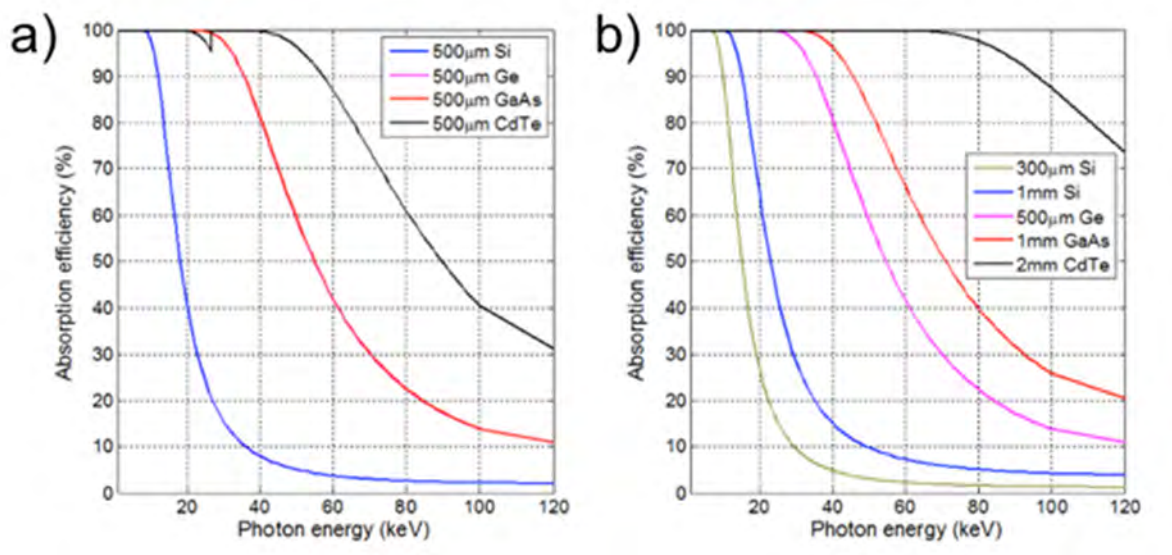

Figure 10 - Absorption efficiency of different materials (Si, GaAs and CdTe) for different thickness [76].

The graphics below (Figure 11) present a MC simulation using Geant4 of an ideal detector, for Si or CdTe sensor of 500 µm thickness. The simulation was carried out for 10^6 photons of 40 keV. On Figure 11 the Compton edge can be easily identified for the Si, and not on the CdTe, where the visible peaks at low energy correspond to the fluorescence peaks of Cadmium and Tellurium. In these ideal detectors, the energy resolutions are respectively 0.28 keV and 0.31 keV for Si and CdTe. In an actual detector this small difference would be masked by other factors like the electronic noise of the detector or the charge sharing. However, a difference in amplitude of the peaks can be noticed. This difference is due to the absorption efficiency of the materials.

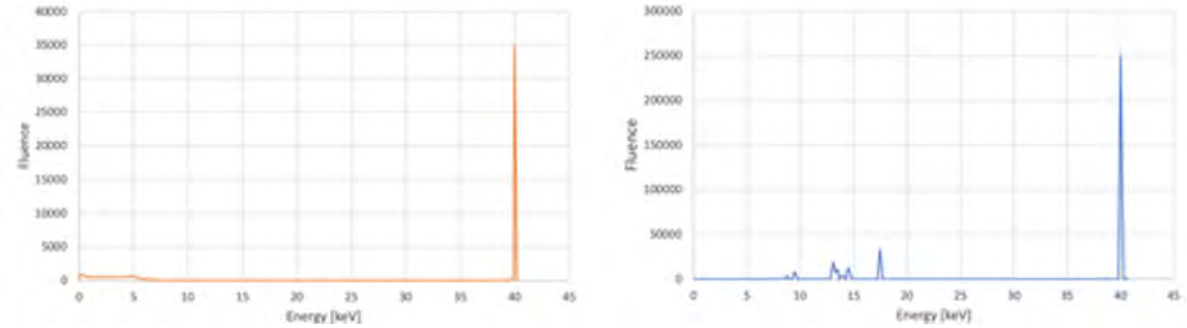

a) Si b) CdTe

Figure 11 - Energy spectrum simulations with Geant4 for an ideal detector with Si (left) or CdTe (right) sensor.

Finally, Si was also chosen for the sensor because of its stability, in terms of production chain and over time, which confers a high reproducibility of the measurements. Si sensors avoid repetitive calibration and do require a detector restart before each data acquisition. In addition, silicon is advantageous because it's less expensive than cadmium or diamond. The Timepix3 detector used in this work was made with a 500 μm layer of Si sensor. As developed in the next section, the calibration of the detector includes the use of correction factors for absorption efficiency and pixel sharing (see part 2.4).

2.3 Calibration

For this specific work, the calibration of the detector was done for beam energies ranging from 20 to 100 keV to match the scattered radiation characteristics found in hospital theatres where fluoroscopy units are used.

At the time of our study, the Timepix3 chip was not commercially available. This means that each chip may differ from one to another. Thus, before calibration, the proper functioning of the chip had to be checked. Some chips might have been damaged due to previous uses or have been improperly assembled. Some chips might also suffer from bonding defects, resulting in noisy pixels that must be masked. However, if this problem is recurrent on the chip, the detector becomes unusable. In such a case, even after a new calibration, the uncertainty on the measurements remains significant. A chip can also present a break that is invisible to the naked eye and induce an error on the measured spectrum. Manipulation error can lead to deteriorate the chip in an a priori nonvisible way. Unfortunately, it sometimes happens that a defective chip is not discovered until after the calibration measurements are completed. The calibration process is thus time-consuming and the repetition of the calibration measurements, as well as data analysis from three detectors was necessary before finding a functional one. However, unless there is a major incident, once the calibration has been carried out, the detector usually

remains stable. Fortunately, this can easily be checked thanks to the use of a known energy radiation source.

The calibration process makes it possible to determine the response function of the TOT with energy and thus convert the TOT values into energy. As each pixel has its own associated electronics and behaves as a single detector, calibration must be performed individually for each of the 65,536 detector pixels. Calibration is carried out with reference radioactive sources or by measuring the fluorescence peaks of different materials. The energy spectrum that is measured for the eight references listed in Table 4 by each single pixel was fitted with a Gaussian function. Automatic data processing was made using Python codes. The median value of the Gaussian distributions corresponds to the TOT of each material for a given pixel. Each of these TOT values is then linked to the gamma energy lines of the radioactive source and to the fluorescence energies of the reference materials.

Table 4 – Sources and metallic foils used for calibration and their corresponding energy:

	Element	Energy [keV]
Sources	Fe-55	5.89
	Am-241	59.54
Metallic foil	Cu	8.05
	Ti	4.51
	Mo	17.45
	Sn	25.20
	Zr	15.75
	Ar	22.16

Figure 12 shows the energy spectrum measured with an Americium source with a given single pixel (at position 100,100 on the detector matrix). This spectrum provides the number of detected photons as a function of TOT. The analysis of the Gaussian function gives a TOT value of 51.6 A.U (arbitrary unit). This value will be related to the energy of Am-241 emission that is at 59.5 keV. Figure 13 shows the calibration curve for the same pixel; the eight values of TOT measured and related to energy. The curve responds to Equation 1. For each of the 65,536 pixels, the values a, b, c and d are extracted. Figure 14 represents Am-241 energy spectrum once the calibration is performed, without sharing pixels or detection efficiency corrections.

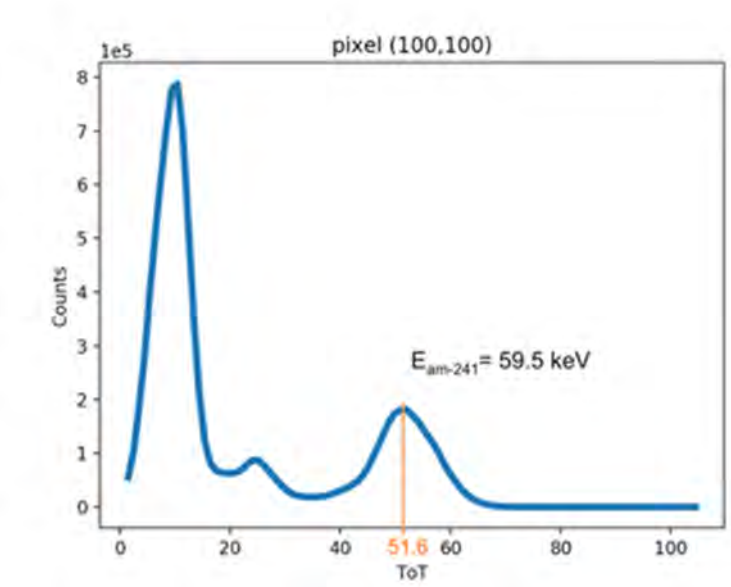

Figure 12 - TOT spectrum for photon emissions of Americium-241 decay for pixel 100, 100. The TOT value of 51.6 AU corresponds to 59.5 keV.

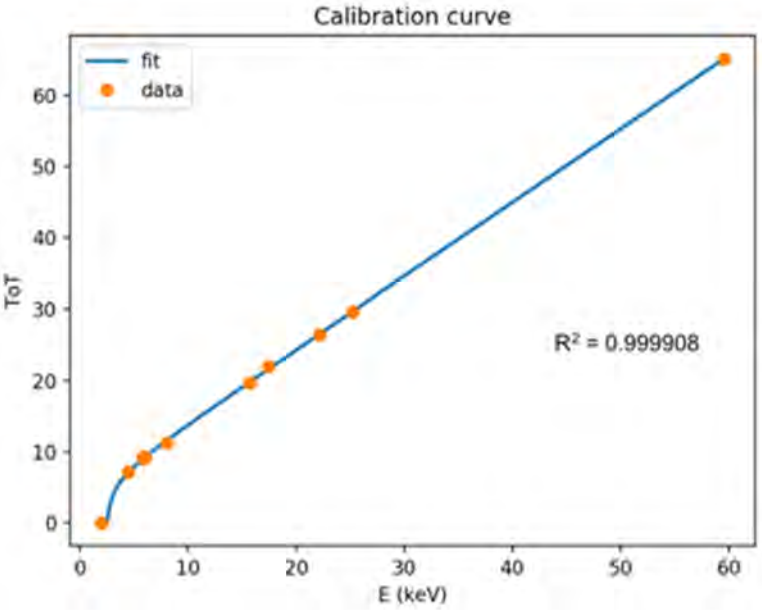

Figure 13 - Calibration curve.

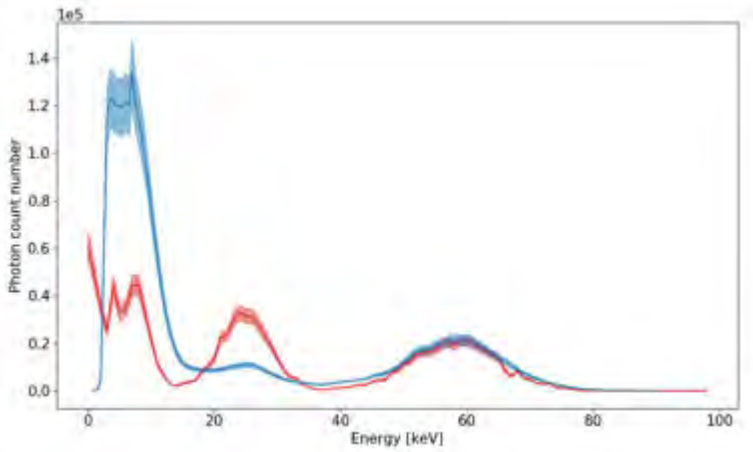

Figure 14 - In blue, energy spectrum measured for the photon of the Americium 241 decay. In red, simulated spectrum of the Americium source. Light blue or light red curves represent the uncertainty.

$$f(x) = ax + b - \frac{c}{d - x}$$

Equation 1 - Calibration function.

2.4 Data corrections

Data acquisition by the Timepix3 equipped with a Si sensor requires corrections for pixel sharing and absorption efficiency.

2.4.1 Correction for pixel sharing

When a photon hits the detector, it can, in the simplest case, interact with one pixel and deposit its energy there, or arrive at the border between several pixels (Figure 15). It is then necessary to determine on which pixel the photon arrived and to recalculate its energy, which was divided between several pixels. For this, it is necessary to take into account a very precise spatial and temporal window, in order not to confuse the different events occurring on the sensor.

During calibration, only single pixel events were taken into account. In order to avoid measurement errors and to remain in the same conditions as during calibration, all the data collected during this work were in single pixel mode. A correction factor was calculated to compensate for missing data. The “Pixet” software integrates algorithms capable of representing TOT spectra, for photon hitting 2, 3, 4, ... pixels. This correction factor was calculated directly by analysing these spectra and the single pixel spectra. The correction factors are shown in Figure 16.

2.4.2 Correction for absorption efficiency.

As seen in Annex 2 on Figure 35, the silicon absorption efficiency curve decreases rapidly with the energy increase. Correction factors specific to the geometry of the Timepix3 have been calculated by MC code for photons with energies ranging from 0 to 90 keV and are shown in Figure 16.

A corrected and calibrated spectrum is presented Figure 17.

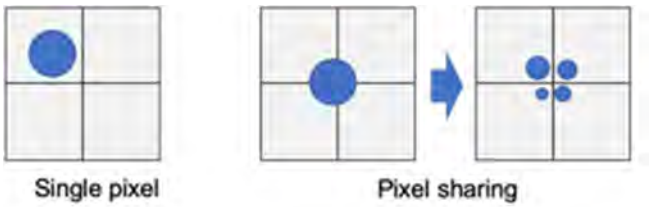

Figure 15 - On the left, a photon hit one pixel. On the right a photon hit four pixels, this led to a pixel sharing.

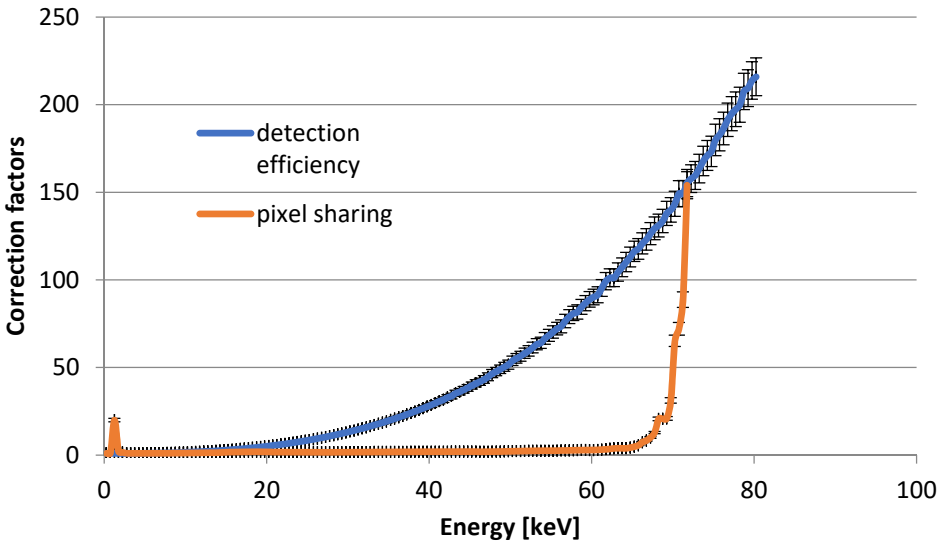

Figure 16 - Correction factors for detection efficiency in blue, and pixel sharing in red.

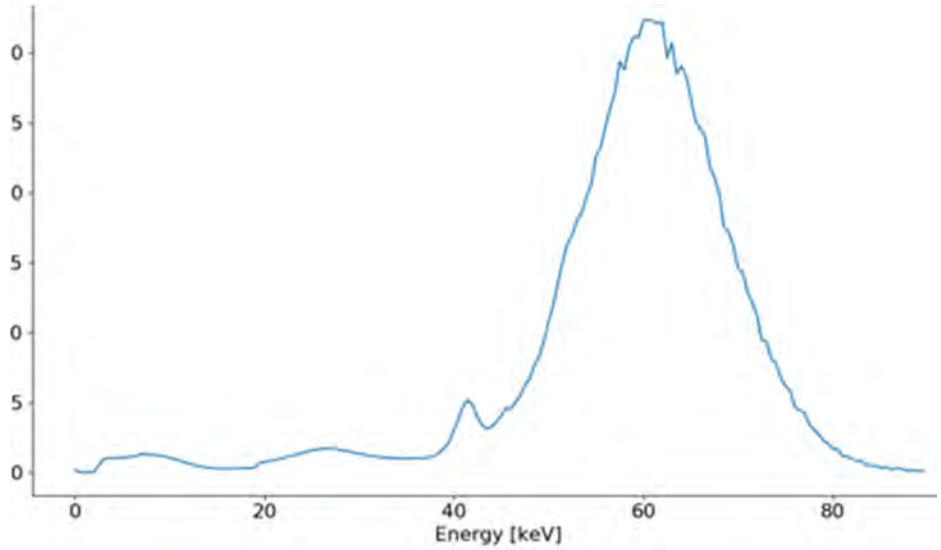

Figure 17 - Americium spectrum calibrated and corrected for pixel sharing and detection efficiency.

3 Results

3.1 Scientific publication 1: Eye lens monitoring programme for medical staff involved in fluoroscopy guided interventional procedures in Switzerland

Paper I - Published in Physica Medica (January 2019)

The purpose of this study was to verify the monitoring method for eye lens dosimetry established by the Swiss authorities. In 2011, the annual dose limit for the eye lens was lowered from 150 mSv to 20 mSv. In order to control this new limit, Swiss authorities proposed to take the dose using the operational dosimetric quantity $H_p(0.07)$ measured at the chest level above the lead apron as the value of the equivalent dose to the eye lens.

In order to verify this method, measurements were taken using an anthropomorphic phantom under controlled conditions as well as measurements with volunteer surgeons from several departments of CHUV, equipped with their routine dosimeters and with an additional specific eye lens dosimeter.

The aim of the measurements under controlled conditions was to calculate several geometric factors under specific position configurations, for given specialties. To this end, routine dosimetry badges as well as individual TLD pellets were placed on an anthropomorphic phantom representing the practitioner. A solid water slabs phantom was used to mimic an adult patient who, when exposed to X-ray, generates a field of scattered radiation in the room. The position of the tube and protective gear as well as the position of the practitioner were chosen to be representative of the IR, surgery, and urology rooms.

The aim of the measurements in clinical conditions was to compare the values of the dose received by the eye lens in terms of $H_p(3)$ and the dose received on the chest in term of $H_p(0.07)$. The study of the ratio of these two quantities made it possible to check whether the compliance with $H_p(0.07)$ occupational exposure limits on the chest would systematically imply compliance with the eye lens dose limit.

Results under controlled conditions showed an exposure gradient from the left to the right side of the head at the front head level depending on the clinical specialty. The maximum dose was identified on the left temple for diagnostic and IR and above the left eye for surgery and urology. Measurements under controlled conditions showed that most of the doses measured on the dosimeters worn at the chest level were higher than those measured at the eye lens level. This is however not the case for urology, due to the specific X-ray tube position, which is, for obvious reasons, above the patient's couch. The measured eye lens dose may, in some cases,

exceed the measured $H_p(0.07)$ value at the chest level where the official badge dosimeter has to be worn.

Measurements under controlled conditions showed that the body is exposed in an inhomogeneous manner, and that the measurements between the different dosimeters give very heterogeneous geometric factors. Measurements under clinical conditions showed that, except in special cases, compliance with the dose limit in $H_p(0.07)$ on the chest represents compliance with the dose limit for the eye lens. However, if the dose is exceeded on the badge, there is no way to estimate the dose received by the eye lens. Establishing an accurate correction factor for a given person is highly complex and depends on many uncontrolled parameters. Thus, a particular effort has to be done to lower as much as possible the eye lens dose using specific protections.

The article highlights that the eye lens dosimetry is a great challenge. This article investigates the limits of the current practice of staff dosimetry. Moreover, it gave us improved knowledge about the scattered radiation field produced in operating theatres, thus providing ways to improve exposure monitoring.

3.2 Unpublished results: First energy spectra measurements with a Timepix3 chip for clinical x-ray beam qualities.

After calibrating the detector, and in order to ensure the proper functioning of the chip in conditions to be met in a clinical environment, measurements were carried out under controlled conditions with a Toshiba KXO-80G X-ray generator in the irradiation facility at the Institute of Radiation Physics (CHUV), Lausanne.

3.2.1 Materials and methods

The scattered radiation field was generated by a water phantom placed on the irradiation bench, 5 m away from the X-ray tube. Several set-up conditions were used to provide reference beams of interest for medical applications conforming to the International Electrotechnical Commission standard from 60 to 120 kVp, and 10 to 160 mA, during 6000 ms. A first series of measurements was performed with the Timepix3 chip placed on the water phantom, facing the primary beam to test the detector response and pile-up effect influence in high flux conditions. A second series of measurements was performed with the Timepix3 chip placed next to the bench, 30 cm away from the water phantom at a 90° to the primary beam to test the response of the detector in the scattered radiation field.

3.2.2 Results

Figures 18 and 19 represent the fluence as a function of the TOT at 60 and 120 kVp, and different tube currents, respectively in the primary and scattered radiation. At this stage of the study, the detector was not calibrated in energy. Figures 19 and 20 show the theoretical fluence calculated at the level of the front face of the detector (red bars on Figure 19) and the measured fluence with the Timepix3 chip (blue bar bars on Figure 20), respectively for the primary beam and scattered radiations.

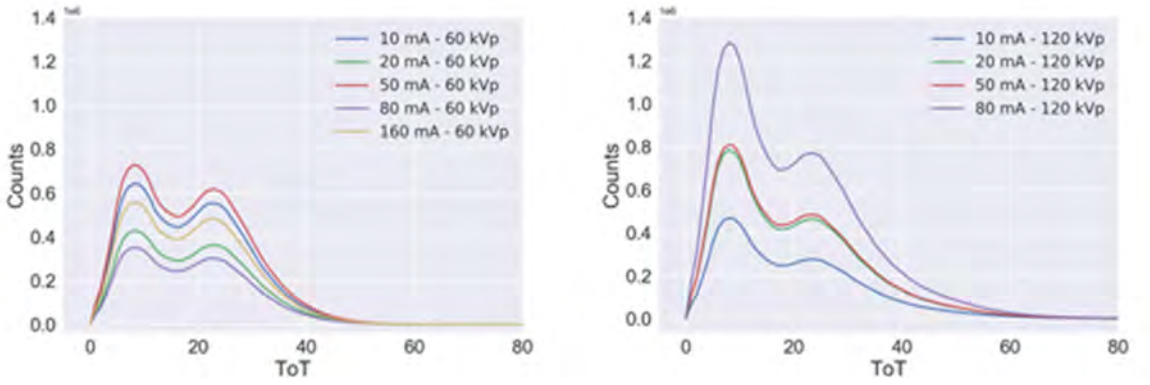

Figure 18 - Counts function of the TOT in the primary beam. Left graphic is for a peak voltage of 60 kVp and right graphic for 120 kVp.

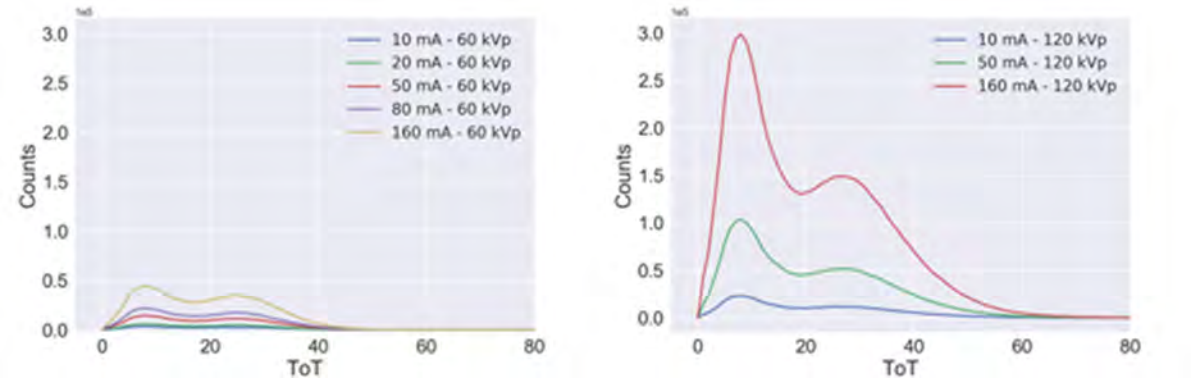

Figure 19 - Counts function of the TOT in the scattered radiation field. Left graphic is for a peak voltage of 60 kVp and right graphic for 120 kVp.

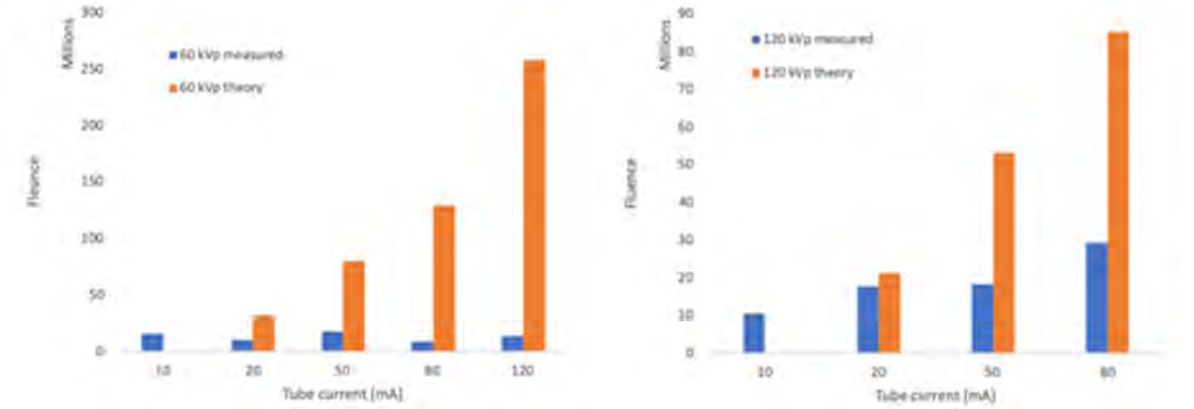

Figure 20 - Fluence of the primary beam measured (blue bar), and theoretical (red line), normalized for 10 mA. Left graphic is for 60 kVp and right for 120 kVp.

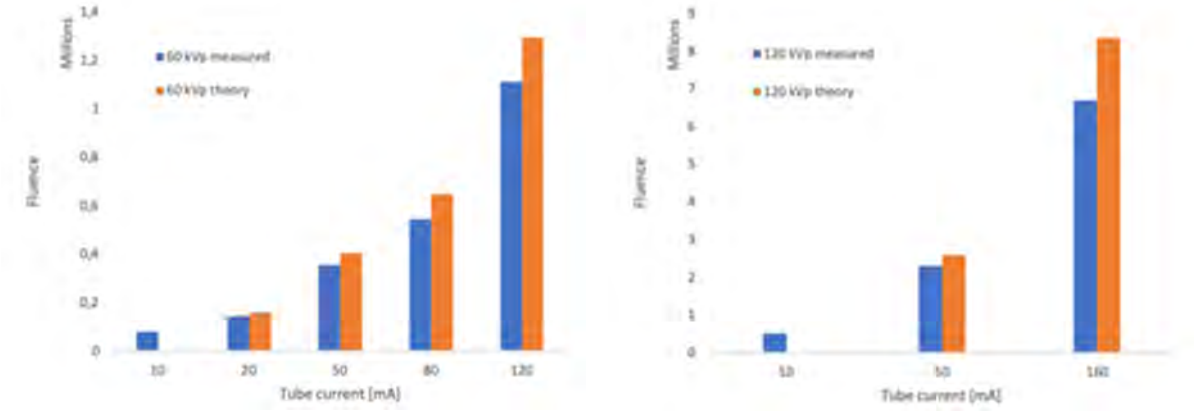

Figure 21 - Fluence of the scattered radiation measured (blue bar), and theoretical (red line), normalized for 10 mA. Left graphic is for 60 kVp and right for 120 kVp.

3.2.3 Discussion

The spectra of Figures 18 and 20 show a first peak at 8 keV which corresponds to the fluorescence peak of copper contained in the detector. The second peak corresponds to the average TOT of the beam. In the primary beam spectra are similar to those for the beam quality reference, RQR 5 [77].

It can be seen that the average TOT increases between the primary beam and the scattered radiation. This is explained by a beam hardening in the water phantom. The TOT maximum increases with kVp. Figures 19 and 21 reveal a lack of data in the primary radiation explainable by the saturation of the detector over 40 Mhits/cm^2/s. This problem does not appear in the scattered radiation field where fluence is 100 to 1000 times lower compared to the primary beam.

For this work, the detector was used in the scattered radiation field, thereby overcoming the problems encountered in primary beams

3.2.4 Conclusion

Detector saturation in the primary beam induces a loss of fluence although the spectra shape is preserved. Its use as a spectrometer would lead to an underestimation of the dose and a use as such is not recommended. Its use in the scattered radiation field should thus be preferred. This limitation does not apply when the detector is used as an image detector in an interventional radiology use where dose levels are quite low from the fact that most of the primary beam is absorbed within the patient. Using the detector for an X-ray tube voltage of 120 kVp with a continuous tube current 10 mA at 5 m of the source in the scattered beam shows a data loss of about 20%. To lower such a loss the detector was used with tube voltages around 80 kVp and a continuous tube current of 12 mA. Such conditions ensure a data loss lower than 5%. The first series of measurements did not show any pile-up effect, and the detector responded, as expected, proportionally to the tube current. These first measurements validated the proof of concept and confirmed the possible use of the detector to characterize scattered radiation fields in hospital theatres.

3.3 Scientific publication 2: Characterisation of the impacts of the environmental variables on Timepix3 Si sensor hybrid pixel detector performance

Paper II - Published in Nuclear Instruments and Methods in Physics Research (November 2020)

Our aim was to characterise the response of the Timepix3 chip to various parameters of interest for measurements in hospital theatres. The calibration and full characterisation of the detector were carried out.

The calibration procedure was performed with reference radioactive sources and X-ray fluorescence lines emitted by exposing several metallic foils to radiation.

The angular response of the detector was investigated over the range of -60° to +90° for the horizontal and vertical axis using a source of Am-241 and Fe-55 sources. The temperature and humidity responses were also investigated in a test chamber to control condensation in the ASICS between 0° and 36°. Finally, the light response was investigated under different intensities of continuous as well as pulsed light.

Measurements showed an angular dependence. The fluence provided by the detector is affected in amplitude without noticeable modification of the shape of the spectrum. Angular dependence is greater at low energy. The variation of the temperature modifies the measurement of the fluence and causes a shift in energy on the spectrum. This energy shift implies a dependence of the detector on the calibration temperature. In fact, an overly large temperature variation will cause measurement errors on the spectrum. This error increases with energy.
On the other hand, the measurements have shown that for continuous light, the response of the detector is not dependent on the luminance. In addition, the fluence is increased by 10% if the light strobes. It is interesting to notice that the spectrum retains its shape but becomes noisier and has a peaky appearance.

This study allowed to characterise the detector response to different physical parameter variations and to determined corrective factors. Our results show that precautions must be taken with regard to temperature fluctuations, but angular or light intensity variations are easily corrected if light does not strobe.

3.4 Scientific publication 3: Characterisation and mapping of scattered radiation fields in interventional radiology theatres

Paper III - Published in Scientific Reports (October 2020)

This article presents the energy spectra measurements of the scattered radiation field for different positions of IR staff members within the theatre, as well as a photon fluence map across the theatre.

All measurements were performed using standard protocol set-up of the C-arm fluoroscopy unit and at representative positions of each staff member during regular procedures. An anthropomorphic phantom was used to mimic the patient who generates a scattered radiation. A first series of measurements was performed on a volunteer person with the collective radiation protection gear (such as mobile shielded panels and shielded table apron) used by the staff. A second series of measurements was performed without any specific radiation protection gear in 57 positions within the theatre with the detector set on a metal rod at four different heights corresponding to the eye lens, the chest, the belt, and the knee of a 1.7 m reference person.

As expected, due to their position around the couch, the radiologist is the most exposed person, while the least exposed is the person standing at the patient's feet. The radiologist is exposed to a noticeable inhomogeneous exposure. The eyes are the least exposed and well protected behind the ceiling-suspended lead glass screens. The rest of the staff experiences a more homogeneous exposure. As expected with an X-ray tube under the couch, the strongest radiation field is at the level of the knees.

The energy spectra at the four chosen heights are presented, showing a shift in mean energy from head to toe for the staff standing close to the patient. To summarize the results, we created a cartography of the photon fluence around the X-ray tube.

This article presents the fluence and energy spectra of the scattered radiation field at several heights related to the position of medical staff within an IR theatre. This research also indicated that the HPD would be an interesting pedagogical tool for training medical staff in real time, and to better protect them. The results highlighted the non-homogenised radiation field on the human body and therefore raised the question of the reliability of staff dosimetry when dosimeters are worn at chest level.

3.5 Unpublished results: Dose obtained from energy spectra

The aim of these measurements was to link the measured spectra to a dose, and to control these results with existing detectors. The idea was to see the behavior of the Timepix3 HPD as a dosimeter based on spectral information.

3.5.1 Materials and methods

A Toshiba KXO-80G (Toshiba, Tokyo, Japan) X-ray generator was used to expose a water phantom placed on the irradiation bench, 2 m away from the X-ray tube. Several set-up conditions were used to provide standardized reference beams (ISO 4037) of interest for medical applications from 40 to 140 kVp, and 50 to 500 mA, for 500 to 1000 ms in order to get about 0.5 mSv ($H_p(10)$) on each dosimeter.

Detectors were placed each in turn on anthropomorphic phantom, facing the water phantom with a distance of 37 cm, perpendicularly to the primary beam. TLD, LiF: Mg, Ti were used in the form of bands of four as well as a DMC3000 (Mirion, Montigny-le-Bretonneux, France) and a DoseAware (Philips, Amsterdam, Netherlands) dosemeters. A Timepix3 (Medipix, Geneva, Switzerland) HPD was also placed on the anthropomorphic phantom as well as a Falcon 5000 (Mirion, Montigny-le-Bretonneux, France) to get spectral measurements. In parallel, the raw spectra obtained with the Timepix3 detector were simulated by Geant4 MC simulation.

The data obtained with the Timepix3 were corrected for sharing pixels and detector efficiency. Finally, each 0.5 keV energy bin was multiplied by the corresponding correction factor for photon to dose founded in ICRU and ICRP draft [53]. Each bin was summed up, thus obtaining a dose.

3.5.2 Results

Figure 22 shows the simulation of the scattered radiation field around the water phantom. The spectrum at the exit of the X-ray tube was simulated by MC code for an energy of 50 kV (Figure 23). Figure 24 shows the spectra in the scattered radiation field as simulated by MC code on the Timepix3 detector, and measured by the Timepix3 detector at 100 kV, 500 mAs. Figure 25 represent the spectra measured by the Falcon 5000 and the Timepix3 in the scattered radiation field at 40 kV, 500 mAs. Figure 26 and Figure 27 represent a comparison of the doses obtained with the DoseAware, the TLD, the DMC3000 and the Timepix3 detectors, respectively for a fixed value of the current intensity and then for a fixed value of the tube voltage.

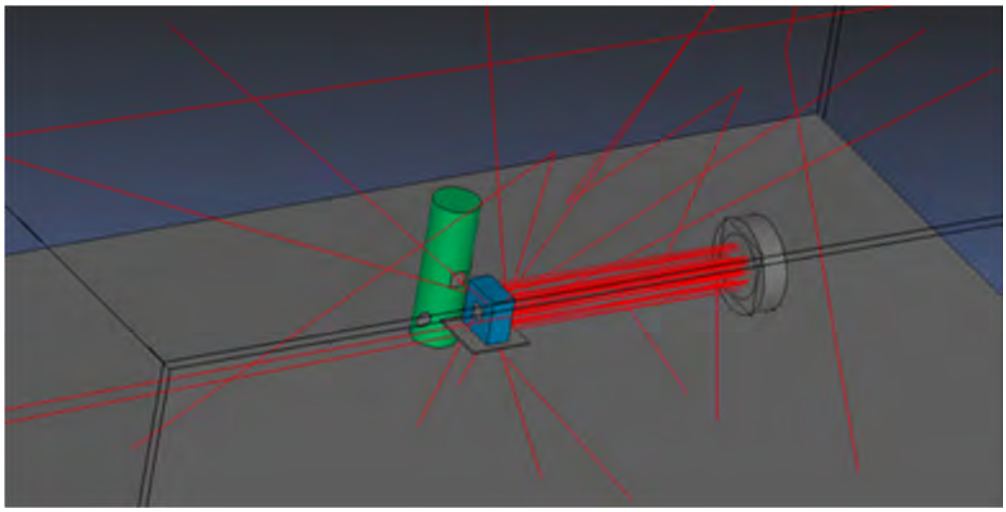

Figure 22 - Simulation of the scattered radiation filed in the room around the water phantom (in blue). The green cylinder represents the anthropomorphic phantom.

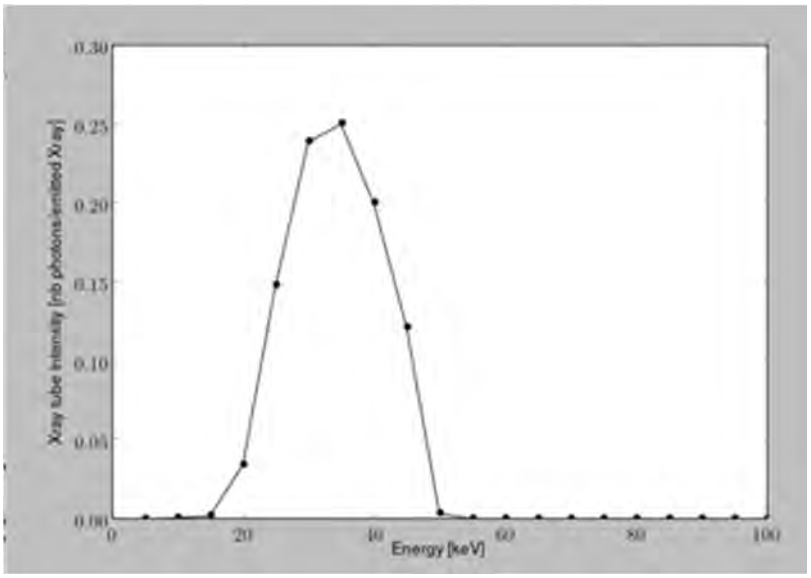

Figure 23 - Simulation by MC code of the spectrum of the primary beam at the tube exit for 50 kV.

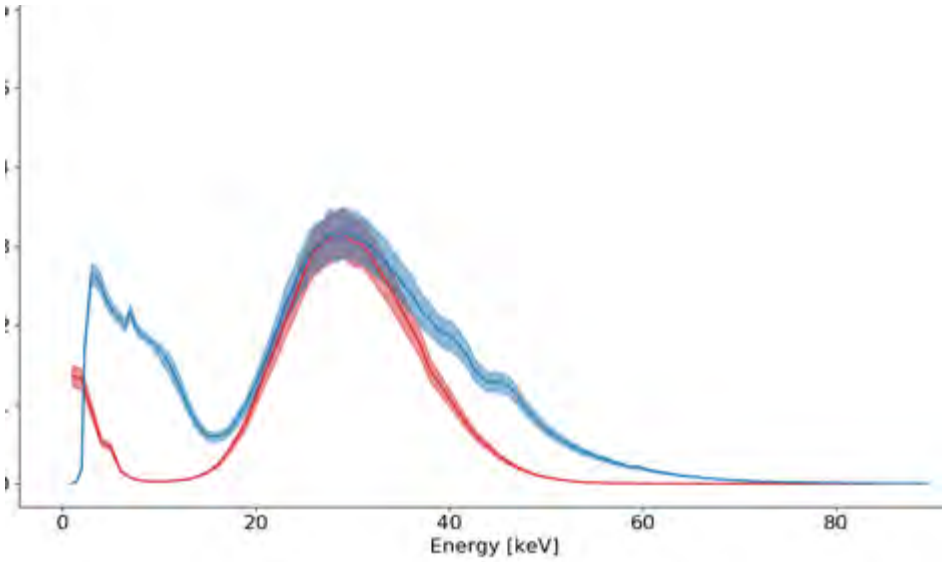

Figure 24 - Simulation by MC code of the spectra on the Timepix3 detector without pixel sharing or detector efficiency, correction in red. Spectra measured by Timepix3 in blue for 100 kV – 500 mAs. Light blue or light red curves represent the uncertainty.

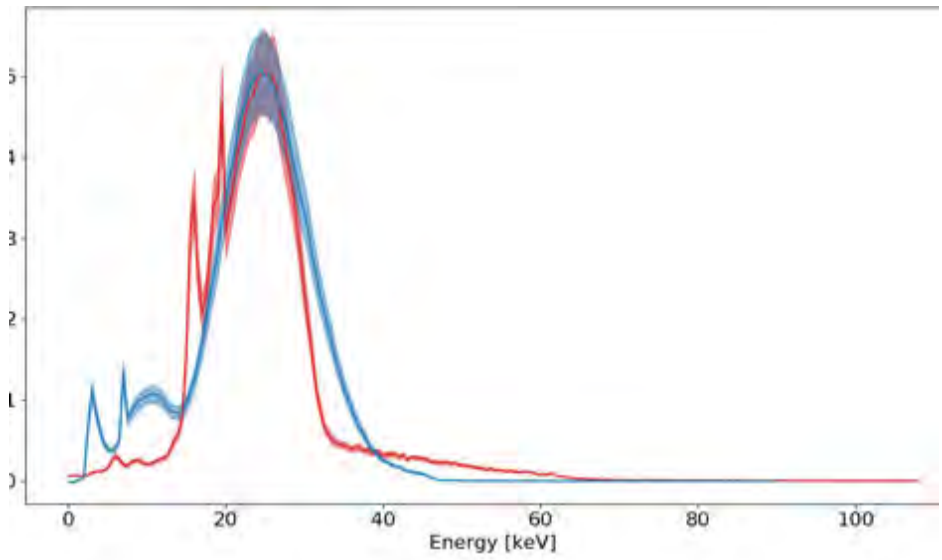

Figure 25 - Measured spectra by Falcon 5000 in red, and Timepix3 in blue for 40 kV, 500 mAs. Light blue or light red curves represent the uncertainty.

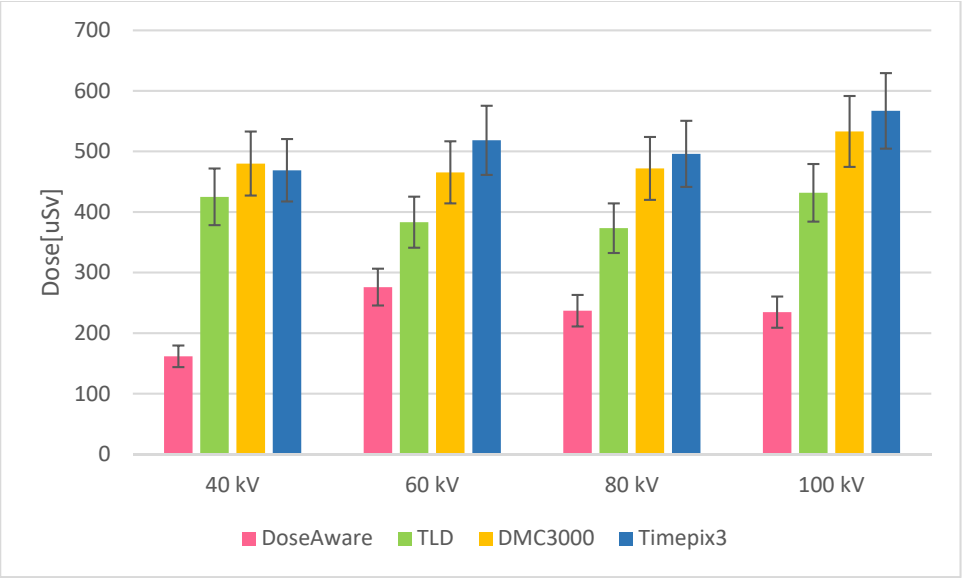

Figure 26 - Dose comparison between DoseAware (pink), TLD (green), DMC3000 (yellow) and Timepix3 (blue) detectors. For different tube voltage, 500 mAs.

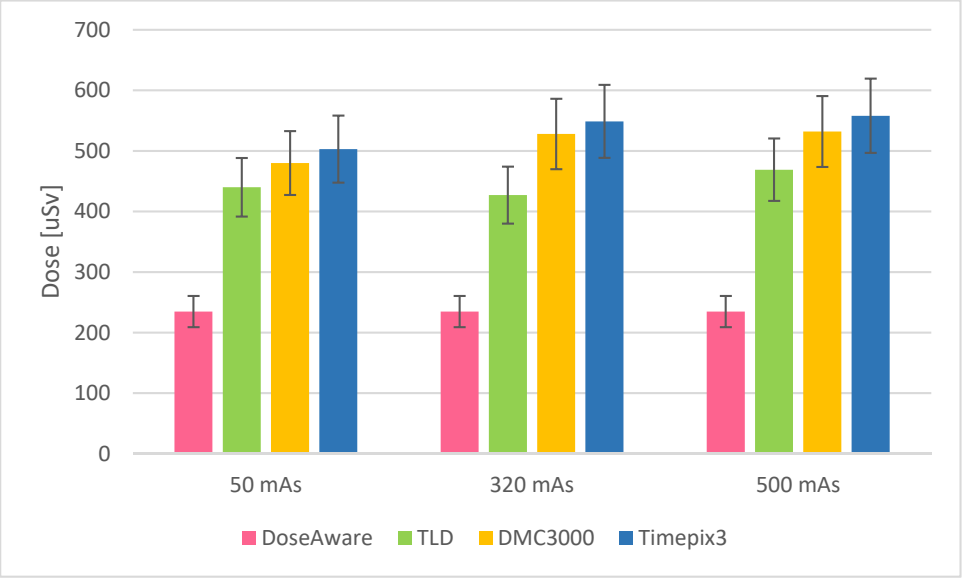

Figure 27 - Dose comparison between DoseAware (pink), TLD (green), DMC3000 (yellow) and Timepix3 (blue) detectors. For different tube current intensities at 100 kV.

3.5.3 Discussion

The simulated spectra of the primary beam was in good agreement with the spectra measured by Fewell [21]. The measurements made with the Timepix3 were consistent with the MC simulations and validated the spectrum obtained with the Timepix3 in the scattered radiation field. The spectrum simulated and measured in the scattered radiation field peaked at 8 keV, which does not exist in the simulation of the primary beam. This peak is due to the reaction of the copper present in Timepix3, which creates a fluorescence peak at 8 keV. The spectrum

measured by the Timepix3 is presented without correction for pixel sharing or detector efficiency, so as to compare it to the one measured with the Falcon 5000 instrument which was not calibrated for this purpose. Furthermore, only spectra for a voltage of 40 kV are presented. Beyond that, measuring the spectrum by the Falcon was impossible due to the saturation of the detector. As Cormack, Marshall, or Bhat *et al.* [30–32] a spectral measurement by the Falcon would require a great collimation of the beam, thus preventing the obtaining of information on fluence and therefore the impossibility of measuring a dose.

If DoseAware dosimeters are an easy to handle pedagogic tool, the dose measured by these dosimeters is underestimated on average by a factor of two compared to the TLD. These dosimeters tend to get in the stand-by mode if the wearers are stationary, and its response in pulsed fields is incorrect. This is in agreement with the study published by Hope.O *et al*. [50]. The dose recorded by the Timepix3 is 1% to 35% higher than the one obtained with other dosimeters. The Timepix3 might overestimate the dose, the dose calculation has to be further optimise.

3.5.4 Conclusion

The measurements finalize the work of adapting a HPD into a dosimeter. The purpose of these measurements was to link the spectra obtained with an HPD to a dose, and to make a comparison with other dosimeters used frequently at hospitals. These measurements were confirmed via MC simulations of spectra as well as a comparison of spectra obtained with the Timepix3 and the Falcon used as spectrometers. The Timepix3 HPD seems suitable for dosimetry purposes. This dosimeter based on spectral information should respond to the ICRP and the ICRU requirements.

4 Discussion

This PhD thesis work focused on the adaptation of an HPD to a dosimeter based on fluence and energy spectra information in hospitals theatres.

The first study for this work was conducted with the support of the FOPH and confirmed that it is possible, for a large majority of cases, to use the routine dosimeter worn on the chest level to ensure that the equivalent dose to the eye lens remains below the annual limit. Respecting the 20 mSv limit with the $H_p(0.07)$ dose measured with double dosimetry does ensure a respect of the annual eye lens dose limit, but does not provide an accurate dose assessment. The results also show a large variation between the values measured by the routine badge dosimeter and the specific dosimeter placed near the eye lens, drawing attention to an inhomogeneous irradiation of the body. The first part of the article supports the fact that an international comparison of doses is complicated in view of the disparate legislation between countries [59].

The measurements in clinical conditions show that for IR, angioplasty, surgery and pain treatment services if compliance with the whole-body dose limit is respected on the badge, then it will be also respected for the eye lens. On the other hand, the urology practice showed numerous measures where the dose to the eye lens was greater than the dose to the whole body. For this specialty, compliance with the dose to the whole body does not ensure compliance with the dose to the eye lens.

The great disparity in ratios, for a given service or even for a given practitioner, does not make it a useful tool for estimating the eye lens dose from the badge data. Thus, when the whole body dose is exceeded, it will not be possible to know the dose received by the eye lens.

The fact that the measured equivalent dose is close to the annual limit for a non-negligible fraction of staff in IR indicate that there is a need for an additional specific dosimeter. Alongside this clinical observation, both the ICRU and the ICRP have proposed introducing new dosimetric quantities based on the radiation fluence. Several working groups emerged across Europe and are running projects to design new dosimetric monitoring methods.

To address this need for a dedicated dosimeter and the adaptation of the dosimetric quantities, we propose using an HPD working in the single-photon counting mode.

In order to verify the possibility of using an HPD in a medical environment, the initial phase of the project was to perform the first measurements with a Timepix3 using reference beam qualities. Spectra obtained without correction (for detector efficiency or sharing pixel) are in

agreement with spectra simulated by the MC method before any correction. This study has shown that the Timepix3 has many advantages compared to commercially available spectral detectors. HPGe detectors require strong collimation [30–32]. These detectors also require cooling with liquid nitrogen, and a great distance from the radiation source in order to lower the fluence on the sensor. The Timepix3 does not require any collimation in the scattered radiation, that would later affect the measurement of the fluence. This advantage makes it possible to capture photons having different solid angles and enables us to consider the Timepix3 as a spectral dosimeter. Measurements in the scattered radiation field show that with the energies of the medical environment and the fluences present in the IR theatre, the detector may be fully operated even close to the radiation source, unlike the HPGe detector. Like the HPGe, the Timepix3 detector requires a cooling system but a small fan is enough to dissipate the heat created by the chip, and keep it at a stable temperature. The measurements done during the initial stage validate the proof of concept. The analysis was performed using the TOT information.

This first series of measurements proves that the Timepix3 allows spectrum measurements in primary and in scattered radiation fields. However, the primary radiation field brings the detector to saturation and no longer allows a correct measurement of the fluence even if the spectra shape is respected. An evolution of the ASIC in order to take into account a greater number of hits per cm^2 per second, would allow to use this detector in the primary radiation field, and to obtain spectral information directly at the exit of the tube for example. In addition, this detector could be used for pulsed field measurements since its data integration speed is higher than the pulse used in the IR room.

Moreover, the material used for the sensor could be adapted for a future detector. Indeed, the choice of Si was made here to guarantee greater stability of the detector and avoid photon escape by fluorescence. A CdTe sensor would allow an absorption efficiency of 87% at 60 keV against 4% for Si. The choice of the materials will have to be studied since if the choice of a CdTe sensor had to be made, the algorithm for calculating the reconstruction of the photon energy will then have to be increased to compensate for the 80 to 87% photon loss by fluorescence compare to 4% for Si.

The second step of the project was to calibrate the detector to be able to measure the energy spectrum and to do a full characterisation of the detector to understand the response in terms of heat, light, energy, and angle. The HPD used in this study is calibrated for an energy range from 2 keV compare to 16 keV for dosimeter actually used in hospital.

The third article of this thesis work demonstrated that HPDs like the Timepix3 allow to characterise the scattered radiation field in an IR theatre. The first results presented the energy

spectra of the scattered radiation field at the positions where the medical staff stand in an IR theatre. The MC simulations of the scattered radiation requires a good knowledge of the primary X-ray beam and the geometry of the theatre. The type and amount of filtration used in recent radiological installations are not well documented. Experimental verification of simulations is therefore crucial. The results that were obtained in the present work confirmed that personnel exposure is strongly inhomogeneous near the X-ray source and smooths out the further one is from the source. These results also enabled us to identify a shift in energy from head to toe for the person standing near the patient.

Our presentation of these results to the medical team reinforced their awareness of radiation protection. This study included creating an exposure map in the theatre at four heights: at knee, belt, chest, and eye lens level.
The energy spectra obtained in the room also demonstrated the need for an energy correction suitable for currently used dosimeters. Using the Timepix3 as a dosimeter would overcome this type of dependence.

The detector in its current composition can be used to make spectral measurements in theatre. However, this process is still time consuming. The validation of the concept allows to work with the Medipix and KT collaboration to develop a new detector, more compact, lighter and no longer requiring cooling. This future detector could thus be used as a personal dosimeter, or even be integrated into protective glasses, which is not yet possible at present. The coupling of the ASIC to a wireless communication system would allow data analysis in real time and guide the medical team during their procedures for protective purposes.

A team works in parallel on a detector call Dosepix, which is part of the Medipix family [78]. However compared to the Timepix3, this detector has a matrix of only 16 x 16 pixels against 256 x 256 for the Timepix3, and the energy spectrum can only be obtained for 16 energy bins. As the Dosepix is more compact, the future detector could be adapted according to this model by keeping a fine matrix to allow an energy spectrum with energy bin of 1 keV.

The last part of the project aimed at calculating the dose from the energy spectra obtained with the Timepix3 detector. A comparison with other active and passive dosimeters validated the functioning of the Timepix3 as a dosimeter.

Finally, the Timepix3 HPD meets the needs of the ICRU and the ICRP for fluence-based dosimetry. We presented the results of this work to EURADOS's Working Group 12, which focuses on fostering initiative and contributing to innovations and improving patient and staff dosimetry assessment.

5 Conclusion

In the context of the impact analysis while reassessing the risk factors for cataract induction during chronic exposure to ionizing radiation, it appeared that the medical situation posed a problem. The risk management faced new challenges for certain health professionals. Indeed, although the previous annual eye lens dose limit was unlikely to be exceeded, even for professionals performing many procedures under fluoroscopic guidance, the new limit was critical in particular for radiologists or cardiologists performing therapeutic procedures. The first study carried out as part of this work confirmed this fact and also highlighted that urologists are at risk as they use a particular geometry with an over-couch X-ray tube during their endoscopic surgery requiring fluoroscopy.

In this context, academic societies recommend a significant improvement of the dosimetry for the personnel who must stand close to the patient and the fluoroscopy equipment. This applies to radiologists, cardiologists as well as all the personnel working in the operating theatre since many surgical procedures require the use of X-ray equipment.

On the one hand, improving dosimetry requires developing a strategy which enables an efficient, yet pragmatic, surveillance of the professionals, and on the other hand, improving how dose is estimated based on physics and the spectral characteristics of the scattered radiation field. In Switzerland, it was first proposed to estimate eye lens exposure using the values obtained from values reported by the personal dosimeter worn on the protective apron at chest level. Our measurements, as well as a review of the literature, show that, in general, this approach is conservative except for some categories of professionals, such as urologists, where this evaluation can underestimate the doses received by the eye lens. A working group of the Swiss Society of Radiobiology and Medical Physics is currently working on the possibility of introducing correction factors for each category of personnel to improve the estimation of the dose to the eye lens by the dosimeter worn at chest level. The heart of the work carried out within the framework of this thesis concerns this part.

Determining X-ray energy spectra remains cumbersome and a true challenge since commercially available detectors are not adapted for the specific environment and cannot cope with the instantaneous fluences involved with fluoroscopy equipment. Furthermore, they are often fragile and must be operated with an associated cooling system, which limits their use in a medical context... The aim of this work was to investigate whether a HPD detector developed by the high energy physicist community at the CERN, initially for identifying trajectories of charged particles and then adapted for photon counting imaging, could be transfered to the medical field and provide a valuable breakthrough in hospital radiation protection and medical

physics. The first phase of the work was done in collaboration with the CERN Medipix team to select the appropriate sensor material for the energy range of interest. The second phase focused on the full characterisation of the detector's performance when measuring X-ray energy spectrum for relevant beam qualities. The results obtained show that the detector is suited to the problem of improving dosimetry surveillance. Finally, in the last phase, the detector was used in a clinical context to verify that it was compatible with the instantaneous fluence levels encountered in medical theatres where fluoroscopic-guided interventions are performed. This last work demonstrated that the shape of the spectra differs slightly from spectra found in the literature, published many years ago based on MC simulations. The results indicate notable variations of the energy spectrum and fluence within the theatre depending upon the position where the measurements are taken.

Thus, the objective of the work, which aimed to better characterize the spectra of scattered radiation field near a patient exposed during a procedure guided by radioscopy was achieved.

6 Perspectives

The proof of concept for the use of the Timepix3 to characterise the scattered radiation field generated by a patient during a fluoroscopy examination has been achieved. The results show that the detector calibration curve is similar to those published by Burian *et al*. [79], in spite of the fact that the relationships are detector specific. One of the advantages of the Timepix3 is its sensitivity to low energy photons when compared to other options. It can provide data from 2 keV as opposed to 16 keV for other dosimeters, which makes it a promising tool for dosimetry. During this study, the Timepix3 was also used to assess the effectiveness of the radiation protection means (leaded screen and leaded table shield) available for the staff in hospital theatres. As expected, a dose reduction by factors in the range of 100 was obtained, and the beam hardening effects produced by those protective devices could be clearly observed. The presentation of the results to the medical team helped raise their awareness and improved their understanding of the radiation protection options available for ensuring their safety. This means that the Timepix3 could be used not only to characterize spectra but also as a pedagogical tool.

The last series of measurements enabled us to improve the dose estimation in a representative radiological scattered radiation field using the energy spectra data collected. Comparisons with other active and passive dosimeters (such as DMC3000 or TLDs) have shown that the doses obtained with the Timepix3 led to slightly higher values (in the range of 10%). This result shows that current dose estimations are reasonably precise and generally do manage to protect the staff but there are ways to further improve the present situation.

Timepix3 HPD meets the requirements of ICRU and ICRP concerning the fluence-based dosimetry. Working group 12 from EURADOS is already interested in the measurements made with this specific dosimeter. One of the next challenges will be adapt the present ICRU and ICRP converting factors with the actual data provided when taking advantage of the spectral data provided by such a detector.

During our study, we mainly focused on the eye lens exposure and characterised scattered radiation around a patient imaged with a fluoroscopy unit aiming at improving the absorbed dose quantity. Taking into account the clinical context where dose limit can be easily exceeded this appeared to us quite an important matter. The improvement of the effective dose delivered to the staff using ambient spectral data when dealing with the dose monitoring over and under the lead apron with appropriate dosimetry would improve the scientific rational of the staff monitoring.

References

[1] Vereinte Nationen. Report of the United Nations Scientific Committee on the Effects of Atomic Radiation 2010: fifty-seventh session. New York: United Nations; 2011.

[2] Le Coultre R, Bize J, Champendal M, Wittwer D, Trueb P, Verdun FR. Exposition de la population suisse aux rayonnements ionisants en imagerie médicale en 2013. 2013.

[3] FOPH. Audits in the OR-areas of Swiss Hospitals. 2020.

[4] Sánchez RM, Vano E, Fernández JM, Rosales F, Sotil J, Carrera F, et al. Staff Doses in Interventional Radiology: A National Survey. J Vasc Interv Radiol 2012;23:1496–501. https://doi.org/10.1016/j.jvir.2012.05.056.

[5] Chodick G, Bekiroglu N, Hauptmann M, Alexander BH, Freedman DM, Doody MM, et al. Risk of cataract after exposure to low doses of ionizing radiation: a 20-year prospective cohort study among US radiologic technologists. Am J Epidemiol 2008;168:620–31. https://doi.org/10.1093/aje/kwn171.

[6] Ciraj-Bjelac O, Rehani MM, Sim KH, Liew HB, Vano E, Kleiman NJ. Risk for radiation-induced cataract for staff in interventional cardiology: is there reason for concern? Catheter Cardiovasc Interv Off J Soc Card Angiogr Interv 2010;76:826–34. https://doi.org/10.1002/ccd.22670.

[7] Rehani MM, Vano E, Ciraj-Bjelac O, Kleiman NJ. Radiation and cataract. Radiat Prot Dosimetry 2011;147:300–4. https://doi.org/10.1093/rpd/ncr299.

[8] Vano E, Kleiman NJ, Duran A, Rehani MM, Echeverri D, Cabrera M. Radiation cataract risk in interventional cardiology personnel. Radiat Res 2010;174:490–5. https://doi.org/10.1667/RR2207.1.

[9] ICRP 2011 Statement on tissue reactions.

[10] RS 814.501 Ordonnance du 26 avril 2017 sur la radioprotection (ORaP). https://www.admin.ch/opc/fr/classified-compilation/20163016/index.html.

[11] RS 814.501.43 Ordonnance du DFI du 26 avril 2017 sur la dosimétrie individuelle et la dosimétrie de l'environnement (Ordonnance sur la dosimétrie) https://www.admin.ch/opc/fr/classified-compilation/20163018/index.html.

[12] Silberstein L. XXXIV. Spectral composition of an X-ray radiation determined from its filtration curve. Lond Edinb Dublin Philos Mag J Sci 1933;15:375–94. https://doi.org/10.1080/14786443309462192.

[13] Mayneord WV, Roberts JE. The "Quality" of High Voltage Radiations. I. Br J Radiol 1935;8:341–64. https://doi.org/10.1259/0007-1285-8-90-341.

[14] Twidell JW. The determination of X-ray spectra using attenuation measurements and a computer program. Phys Med Biol 1970;15:529. https://doi.org/10.1088/0031-9155/15/3/013.

[15] Sundararaman V, Prasad MA, Vora RB. Computed spectra from diagnostic and therapeutic X-ray tubes. Phys Med Biol 1973;18:208. https://doi.org/10.1088/0031-9155/18/2/004.

[16] Stanton L, Lightfoot DA, Mann S. A Penetrameter Method for Field kV Calibration of Diagnostic X-Ray Machines. Radiology 1966;87:87–98. https://doi.org/10.1148/87.1.87.

[17] Peaple LHJ, Burt AK. The measurement of spectra from X-ray machines. Phys Med Biol 1969;14:73. https://doi.org/10.1088/0031-9155/14/1/005.

[18] Seelentag WW, Panzer W, Drexler G, Platz L, Santner F. A catalogue of spectra for the calibration of dosemeters. Gesellschaft fuer Strahlen- und Umweltforschung m.b.H.; 1979.

[19] Birch R, Marshall M. Computation of bremsstrahlung X-ray spectra and comparison with spectra measured with a Ge(Li) detector. Phys Med Biol 1979;24:505–517. https://doi.org/10.1088/0031-9155/24/3/002.

[20] Israel HI, Lier DW, Storm E. Comparison of detectors used in measurement of 10 to 300 keV X-ray spectra. Nucl Instrum Methods 1971;91:141–57. https://doi.org/10.1016/0029-554X(71)90650-1.

[21] Fewell TR, Shuping RE. Photon energy distribution of some typical diagnostic x-ray beams. Med Phys 1977;4:187–97. https://doi.org/10.1118/1.594364.

[22] Epp ER, Weiss H. Experimental Study of the Photon Energy Spectrum of Primary Diagnostic X-Rays. Phys Med Biol 1966;11:225–38. https://doi.org/10.1088/0031-9155/11/2/302.

[23] Castro ED, Pani R, Pellegrini R, Bacci C. The use of cadmium telluride detectors for the qualitative analysis of diagnostic x-ray spectra. Phys Med Biol 1984;29:1117. https://doi.org/10.1088/0031-9155/29/9/008.

[24] Kurková D, Judas L. X-ray tube spectra measurement and correction using a CdTe detector and an analytic response matrix for photon energies up to 160 keV. Radiat Meas 2016;85:64–72. https://doi.org/10.1016/j.radmeas.2015.12.008.

[25] Terini RA, Costa PR, Furquim TAC, Herdade SB. Measurements of discrete and continuous X-ray spectra with a photodiode at room temperature. Appl Radiat Isot 1999;50:343–54. https://doi.org/10.1016/S0969-8043(97)10123-3.

[26] Compton AH. The Spectrum of Scattered X-Rays. Phys Rev 1923;22:409–13. https://doi.org/10.1103/PhysRev.22.409.

[27] Phys. Rev. 21, 483 (1923) - A Quantum Theory of the Scattering of X-rays by Light Elements. https://journals.aps.org/pr/abstract/10.1103/PhysRev.21.483.

[28] Zagorska A, Bliznakova K, Buchakliev Z. Towards the estimation of the scattered energy spectra reaching the head of the medical staff during interventional radiology: A Monte Carlo simulation study. J Phys Conf Ser 2015;637:012036. https://doi.org/10.1088/1742-6596/637/1/012036.

[29] McCaffrey JP, Tessier F, Shen H. Radiation shielding materials and radiation scatter effects for interventional radiology (IR) physicians: Radiation shielding materials and radiation scatter for IR. Med Phys 2012;39:4537–46. https://doi.org/10.1118/1.4730504.

[30] Cormack DV, Griffith TJ, Johns HE. Measurement of the Spectral Distribution of Scattered 400 kVp X Rays in a Water Phantom. Br J Radiol 1957;30:129–35. https://doi.org/10.1259/0007-1285-30-351-129.

[31] Marshall NW, Faulkner K, Warren H. Measured scattered x-ray energy spectra for simulated irradiation geometries in diagnostic radiology. Med Phys 1996;23:1271–6. https://doi.org/10.1118/1.597690.

[32] Bhat M, Pattison J, Bibbo G, Caon M. Diagnostic x-ray spectra: A comparison of spectra generated by different computational methods with a measured spectrum. Med Phys 1998;25:114–20. https://doi.org/10.1118/1.598170.

[33] Minamoto A, Taniguchi H, Yoshitani N, Mukai S, Yokoyama T, Kumagami T, et al. Cataract in atomic bomb survivors. Int J Radiat Biol 2004;80:339–45. https://doi.org/10.1080/09553000410001680332.

[34] Nakashima E, Neriishi K, Minamoto A. A reanalysis of atomic-bomb cataract data, 2000-2002: a threshold analysis: Health Phys 2006;90:154–60. https://doi.org/10.1097/01.HP.0000175442.03596.63.

[35] Cucinotta FA, Manuel FK, Jones J, Iszard G, Murrey J, Djojonegro B, et al. Space radiation and cataracts in astronauts. Radiat Res 2001;156:460–6.

[36] Chylack LT, Peterson LE, Feiveson AH, Wear ML, Manuel FK, Tung WH, et al. NASA study of cataract in astronauts (NASCA). Report 1: Cross-sectional study of the relationship of exposure to space radiation and risk of lens opacity. Radiat Res 2009;172:10–20. https://doi.org/10.1667/RR1580.1.

[37] Worgul BV, Kundiyev YI, Sergiyenko NM, Chumak VV, Vitte PM, Medvedovsky C, et al. Cataracts among Chernobyl clean-up workers: implications regarding permissible eye exposures. Radiat Res 2007;167:233–43.

[38] Clarke RH, Valentin J. The History of ICRP and the Evolution of its Policies. Ann ICRP 2009;39:75–110. https://doi.org/10.1016/j.icrp.2009.07.009.

[39] Authors on behalf of ICRP, Stewart FA, Akleyev AV, Hauer-Jensen M, Hendry JH, Kleiman NJ, et al. ICRP publication 118: ICRP statement on tissue reactions and early and late effects of radiation in normal tissues and organs--threshold doses for tissue reactions in a radiation protection context. Ann ICRP 2012;41:1–322. https://doi.org/10.1016/j.icrp.2012.02.001.

[40] Ciraj-Bjelac O, Ciraj-Bjelac O, Rehani M, Minamoto A, Sim KH, Liew HB, et al. Radiation-Induced Eye Lens Changes and Risk for Cataract in Interventional Cardiology. Cardiology 2012;123:168–71. https://doi.org/10.1159/000342458.

[41] Auvinen A, Kivelä T, Heinävaara S, Mrena S. Eye Lens Opacities Among Physicians Occupationally Exposed to Ionizing Radiation. Ann Occup Hyg 2015;59:945–8. https://doi.org/10.1093/annhyg/mev022.

[42] Alnaaimi M, Alkhorayef M, Omar M, Abughaith N, Alduaij M, Salahudin T, et al. Occupational radiation exposure in nuclear medicine department in Kuwait. Radiat Phys Chem 2017;140:233–6. https://doi.org/10.1016/j.radphyschem.2017.02.048.

[43] Nowak M, Sans-Merce M, Lemesre C, Elmiger R, Damet J. Eye lens monitoring programme for medical staff involved in fluoroscopy guided interventional procedures in Switzerland. Phys Med 2019;57:33–40. https://doi.org/10.1016/j.ejmp.2018.12.001.

[44] OFSP O fédéral de la santé publique. Rapports annuels Radioprotection et Dosimétrie.

[45] FOPH. Personal Dosimetry Services. https://www.bag.admin.ch/bag/en/home/gesund-leben/umwelt-und-gesundheit/strahlung-radioaktivitaet-schall/dosimetrie-berufliche-strahlenexposition/personendosimetriestellen.html.

[46] OFSP. Radioprotection et surveillance de la radioactivité en Suisse Résultats 2018.

[47] Horowitz YS. Thermoluminescence and Thermoluminescent Dosimetry, v. 1 1984.

[48] DMC 3000 Dosimètre électronique personnel. Mirion. https://v2.mirion.com/produits/.

[49] Ciraj-Bjelac O, Carinou E, Vanhavere F. Use of active personal dosimeters in hospitals: EURADOS survey. J Radiol Prot 2018;38:702–15. https://doi.org/10.1088/1361-6498/aabce1.

[50] Hupe O, Friedrich S, Vanhavere F, Brodecki M. Determining the dose rate dependence of different active personal dosemeters in standardized pulsed and continuous radiation fields. Radiat Prot Dosimetry 2019:ncz173. https://doi.org/10.1093/rpd/ncz173.

[51] Fisher DR, Fahey FH. Appropriate use of effective dose in radiation protection and risk assessment. Health Phys 2017;113:102–9. https://doi.org/10.1097/HP.0000000000000674.

[52] Jacobi W. The concept of the effective dose--a proposal for the combination of organ doses. Radiat Environ Biophys 1975;12:101–9.

[53] ICRP. Draft Joint Report of ICRU and ICRP for Consultation: Operational Quantities for External Radiation Exposure.

[54] Kim JO, Kim JK. Dose Equivalent Per Unit Fluence near the Surface of the ICRU Phantom by Including the Secondary Electron Transport for Photons. Radiat Prot Dosimetry 1999;83:211–20. https://doi.org/10.1093/oxfordjournals.rpd.a032675.

[55] Personal dose equivalent conversion coefficients for photons to 1 GeV | Radiation Protection Dosimetry | Oxford Academic. https://academic.oup.com/rpd/article/145/1/28/1600187.

[56] ICRU 1998. Conversion Coefficients for Use in Radiological Protection against External Radiation. ICRU Rep 57 1998.

[57] Otto T, Hertel NE, Bartlett DT, Behrens R, Bordy J-M, Dietze G, et al. The ICRU Proposal for New Operational Quantities for External Radiation. Radiat Prot Dosimetry 2018;180:10–6. https://doi.org/10.1093/rpd/ncx243.

[58] Mayer S, Baechler S, Damet J, Elmiger R, Frei D, Giannini S, et al. Occupational exposure to external radiation in switzerland. Radiat Prot Dosimetry 2016;170:433–6. https://doi.org/10.1093/rpd/ncw048.

[59] Martin CJ. Personal dosimetry for interventional operators: when and how should monitoring be done? Br J Radiol 2011;84:639–48. https://doi.org/10.1259/bjr/24828606.

[60] Code du travail - Article R4451-111. vol. R4451-111. n.d.

[61] Carinou E, Ferrari P, Bjelac OC, Gingaume M, Merce MS, O'Connor U. Eye lens monitoring for interventional radiology personnel: dosemeters, calibration and practical aspects of H p (3) monitoring. A 2015 review. J Radiol Prot 2015;35:R17. https://doi.org/10.1088/0952-4746/35/3/R17.

[62] An information system for occupational dosimetry registration. https://siseri.irsn.fr/about-siseri.

[63] SFRP. Fiche technique SFRP - Cristallin : Limites réglementaires, mesure, dosimétrie et suivi médical 2016.

[64] Medipix collaboration. Medipix website. Medipix 2017.

[65] Heijne EHM. Semiconductor micropattern pixel detectors: a review of the beginnings. Nucl Instrum Methods Phys Res Sect Accel Spectrometers Detect Assoc Equip 2001;465:1–26. https://doi.org/10.1016/S0168-9002(01)00340-0.

[66] Alexeev G, Andersen E, Andrighetto A, Antinori F, Armenise N, Ban J, et al. First results from the 1994 lead beam run of WA97. Nucl Phys A 1995;590:139–46. https://doi.org/10.1016/0375-9474(95)00232-P.

[67] Ballabriga R, Campbell M, Llopart X. Asic developments for radiation imaging applications: The medipix and timepix family. Nucl Instrum Methods Phys Res Sect Accel Spectrometers Detect Assoc Equip 2018;878:10–23. https://doi.org/10.1016/j.nima.2017.07.029.

[68] Lutz G. Semiconductors. In: Lutz G, editor. Semicond. Radiat. Detect. Device Phys., Berlin, Heidelberg: Springer; 2007, p. 7–38. https://doi.org/10.1007/978-3-540-71679-2_2.

[69] Vähänen S, Tick T, Campbell M. Low-cost bump bonding activities at CERN. J Instrum 2010;5:C11008–C11008. https://doi.org/10.1088/1748-0221/5/11/C11008.

[70] Ballabriga R. The Design and Implementation in 0.13um CMOS of an Algorithm Permitting Spectroscopic Imaging with High Spatial Resolution for Hybrid Pixel Detectors. Universitat Ramon Llull, 2009.

[71] Llopart X, Ballabriga R, Campbell M, Tlustos L, Wong W. Timepix, a 65k programmable pixel readout chip for arrival time, energy and/or photon counting measurements. Nucl Instrum Methods Phys Res Sect Accel Spectrometers Detect Assoc Equip 2007;581:485–94. https://doi.org/10.1016/j.nima.2007.08.079.

[72] Pinsky LS, Idarraga-Munoz J, Kroupa M, Son HM, Stoffle NN, Semones EJ, et al. Medipix in space on-board the ISS. J Radiat Res (Tokyo) 2014;55:i62–3. https://doi.org/10.1093/jrr/rrt197.

[73] Turecek D, Pinsky L, Jakubek J, Vykydal Z, Stoffle N, Pospisil S. Small Dosimeter based on Timepix device for International Space Station. J Instrum 2011;6:C12037–C12037. https://doi.org/10.1088/1748-0221/6/12/C12037.

[74] Walsh MF, Opie AMT, Ronaldson JP, Doesburg RMN, Nik SJ, Mohr JL, et al. First CT using Medipix3 and the MARS-CT-3 spectral scanner. J Instrum 2011;6:C01095. https://doi.org/10.1088/1748-0221/6/01/C01095.

[75] Krejci F, Jakubek J, Kroupa M, Bruza P, Panek D. Pixel detector Timepix operated in pile-up mode for pulsed imaging with ultra-soft X-rays. J Instrum 2012;7:C12013–C12013. https://doi.org/10.1088/1748-0221/7/12/C12013.

[76] Ballabriga R, Alozy J, Campbell M, Frojdh E, Heijne EHM, Koenig T, et al. Review of hybrid pixel detector readout ASICs for spectroscopic X-ray imaging. J Instrum 2016;11:P01007–P01007. https://doi.org/10.1088/1748-0221/11/01/P01007.

[77] International Electrotechnical Commission. Medical diagnostic X-ray equipment-Radiation conditions for use in the determination of characteristics.;IEC 61267:1994.

[78] Zang A, Anton G, Ballabriga R, Bisello F, Campbell M, Celi JC, et al. The Dosepix detector—an energy-resolving photon-counting pixel detector for spectrometric measurements. J Instrum 2015;10:C04015–C04015. https://doi.org/10.1088/1748-0221/10/04/C04015.

[79] Burian P, Broulím P, Jára M, Georgiev V, Bergmann B. Katherine: Ethernet Embedded Readout Interface for Timepix3. J Instrum 2017;12:C11001–C11001. https://doi.org/10.1088/1748-0221/12/11/C11001.

[80] ICRP 2007. The 2007 Recommendations of the International Commission on Radiological Protection. ICRP Publication 103. Ann ICRP 37.:2–4.

[81] ICRP 1977. Recommendations of the ICRP. ICRP Publication 26. Ann ICRP 1 3.

[82] CC 814.501 Radiological Protection Ordinance of 26 April 2017 (RPO). https://www.admin.ch/opc/en/classified-compilation/20163016/index.html.

[83] Mayles P, Nahum A, Rosenwald JC, Papanikolaou N. Handbook of Radiotherapy Physics: Theory and Practice. vol. 35. n.d.

[84] Berger MJ, Hubbell JH. XCOM: Photon Cross Sections Database. NIST 2009.

Paper I

Eye lens monitoring programme for medical staff involved in fluoroscopy guided interventional procedures in Switzerland

Published in Physica Medica (January 2019)

M.Nowak, M.Sans-Merce, C.Lemesre, R.Elmiger, J.Damet

Physica Medica 57 (2019) 33–40

Contents lists available at ScienceDirect

Physica Medica

journal homepage: www.elsevier.com/locate/ejmp

Original paper

Eye lens monitoring programme for medical staff involved in fluoroscopy guided interventional procedures in Switzerland

Marie Nowak[a,b,*], Marta Sans-Merce[a,c], Camille Lemesre[a], Raphael Elmiger[d], Jérôme Damet[a,b,e]

[a] Institute for Radiation Physics, Lausanne University Hospital, Lausanne, Switzerland
[b] CERN, European Organization for Nuclear Research, Switzerland
[c] Department of Medical Imaging and Information Sciences, Geneva University Hospitals, Geneva, Switzerland
[d] Federal Office of Public Health FOPH, Bern, Switzerland
[e] Department of Radiology, University of Otago, Christchurch, New Zealand

ABSTRACT

Epidemiological studies indicate that radiation damages to the eye lens occurs at lower dose values than previously considered (Worgul et al., 2007; Chodick et al., 2008; Ciraj-Bjelac et al., 2010; Rehani et al., 2011; Vano et al., 2010) [1–5]. The International Commission on Radiological Protection lowered the equivalent dose limit value for the eye lens to 20 mSv/year (ICRP, n.d.) [6]. This new limit has been incorporated into the revised Swiss legislation [7]. Prior this change, it was agreed that if the effective dose limit was respected it would implicitly imply the respect of the limit to the eye lens, for penetrating radiation. The concept had to be reviewed in the light of necessary application of the new eye lens dose limit. The new Swiss legislation proposes to use the value of $H_p(0.07)$ measured over the protective apron to estimate the eye lens dose.

This study aims to investigate the validity of this approach for medical staff during fluoroscopy guided procedures. The results show that the ratio between thorax and eye lens doses varies greatly from one medical speciality to another, but also between surgeons within the same speciality. Moreover, for a given physician, the ratio varied over the periods of surveillance. Those variations confirmed the crucial influence of external parameters related to experience, practice and workload. The surveillance method is appropriate for most of the procedures performed in the department included in this study. Nevertheless, for the particular configuration in urology, the respect of the effective dose limit measured by the routine dosimetry does not allow direct compliance with the dose limit to the eye lens, unless appropriate protective eye wear gear are worn.

1. Introduction

The sensitivity of the eye lens to ionising radiation has been clearly demonstrated with numerous studies based on large epidemiological datasets [2–5]. The follow up of the Hiroshima and Nagasaki cohort highlighted a significant increase in the rate of diagnosed cases of partial or total opacity of the eye lens [8]. The International Commission on Radiological Protection (ICRP) introduced the annual dose equivalent to the eye lens at 300 mSv in 1977 [9]. The epidemiological study of the liquidators who intervened immediately on the scene of the Chernobyl accident helped to better understand the mechanisms behind the progressive opacity of the eye lens [1]. These observations were corroborated with studies on astronauts, that suggest low-dose-induced effects, challenging the initial hypothesis that the occurrence of induced radio-cataract is only valid for high doses [10,11]. This was also confirmed by studies on physicians working in interventional radiology [12,13].

Based on the growing epidemiological evidence, the occupational dose limit value for the eye lens was adapted accordingly. The limit originally set to 300 mSv was reduced to 150 mSv in 1991 [14]. With former recommendations, the eye lens dose limit was well above the whole-body dose limit, for penetrating radiation only. It was thus generally agreed that the whole-body dosimetry guaranteed compliance with the eye lens dose limit [15], and a general consensus appears amongst authorities regarding the absence of a dedicated surveillance programme for the eye lens dosimetry. The latest exposure limit value was lowered in 2011 to 20 mSv on a five-year average [6,16], equal to the limit for the whole body and thus imposing the development of a dedicated surveillance programme [7]. The design and application of a suitable dosimetry monitoring method is a matter of importance and is the subject of numerous studies in Europe [17,18].

This major change in dose limit is of high interest and concern in hospitals. The medical personnel using fluoroscopy equipment can be particularly close to the patient, having their eyes lens exposed to an inhomogeneous scattered radiation field. In these conditions, the location of the dosimeter is critical to obtain a representative estimate of the eye lens dose [19]. There is no national or international consensus yet on where the dosimeter should be worn. The analysis carried out by

* Corresponding author.
E-mail address: marie.nowak@cern.ch (M. Nowak).

https://doi.org/10.1016/j.ejmp.2018.12.001
Received 24 January 2018; Received in revised form 18 October 2018; Accepted 5 December 2018
Available online 18 December 2018

a working group of the European EURADOS network indicates though that the best position for eye lens routine dosimetry is as close as possible to the eye, and, if possible, in contact with the skin, oriented towards the radiation source [17]. If eye protection gears are used, the dosimeter should be placed under them. If this is not feasible, the dosimeter should be placed on the protection; an additional reduction factor should then be determined. Another methodology to evaluate the eye lens dose is to place an additional dosimeter above the protective apron as proposed by the IAEA [19]. This methodology would be acceptable only for homogeneous fields [7], though this is not the case for a large majority of the personnel in the medical sector. In the case of inhomogeneous exposure, the ratio between the eye lens dose and the dose measured on the apron is extremely hard to determine and depends on many parameters that are difficult to quantify: type of procedure, personal habits, exact location of dosimeters, protective measures taken, etc. However, a range of values for the ratio between the dose to the eye lens and the dose measured by the dosimeter on the apron is available in the literature for interventional radiology, interventional cardiology and some nuclear medicine procedures [20–33].

The eye lens dose monitoring also presents a significant metrological challenge. The International Commission on Radiological Units and Measurements (ICRU) recommends the use of a specific quantity by introducing the quantity $H_p(3)$ [13,33]. In practice in Switzerland, almost no dosimetry service is able to assess the eye lens dose in terms of $H_p(3)$ and alternative methods based on $H_p(0.07)$ are proposed [17,19].

The aim of this study is to evaluate the concept of the routine eye lens dose monitoring that is proposed in the recently revised Swiss Radiological Protection Ordinance and in the corresponding Dosimetry Ordinance that has come in force on January 1st, 2018 [7]. The new Swiss Dosimetry Ordinance stipulates that the dosimetry of the eye lens should be monitored using a suitable dosimeter [7]. The text describes a practical and pragmatic solution for a homogeneous exposure, easily applied by companies and dosimetry services, while ensuring an effective monitoring.

The second chapter of the ordinance stipulates that the equivalent dose to the eye lens is assumed to be equal to the individual dose on the surface, $H_p(0.07)$, measured by the whole body dosimeter. In the case of inhomogeneous radiation fields for which the whole body dose is not representative of the eye lens dose, the surveillance authority may require specific eye lens dosimeters to be worn on a case-by-case basis. Within this legal context, our study helps the local radiation protection team to identify the sectors concerned by an extra dosimeter, specific for eye lens dosimetry, at the Lausanne University Hospital (CHUV).

This study is based on the measurement of the operational quantity $H_p(0.07)$, measured with the whole body dosimeter. A first series of measurements was done with phantoms, under controlled geometrical conditions, (*i.e.* specific X-Ray tube position, and define radiation protection gears) choosing the best representative conditions for each given medical speciality. These measurements are important to estimate the correction factors to be applied between dosimeters worn at several positions in static conditions. A second set of measurements was done with dosimeters placed on medical staff using fluoroscopy equipment in services of diagnostic and interventional radiology, angioplasty, surgery, urology and pain treatment centre. Surgeons were equipped with whole body dosimeters placed on the thorax under and over the lead apron and, with a dedicated dosimeter taped on their protective glasses, closest as possible to the eye lens. The study provides the basis to define a specific eye lens dose measurement method for the different categories of persons at-risk for which their professional activity could lead to exceed the annual limit.

2. Materials and Methods

2.1. Individual dosimetry monitoring

2.1.1. Badge

The Swiss Dosimetry Ordinance stipulates that the supervisory authority may require that two dosimeters should be worn, on the chest, for work involving high doses carried out with a protective apron [7], one over and the other under the protective apron. All the staff participating in this study was introduced with double dosimetry in case this modality was not yet available.

The Swiss Dosimetry Ordinance define the $H_p(10)$ and $H_p(0.07)$ calculation of follow [34]:

$$H_p(10) = H_{p_{under}}(10) + a \cdot H_{p_{above}}(10) \quad (1)$$

$$H_p(0.07) = H_{p_{under}}(0.07) + H_{p_{above}}(0.07) \quad (2)$$

where $H_{p_{under}}$ represents the dose indicated by the dosimeter placed under the apron and $H_{p_{above}}$ the dose of the dosimeter placed on the apron; a = 0.1 when no thyroid protective collar is worn and a = 0.05 if it is worn. The use of dosimeters under the lead apron, take into account the possibility for the medical staff to received dose during procedure where the lead apron is not mandatory.

The dosimeters used for this study were the whole body routine dosimeters provided by the dosimetry service of the Institute of Radiation Physics (IRA) (Fig. 1). Whole body dosimeters provide data for the operational quantities $H_p(10)$ and $H_p(0.07)$. The first chip was used to measure the deep dose equivalent with a filter of 1.8 mm Al and 0.4 mm PE, while the second was used to measure the shallow dose equivalent with a filter of 0.07 mm PETD-Al. The IRA's dosimeters use Thermo Luminescence Detector (TLD) LiF-100 type: Mg, Cu, P. The results of interest for this study were provided in terms of $H_p(0.07)$ calibrated using a Cs-137 reference source. In addition to those dosimeters, single TLD (LiF: MCP-N, Mg, Cu, P) pellets were used for measurements on phantoms either in individual tight plastic bags or strips as shown in Fig. 2. The $H_p(10)$ value measured with the dosimeters is not taken into account.

The values presented in this study correspond to the routine $H_p(0.07)$ values as transmitted to the national dose register. No specific correction regarding angular or energy response of the dosimeter was done on raw data in order to evaluate the method under realistic routine conditions.

2.1.2. Eye lens dosimetry

When using $H_p(0.07)$, measured with the dosimeter worn on the chest over the apron to estimate the eye lens dose, the local radiation protection expert must determine an individual correction factor if protective glasses are worn. This correction factor needs the consent of the supervisory authority and is then communicated to the individual dosimetry service in order to calculate the dose to the eye lens from the formula below:

Fig. 1. Routine badge dosimeter used for this study, based on two TLD pellets.

Fig. 2. Single TLD pellet in individual bag (left), TLD pellets in a plastic strip (right).

$$H_{eyelens}(0.07) = f_c * H_p(0.07) \quad (3)$$

where f_c is the attenuation factor of the protection. The determination of the protection effectiveness of glasses used in the hospital is at this stage beyond the scope of the study and is thus not considered in this article.

The purpose of this study is to investigate a possible correlation between the $H_p(0.07)$ routine measurement and the eye lens dose. For this purpose, in addition to the whole body dosimeters previously described, we used the eye lens routine dosimeters (Dosiris) of the Institute of Radiation protection and Nuclear Safety (IRSN) in France. The eye lens dosimeter, placed as closed as possible to the eye lens, provide data for the operational quantity $H_p(3)$. Dosiris dosimeter use TLD 7LiF: Mg, Ti. IRSN provided results in terms of $H_p(3)$ calibrated for an energy of 118 keV (beam quality N150) [35].

In order to evaluate the method under realistic routine conditions, this study was based on routine measurement results that do not require any specific correction on the dosimeter read-out signal.

2.1.3. Measurements under controlled conditions

Measurements were first performed in controlled conditions, with phantoms, in a radiological room to determine geometric correction factors for a given configuration (see Fig. 3). The position of the phantoms and the X-ray tube were set to mimic as close as possible the characteristic position during a standard procedure for identified cases.

An Alderson RANDO anthropomorphic phantom (model 200, RSD, USA) was used to represent medical personnel during irradiations in controlled conditions. A container filled with water together with Vinyl Polychoride cylinders and a skull phantom were used to simulate the patient, generating the scattered radiation field.

Measures under controlled conditions were performed with a fluoroscopic imaging system from Siemens (Artis zee), used with the parameters recommended by the local medical staff. The settings were the following: a tube tension of 70 kV_p, a current intensity of 199.3 mA, a square field of 30 cm × 30 cm and 7.5 images per second.

The same irradiation was repeated several times to reach a dose in the mSv level, in order to reduce uncertainties. An active dosimeter (mirion DMC 3000) was placed on the chest phantom to monitor the exposure range.

The RANDO phantom representing the physician was equipped with several dosimeters (Table 1) on the thorax, the thyroid, the forehead, the temples and the eyes as illustrated on Figs. 4 and 5. A strip of 11 TLD pellets, interspaced every 2 cm and labelled numbered from left to right from 0 to 20, was placed on the forehead.

The measurements done at different positions on the head were performed to check that the measurements on the forehead are indeed representative of the eye lens dose and to evaluate the dose distribution on the forehead to check where the highest dose is expected.

In order to do dose measurements close to the reality, different radioprotection gears were used, and are summarized in Table 2. The choice to use these protections was done by following the practices observed at the hospital.

Table 1
Reference position and identification of the dosimeters. Dosiris dosimeter worn on the left side, to be closer to the X-Ray tube [18].

Type of dosimeter	Position on the phantom			Reference name
Badges	Chest	Left	Under apron	B. 4
			Above apron	B. 3
		Right	Above apron	B. 2
	Thyroid	Centre	Above apron	B. 1
TLD	Eye	Right		A.2
		Left		A.3
	Temple	Right		A.1
		Left		A.4
TLD (strip of 3 chips)	Chest	Left	Under the left badge above apron	C
TLD (strip of 11 chips)	Forehead	Left to right		TLD Frontal strip
Dosiris	Close to the eye	Left		Dosiris

Fig. 4. Reference position of dosimeters.

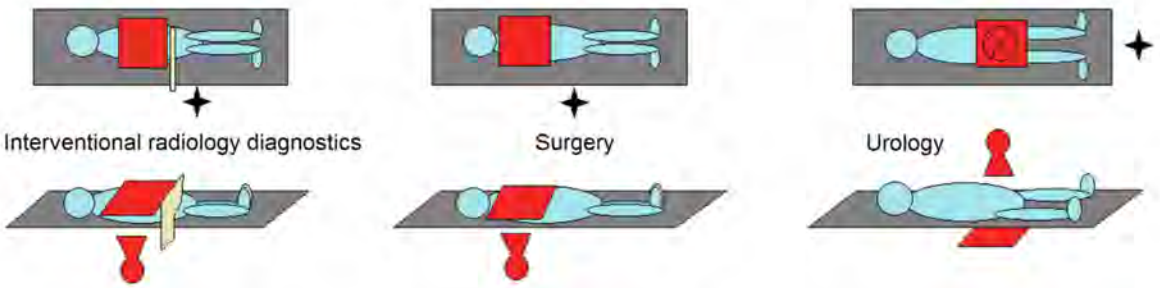

Fig. 3. Configurations used under controlled conditions. The cross represents the position of the physician; the red shapes around the patient represent the X-ray tube and the detector. The yellow frame represents a mobile protective gear. (For interpretation of the references to colour in this figure legend, the reader is referred to the web version of this article.)

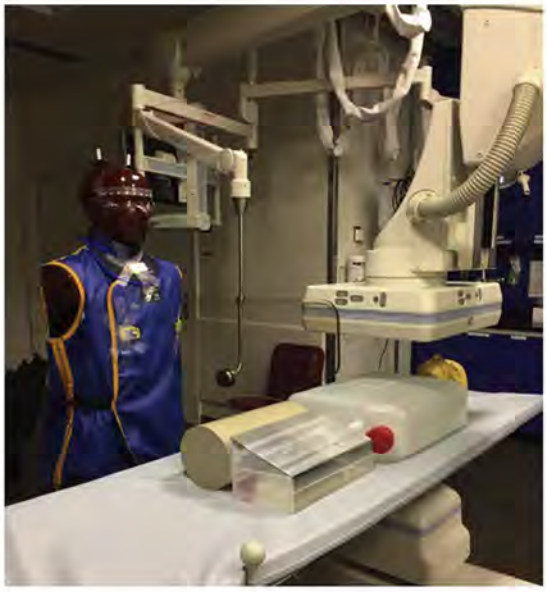

Fig. 5. Position of the phantoms and dosimeters during the measurements in the radiological room.

Table 2
Radiation protection gear used for the different speciality. "+" represent the use of the protection and "−" the unused. All thickness in this table are lead equivalent between 50 and 110 kV_p.

	Screen	Lead Apron	X-Ray tube position
Diagnostic and Interventional radiology	+ 0.5 mm	+ 0.25 mm	Under the table
Surgery	− −	+ 0.25 mm	Under the table
Urology	− −	+ 0.25 mm	Above the table

2.1.4. Measurements in clinical procedures

Twenty-one physicians from five services at CHUV participated in this study over a four-months period that took place between beginning of August until the end of November 2016. The number of physicians in each sector is given in Table 3. Each physician had a set of two badge dosimeters placed on the left chest, one under and one over the apron, to ensure the routine surveillance by double dosimetry and a Dosiris dosimeter. The eye lens dosimeter was taped on the external side of the left arm of the protective eyewear (Fig. 6) or worn with a solid headband provided by IRSN. Routine measurements were done according the habit of each practitioner, and with radiation protection gear present in each room (screen or skirt leaded). The kit was collected and exchanged each month.

2.2. Calculation of the correction factor

The purpose of this part of the study is to determine a correction factor to assess the eye lens dose based on the $H_p(0.07)$ value measured at the thorax. In order to comply with standard conditions of use, we assumed that $H_p(3)$ measured on the temple was the eye lens dose, while $H_p(0.07)$ was the dose on the thorax. The correction factor k is defined as the ratio of the dose received to the eye lens $H_p(3)_{Dosiris}$ and the dose measured in terms of $H_p(0.07)$ at the thorax level over the apron:

$$k = \frac{H_p(3)_{Dosiris}}{H_p(0.07)} \quad (4)$$

The relative uncertainty on the measurement of the absorbed dose by the TLD pellets is calculated according to the internal procedure [36] and following the Guide to the expression of uncertainty in measurement (GUM) [37] and does not exceed 10% at $k = 2$.

The relative uncertainty for measurements by Dosiris dosimeters is indicated on the IRSN measurement certificate, maximum 50% for energies below 118 keV.

Table 3
Number of physicians by service equipped with dosimeters for the study.

Service	Number of physicians
Diagnostic and Interventional radiology	8
Angioplasty	6
Surgery	3
Pain treatment centre	2
Urology	2

Fig. 6. Typical position of the Dosiris dosimeter taped on protective glasses.

3. Results

3.1. Measurements under controlled conditions

A colour-coded schematic representation of the distribution of the dose on the forehead is shown on Fig. 7 for the three given services, *i.e.* diagnostic and interventional radiology, surgery and urology. The ratio of the $H_p(0.07)$ dose measured on the chest and the $H_p(3)$ close to the eye is summarised in Table 4. Selected ratios were highlighted to better understand the dose difference between dosimeters or localisations.

The doses measured with the TLD pellet on the strips placed on the forehead, which is closest to the eye are consistent with the doses measured with the single TLD pellet directly taped on the eye. The best agreement is found for urology between the TLD on position 8 on the strip and the eye, with a difference of 3.4%. The largest difference, 17%, is observed for the surgery between the TLD on position 8 on the strip and the eye. The largest difference is less than 20%.

Moreover, a strip of 3 TLDs was placed under the chest dosimeter to study the dose distribution, and to see if the position of the passive dosimeter has a significant influence on the k ratio. However, with dose uncertainties in the measurements, it could not be demonstrated that such a small change in position significantly modified the dose on the chest badge.

3.2. Measurements during clinical procedures

The kit of dosimeters supplied to the physicians at CHUV provided data for an estimation under routine conditions with a representative clinical workload during the four-month period of this study. The values of the correction factors k (Eq. (4)) obtained for each physician in a service are compiled and presented Fig. 8. It can be seen that for the departments of diagnostic and interventional radiology, angioplasty, surgery and the pain treatment centre the set of values k is less than 1, however there is one value higher than 1, which was later explained by

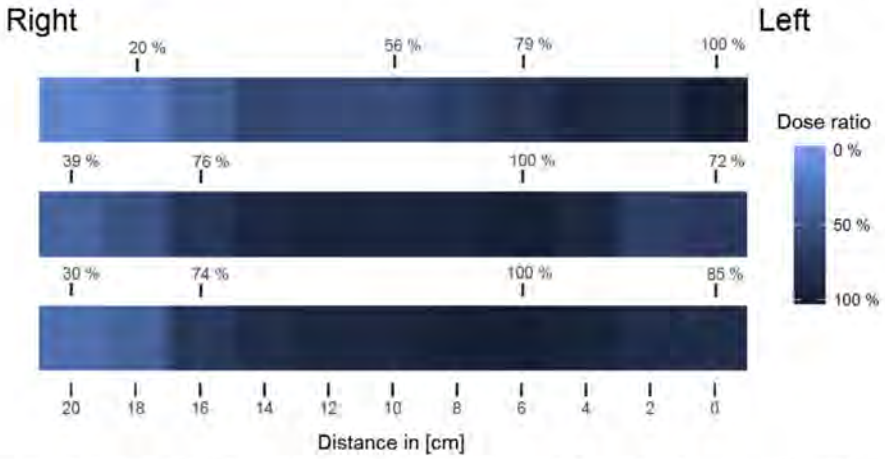

Fig. 7. Dose gradient measured by the TLD band placed on the forehead for (from top to bottom) diagnostic and interventional radiology, surgery, urology. For each medical speciality, the highest dose was used as reference for normalisation.

Table 4
Ratio between the most important dosimeter for different departments. k (Eq. (1)) is the ratio between $H_p(3)$ Dosiris and $H_p(0.07)$ which correspond to the dose calculation (Eq. (2)) with the badge under and above the lead apron. A. 2 and A. 3 correspond to the right and left eye dose, respectively, while A. 4 is the left temple dose. B.1 is $H_p(0.07)$ on the collar badge.

Ratio	Diagnostic and interventional radiology	Surgery	Urology
k= Dosiris/$H_p(0.07)$	0.39	0.28	0.72
A. 3/Dosiris	1.20	1.48	0.87
A. 4/Dosiris	1.37	1.24	0.82
B.1/Dosiris	3.14	0.91	0.89
A.2/A. 3	0.79	0.91	0.92
TLD Frontal strip8/$H_p(0.07)$	0.42	0.36	0.6
A.3/$H_p(0.07)$	0.47	0.42	0.62

a malpractice to a practitioner. The lowest end of the span can be explained by the workload of the person involving activities outside theatre (i.e. without protective glasses thus without the Dosiris dosimeter). The factor k shows a large span of variation for the urology department with values greater than 1.

All data from physicians in the same service are represented in a

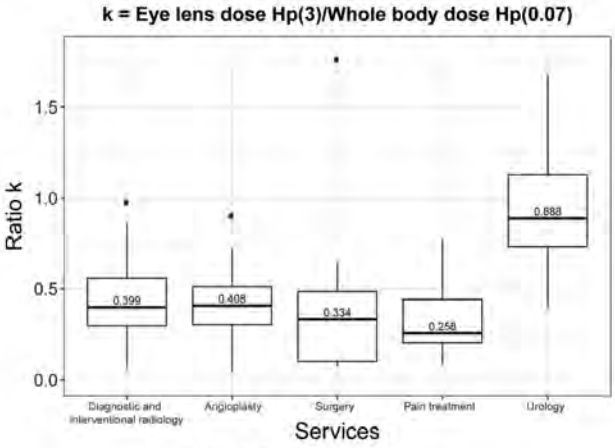

Fig. 9. k-ratio by services.

boxplot format on Fig. 9. The lower limit of the rectangle corresponds to the 25th percentile, while the upper limit corresponds to the 75th percentile. The horizontal line indicates the median value. The segments at the ends of the rectangle indicate the extreme values. In these

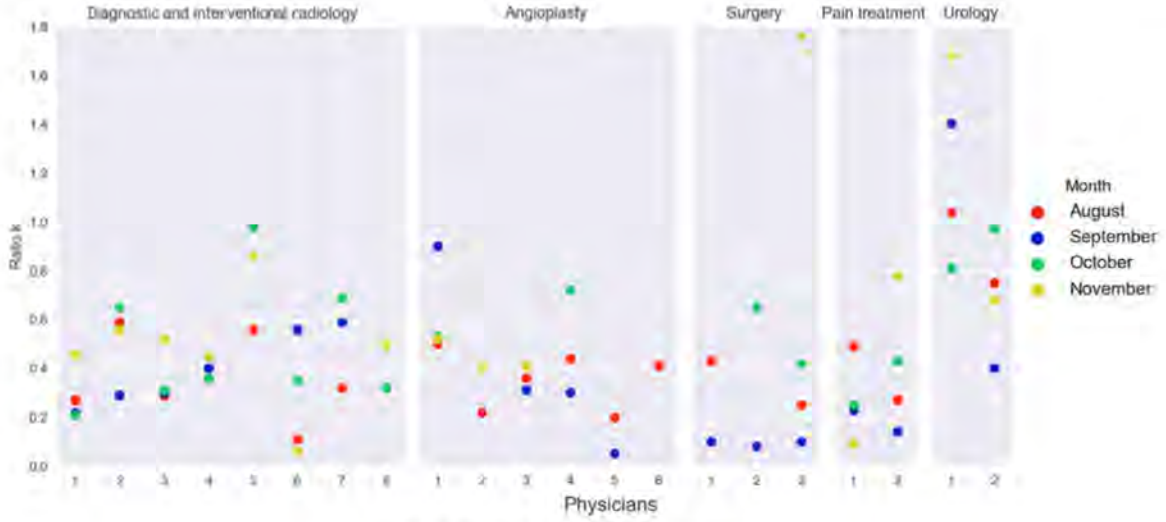

Fig 8. k-ratio for each physician, by service.

figures, points represent the atypical values (values greater than 1.5 times the height of the box).

For departments of diagnostic and interventional radiology, angioplasty, surgery and pain treatment centre, the median values of k are under the unity which indicates that the dosimeter placed on the chest over the lead apron receives a higher dose than the one situated near the eye lens. The urology department presents a maximal value above one, whereas the median value is close to one, while remaining lower.

4. Discussion

Results obtained with the strips positioned on the forehead of the phantom clearly indicate an asymmetric dose gradient with a maximum on the left side of the skull for diagnostic and interventional radiology, and a maximum dose above the left eye for surgery and urology. The dose distribution can be explained for each service by the position of the phantom towards the X-ray tube and the orientation towards the patient. This support the work of S. Principi et al. [38]. As shown Table 4, measurements under controlled conditions indicate that Dosiris dosimeter underestimated the dose received by the eye lens by a factor 1.48 in the worst case for surgery.

The doses measured with the TLD pellet show a good correlation between the dose obtained on the eye, A.2 and A. 3, and the one above the eye TLD 12 and TLD 8 respectively, on the forehead. This indicates that a dosimeter worn on the forehead, above the eye, would be appropriate for a measurement of the eye lens dose. This approach however faces the reluctance of physicians to wear an additional dosimeter on their forehead on a routine basis. Physicians are yet willing to join occasionally dedicated specific studies.

The Swiss approach requires no modification of the existing personal dosimetry system. An alternative option based on the possible use of an active personal dosimeters requires an adequate training of the staff and more complex data acquisition systems and data analysis treatment tools [39,40]. This approach is though an interesting alternative and could be used in the future.

The difference of the k value measured on the phantom and the median k value obtained with the medical staff during clinical procedures is below 20% for both diagnostic and interventional radiology and surgery services. The difference is less than 23% for the urology service. This indicates that the local radiation protection team may estimate the eye lens dose when new procedures are introduced as well as the efficiency of protective gears with phantom-based measurements.

The ICRP recommended wearing an additional dosimeter at collar level and above the thyroid protective collar [41]. The recommendation was also made by the Eurados working group [17]. Our results in controlled conditions support this recommendation and indicate that the dose values measured on the thyroid level are closer in absolute value to those measured by the Dosiris dosimeter than the dose values measured with the badge placed on the thorax. However, results summarised in Table 4 show a large variation of the ratio collar dose on eye lens dose. Doses measured at the thyroid may be lower than the eye lens dose measured by the Dosiris dosimeter. Indeed, a ratio of 3.14 is observed for the diagnostic and interventional radiology. This difference could be explained by the choice of the different radioprotection gears in the theatre. This indicates that the measurement on the thyroid cannot be used on its own to ensure the respect of the dose limit on the eye lens and requires the determination of a correction factor to correctly assess the eye lens dose [17,42]. An article of Tom Jupp et al. [43] goes in this direction, they found a ratio between eye lens dose and collar dose above one for nurse and radiographer in cardiology. A limit not to exceed on the collar could be set to ensure compliance with the dose limit to the eye lens. However, with the Swiss approach, even though we can't provide a very accurate value for the eye lens dose, we make sure that the limit is not exceeded. Doses measured by the standard routine procedure, *i.e.* with an additional dosimeter on the chest level and above the protective apron, may also, albeit seldom, be lower than the eye lens dose measured by the Dosiris dosimeter. Besides, this approach gets the slight advantage that it does not require any change from the user, as s/he can continue to wear the dosimeter on the chest as s/he is used to do for the double dosimetry that is now in practice for many years in CHUV.

The k ratio remains below unity for services of diagnostic and interventional radiology, angioplasty, surgery and the pain treatment centre, and indicates that a dosimetric surveillance based on the routine dosimetry can ensure the respect of the eye lens dose limit as long as the cumulative $H_p(0.07)$ is below 20 mSv per year. This observation is consistent with the Yoshihiro Haga et al. conclusion's [44], but also with the results of Alejo et al. [45] who found a factor of 0.33 and 0.40 in paediatric interventional cardiology. Only one practitioner in the surgery service had a ratio above unity, and this was explained by the fact that s/he informed that s/he forgot to wear the routine dosimeter. This shows that in practice the constant wearing of two dosimeters is problematic and cannot be guaranteed. Moreover, the last ratio Table 4 (left eye/$H_p(0.07)$) always below one, although impossible to test in clinical condition, support the fact that the routine chest badge would be an appropriate dosimetry to verify the respect of the eye lens dose limit.

A large variation of the k factor can be observed between staff members within a given service. For instance, a ratio of 0.06 is found for a given surgeon in the diagnostic and interventional radiology service, while a ratio fourteen times larger, 0.86, is found for another surgeon over the same period. This variation can also be seen with the wide spread of the box plot for some physicians on Fig. 9.

Furthermore, a large variation of the k factor can be observed for a given physician over the time (Fig. 8). For instance, the k factor calculated for physician number 6 of the diagnostic and interventional radiology service spans from 0.06 to 0.56 for the four months period of this study.

The median value of the k factor for the urology service is close to unity (0.89) while it is below 0.5 for the four other services. This value is consistent with the dose ratio of 0.9 ± 0.4 reported by Medici et al. [46], and higher than the dose ratio of 0.5 ± 1.2 reported by Vano et al. [33]. The higher value of the k factor in urology can be explained by the specific configuration of the procedures with the position of the x-ray tube above the patient, witch is also clearly specify for Medici et al.

The use of lead glasses would help, despite a factor k sometimes greater than 1 in urology, compliance with the eye lens dose limit. Indeed, their effectiveness makes it possible to reduce the dose received to the eye lens by a factor 3 to 7, depending on the model [47,42]. Moreover, Principi et al. [38] showed that depending on the position of the practitioner, the dose to the eye lens could be reduced. In the same way, the use of lead screen as ceiling suspended, according to the ORAMED project [42], can reduce the eye lens dose up to 90% for a wearer of lead glasses.

Although conducted conscientiously, this study presents some limitations. Firstly, measures were carried out only in a single hospital, and did not include all the trades working with ionising radiation. Secondly, the data were only collected on 21 workers and over a period of 4 months. Finally, as the scope of the study was to collected data during routine intervention, the effect of the radiation protection gears was not measured separately.

5. Conclusion

These measurements under routine conditions with a typical clinical workload indicate that the determination of an average correction factor to correctly assess the eye lens dose from a dosimeter worn on the chest is complex. High variations on the correction factors are obtained coming from the high dependency of these factors on the type of procedures, personal habits, the precise position of the routine dosimeters and the use of addition radiation protection gears. It is thus not possible

to accurately estimate the received dose to the eye lens from the routine dosemeter placed at the chest level over the apron measuring the quantity $H_p(0.07)$. However, the study showed that for services with a standard configuration, (*i.e.* the X-ray tube placed under the patient) it is possible to use this routine dosemeter to verify the respect of the eye lens dose limit. In other words, the respect of the routine dose limit $H_p(0.07)$ measured with double dosimetry ensures the respect of the annual eye lens dose limit. Contrariwise, in some fields of activity, such as urology, more in-depth studies will have to be carried out in order to find a way to ensure compliance with the lens dose limit without protective eye wear gears.

Our study confirms the validity of the Swiss approach for eye lens dosimetry. Nonetheless, if the annual dose limit on the badge were to be exceeded, there is as yet no reliable means of calculating the dose received by the eye lens. In fact, in the absence of a dedicated dosimeter, close to the eye lens, Switzerland will face the same challenges as its European partners for a precise measurement of the dose to the eye lens. Our study also confirms that eye lens dosimetry poses a major challenge for the years to come both in metrology and operational radiation protection, as also shown by Zagorska et al. [48]. It must be noticed that the new dosimetry ordinance accommodates these limitations by giving the supervisory authority the possibility to demand a dedicated eye lens dosimeter when measurements with the routine dosimeter aren't suitable to monitor the dose limit.

Acknowledgements and disclaimer

The authors would like to thank the members of the medical staff who participated in this study. The authors also would also like to acknowledge the many valuable suggestions made by Dr. C. Bailat, head of the metrology group and the helpful advice on various technical issues given by N. Cherbuin from the radiation protection group at the institute of radiation physics.

This research project has been partly supported by the Swiss Federal of Public Health under the contract N° 16.010049/434.0000/-170 for *Evaluation der neuen Bestimmungen zur Überwachung der Augenlinsendosis.*

References

[1] Worgul BV, Kundiyev YI, Sergiyenko NM, Chumak VV, Vitte PM, Medvedovsky C, et al. Cataracts among Chernobyl clean-up workers: implications regarding permissible eye exposures. Radiat Res 2007;167:233–43.
[2] Chodick G, Bekiroglu N, Hauptmann M, Alexander BH, Freedman DM, Doody MM, et al. Risk of cataract after exposure to low doses of ionizing radiation: a 20-year prospective cohort study among US radiologic technologists. Am J Epidemiol 2008;168:620–31. https://doi.org/10.1093/aje/kwn171.
[3] Ciraj-Bjelac O, Rehani MM, Sim KH, Liew HB, Vano E, Kleiman NJ. Risk for radiation-induced cataract for staff in interventional cardiology: is there reason for concern? Catheter Cardiovasc Interv Off J Soc Card Angiogr Interv 2010;76:826–34. https://doi.org/10.1002/ccd.22670.
[4] Rehani MM, Vano E, Ciraj-Bjelac O, Kleiman NJ. Radiation and cataract. Radiat Prot Dosimetry 2011;147:300–4. https://doi.org/10.1093/rpd/ncr299.
[5] Vano E, Kleiman NJ, Duran A, Rehani MM, Echeverri D, Cabrera M. Radiation cataract risk in interventional cardiology personnel. Radiat Res 2010;174:490–5. https://doi.org/10.1667/RR2207.1.
[6] ICRP 2011 Statement on tissue reactions n.d.
[7] Ordonnance du DFI sur la dosimétrie individuelle et la dosimétrie de l'environnement; 2018.
[8] Minamoto A, Taniguchi H, Yoshitani N, Mukai S, Yokoyama T, Kumagami T, et al. Cataract in atomic bomb survivors. Int J Radiat Biol 2004;80:339–45. https://doi.org/10.1080/09553000410001680332.
[9] ICRP. Recommendations of the ICRP. ICRP Publication 26. Ann ICRP 1977;3:1977.
[10] Chylack LT, Peterson LE, Feiveson AH, Wear ML, Manuel FK, Tung WH, et al. NASA study of cataract in astronauts (NASCA). Report 1: cross-sectional study of the relationship of exposure to space radiation and risk of lens opacity. Radiat Res 2009;172:10–20. https://doi.org/10.1667/RR1580.1.
[11] Cucinotta FA, Manuel FK, Jones J, Iszard G, Murrey J, Djojonegro B, et al. Space radiation and cataracts in astronauts. Radiat Res 2001;156:460–6.
[12] The 2007 Recommendations of the International Commission on Radiological Protection. ICRP publication 103. Ann ICRP 2007; 37:1–332. doi:10.1016/j.icrp.2007.10.003.
[13] Matsubara K, Lertsuwunseri V, Srimahachota S, Krisanachinda A, Tulvatana W, Khambhiphant B, et al. Eye lens dosimetry and the study on radiation cataract in interventional cardiologists. Phys Med 2017;44:232–5. https://doi.org/10.1016/j.ejmp.2017.10.007.
[14] 1990 Recommendations of the International Commission on Radiological Protection. Ann ICRP 1991;21:1–201.
[15] Ciraj-Bjelac O, Carinou E, Ferrari P, Gingaume M, Merce MS, O'Connor U. Occupational exposure of the eye lens in interventional procedures: how to assess and manage radiation dose. J Am Coll Radiol 2016;13:1347–53. https://doi.org/10.1016/j.jacr.2016.06.015.
[16] Stewart FA, Akleyev AV, Hauer-Jensen M, Hendry JH, Kleiman NJ, MacVittie TJ, et al. ICRP PUBLICATION 118: ICRP statement on tissue reactions and early and late effects of radiation in normal tissues and organs – threshold doses for tissue reactions in a radiation protection context. Ann ICRP 2012;41:1–322. https://doi.org/10.1016/j.icrp.2012.02.001.
[17] Carinou E, Ferrari P, Bjelac OC, Gingaume M, Merce MS, O'Connor U, et al. Eye lens monitoring for interventional radiology personnel: dosemeters, calibration and practical aspects of H p (3) monitoring. A 2015 review. J Radiol Prot 2015;2015(35):R17. https://doi.org/10.1088/0952-4746/35/3/R17.
[18] Carinou E, Ginjaume M, O'Connor U, Kopec R, Merce MS. Status of eye lens radiation dose monitoring in European hospitals. J Radiol Prot 2014;34:729. https://doi.org/10.1088/0952-4746/34/4/729.
[19] IAEA. Implications for occupational radiation protection of the new dose limit for the lens of the. Eye 2014.
[20] Merce MS, Korchi AM, Kobzeva L, Damet J, Erceg G, Gonzalez AM, et al. The value of protective head cap and glasses in neurointerventional radiology. J NeuroInterventional Surg 2015. https://doi.org/10.1136/neurintsurg-2015-011703.
[21] Principi S, Delgado Soler C, Ginjaume M, Beltran Vilagrasa M, Escutia RJJ, et al. Eye lens dose in interventional cardiology. Radiat Prot Dosimetry 2015;165:289–93. https://doi.org/10.1093/rpd/ncv051.
[22] Farah J, Struelens L, Dabin J, Koukorava C, Donadille L, Jacob S, et al. A correlation study of eye lens dose and personal dose equivalent for interventional cardiologists. Radiat Prot Dosimetry 2013;157:561–9. https://doi.org/10.1093/rpd/nct180.
[23] Kicken PJH, Kemerink GJ, van Engelshoven JMA. Dosimetry of occupationally exposed persons in diagnostic and interventional arteriography. Part 1: assessment of entrance doses. Radiat Prot Dosimetry 1999;82:93–103. https://doi.org/10.1093/oxfordjournals.rpd.a032620.
[24] Strocchi S, Chiaravalli A, Veronese I, Novario R. On-field evaluation of operator lens protective devices in interventional radiology. Radiat Prot Dosimetry 2016;171:382–8. https://doi.org/10.1093/rpd/ncv412.
[25] Kubo ALSL, Mauricio CLP. TLD occupational dose distribution study in nuclear medicine. Radiat Meas 2014;71:442–6. https://doi.org/10.1016/j.radmeas.2014.04.021.
[26] Bor D, Olgar T, Onal E, Caglan A, Toklu T. Assessment of radiation doses to cardiologists during interventional examinations. Med Phys 2009;36:3730–6. https://doi.org/10.1118/1.3168971.
[27] Olgar T, Bor D, Berkmen G, Yazar T. Patient and staff doses for some complex x-ray examinations. J Radiol Prot 2009;29:393. https://doi.org/10.1088/0952-4746/29/3/004.
[28] Janssen RJJN, Hadders RH, Henkelman MS, Bos AJJ. Exposure to operating staff during cardiac catheterisation measured by thermoluminescence dosimetry. Radiat Prot Dosimetry 1992;43:175–7. https://doi.org/10.1093/oxfordjournals.rpd.a081359.
[29] Efstathopoulos EP, Katritsis DG, Kottou S, Kalivas N, Tzanalaridou E, Giazitzoglou E, et al. Patient and staff radiation dosimetry during cardiac electrophysiology studies and catheter ablation procedures: a comprehensive analysis. EP Eur 2006;8:443–8. https://doi.org/10.1093/europace/eul041.
[30] Principi S, Ginjaume M, Duch MA, Sánchez RM, Fernández JM, Vano E. Influence of dosemeter position for the assessment of eye lens dose during interventional cardiology. Radiat Prot Dosimetry 2015;164:79–83. https://doi.org/10.1093/rpd/ncu359.
[31] Lie ØØ, Paulsen GU, Wøhni T. Assessment of effective dose and dose to the lens of the eye for the interventional cardiologist. Radiat Prot Dosimetry 2008;132:313–8. https://doi.org/10.1093/rpd/ncn296.
[32] Vano E, Sanchez RM, Fernandez JM. Estimation of staff lens doses during interventional procedures. Comparing cardiology, neuroradiology and interventional radiology. Radiat Prot Dosimetry 2015;165:279–83. https://doi.org/10.1093/rpd/ncv049.
[33] Vano E, Fernandez JM, Resel LE, Moreno J, Sanchez RM. Staff lens doses in interventional urology. A comparison with interventional radiology, cardiology and vascular surgery values. J Radiol Prot 2016;36:37. https://doi.org/10.1088/0952-4746/36/1/37.
[34] International Commission on Radiation Units and Measurements (ICRU) n.d. http://www.icru.org/reports/reports/measurement-of-dose-equivalents-from-external-photon-and-electron-radiations-report-47 (accessed August 25, 2017).
[35] ISO 4037-1:1996 – X and gamma reference radiation for calibrating dosemeters and doserate meters and for determining their response as a function of photon energy – Part 1: Radiation characteristics and production methods n.d. https://www.iso.org/standard/20781.html (accessed October 18, 2018).
[36] Internal procedure IRA/30.06/05.01/10 n.d.
[37] Evaluation of measurement data — Guide to the expression of uncertainty in measurement n.d.
[38] Principi S, Farah J, Ferrari P, Carinou E, Clairand I, Ginjaume M. The influence of operator position, height and body orientation on eye lens dose in interventional radiology and cardiology: Monte Carlo simulations versus realistic clinical measurements. Phys Med 2016;32:1111–7. https://doi.org/10.1016/j.ejmp.2016.08.

010.
[39] Omar A, Marteinsdottir M, Kadesjö N, Fransson A. On the feasibility of utilizing active personal dosimeters worn on the chest to estimate occupational eye lens dose in x-ray angiography. J Radiol Prot 2015;35:271. https://doi.org/10.1088/0952-4746/35/2/271.
[40] Ginjaume M, Bolognese-Milsztajn T, Luszik-Bhadra M, Vanhavere F, Wahl W, Weeks A. Overview of active personal dosemeters for individual monitoring in the European Union. Radiat Prot Dosimetry 2006;125:261–6. https://doi.org/10.1093/rpd/ncl136.
[41] ICRP: ICRP Publication 85 n.d. http://www.icrp.org/publication.asp?id=icrp%20publication%2085 (accessed August 31, 2017).
[42] Vanhavere F, Carinou E, Gualdrini G, Clairand I, Sans Merce M, Ginjaume M, et al. ORAMED: Optimization of Radiation Protection of Medical Staff. n.d.
[43] Jupp T, Kamali-Zonouzi P. Eye lens dosimetry within the cardiac catheterisation laboratory—are ancillary staff being forgotten? Radiat Prot Dosimetry 2018;178:185–92. https://doi.org/10.1093/rpd/ncx088.
[44] Haga Y, Chida K, Kaga Y, Sota M, Meguro T, Zuguchi M. Occupational eye dose in interventional cardiology procedures. Sci Rep 2017;7:569. https://doi.org/10.1038/s41598-017-00556-3.
[45] Alejo L, Koren C, Corredoira E, Sánchez F, Bayón J, Serrada A, et al. Eye lens dose correlations with personal dose equivalent and patient exposure in paediatric interventional cardiology performed with a fluoroscopic biplane system. Phys Med 2017;36:81–90. https://doi.org/10.1016/j.ejmp.2017.03.015.
[46] Medici S, Pitzschke A, Cherbuin N, Boldini M, Sans-Merce M, Damet J. Eye lens radiation exposure of the medical staff performing interventional urology procedures with an over-couch X-ray tube. Phys Medica PM Int J Devoted Appl Phys Med Biol Off J Ital Assoc Biomed Phys AIFB 2017;43:140–7. https://doi.org/10.1016/j.ejmp.2017.11.002.
[47] Magee JS, Martin CJ, Sandblom V, Carter MJ, Almén A, Cederblad Å, et al. Derivation and application of dose reduction factors for protective eyewear worn in interventional radiology and cardiology. J Radiol Prot Off J Soc Radiol Prot 2014;34:811–23. https://doi.org/10.1088/0952-4746/34/4/811.
[48] Zagorska A, Romanova K, Hristova-Popova J, Vassileva J, Katzarov K. Eye lens exposure to medical staff during endoscopic retrograde cholangiopancreatography. Phys Med 2015;31:781–4. https://doi.org/10.1016/j.ejmp.2015.03.011.

Paper II

Characterisation of the impacts of the environmental variables on Timepix3 Si sensor hybrid pixel detector performance

Published in Nuclear Instruments and Methods in Physics Research (November 2020)

M. Nowak, L. Tlustos, P.Carbonez, F.R. Verdun, J. Damet

Nuclear Inst. and Methods in Physics Research, A 981 (2020) 164502

Contents lists available at ScienceDirect

Nuclear Inst. and Methods in Physics Research, A

journal homepage: www.elsevier.com/locate/nima

Characterisation of the impacts of the environmental variables on Timepix3 Si sensor hybrid pixel detector performance

M. Nowak [a,b,*], L. Tlustos [a], P. Carbonez [a,c], F.R. Verdun [b], J. Damet [a,b,c]

[a] CERN, European Organization for Nuclear Research, Geneva, Switzerland
[b] Institute of Radiation Physics, Lausanne University Hospital and University of Lausanne, Lausanne, Switzerland
[c] Department of Radiology, University of Otago, Christchurch, New Zealand

ARTICLE INFO

Keywords:
Timepix3
Hybrid pixel detector
Characterisation

ABSTRACT

The study was conducted to calibrate and characterise the response of the Timepix3 photon-counting hybrid pixel detector. The study was conducted to calibrate and characterise the response of the Timepix3 photon-counting hybrid pixel detector. The goal was also to determine the impact of the angular variation of the detector to the source, of temperature change, and of ambient or strobe light on the on the detector response (measured fluence and energy spectrum). The impacts were studied using X-ray fluorescence lines, as well as Am-241 and Fe-55 radioactive sources. Angular variation measurements indicated angular dependence. This dependency increased with the angle and increased with lower energies. A decrease in fluence of up to 98.4% was recorded for Fe-55 (5.89 keV) and 43.1% for Am-241 (59.56 keV) at an angle of 90°. Temperature measurements showed a 4% decrease of photon count when increasing the temperature from 10 °C to 36 °C. Energy spectra were shifted to lower energies when the temperature increased. Measurements with variable light intensities showed no variations in terms of fluence or energy spectra. However, if it was a strobe light, the fluence was overestimated by 10% and the spectral shape presented an additional artefactual peak around 3 keV. To restrict the variability of the detector response and avoid a time-consuming calculation of the error factor, due to the detector's temperature variation, we showed that it is necessary to keep the measurement temperature as close as possible to the temperature at which the calibration was performed. We also discovered the necessity of focusing on other relevant parameters such as the effect of the ambient light level or the angle of incidence of the X-ray beam impinging the detector on the detector response. This enabled us to propose a set of correction factors that can be used for other applications.

1. Introduction

Interest in hybrid pixel detectors (HPD) has increased in recent years. Indeed, its characteristics make it an adaptable tool and easy-to-use detector that provides access to spatial, temporal, and energetic information of the incident particles. An HPD is designed to connect each one of the pixels in the sensor to a readout pixel providing a dedicated pulse processing circuit. This hybrid detector makes it possible to adapt the material of the sensor to a dedicated application.

Hybrid pixel detectors have been used at CERN since 1998 [1] and were first successfully tested in a three pixel-chip telescope in 1991 [2]. The first use in an experiment at CERN was in the lead beam experiment WA97 [3]. Ever since, pixel detectors have become key components in particle physics experiments. Based on the know-how gained in high energy physics experiments, CERN Medipix collaborations were formed and allowed the creation of HPD and the development of several versions of the Medipix or Timepix chips (versions 1 to 4). These detectors cover a wide range of applications. They are currently used to monitor the radiation environment in the ATLAS and CMS caverns, detect neutrons with different energies or verify and validate simulation [4]. They are also used for medical imaging or dosimetry. Medipix3 is used in the spectral scanner MARS that produced the first coloured images of a human body, providing the first CT images for diagnostic applications with tissue/organ identification [5]. Furthermore, these detectors are also used in mammography imaging [6], dental imaging [7] or as dosimeters in the international space station [8] and in industrial applications (Panalytical, Advacam, ASI).

Many articles mention the possible applications of Timepix3, but no paper has so far been published about its characterisation. This means that various parameters such as light, temperature, or angular variation have not yet been addressed. This lack of information led us to check the importance of the variability of several relevant parameters on the data. The necessity of such measurements is confirmed by Khalil et al. [9], where it is mentioned that a better

* Corresponding author at: Institute of Radiation Physics, Lausanne University Hospital and University of Lausanne, Lausanne, Switzerland.
E-mail address: marie.nowak@chuv.ch (M. Nowak).

https://doi.org/10.1016/j.nima.2020.164502
Received 2 August 2019; Received in revised form 21 July 2020; Accepted 2 August 2020
Available online 4 August 2020
0168-9002/

control of the measurement temperature might have led to more precise measurements.

For this study we used a Timepix3 HPD, developed in the framework of the Medipix3 collaboration [1]. The goal of this study was to analyse the use of this detector to measure scattered X-ray radiations in a hospital environment, where medical staff is present (such as in an operating room) in order to improve their exposure assessment for an energy range of 20–120 keV. In fact, the Timepix3 makes it possible to measure both the fluence and energy spectrum around an X-ray tube in real time and at any position. In order to perform the measurements, we first made an accurate energy calibration of the detector. This step is crucial for the rest of the study, since a change of response with measurement condition can distort the data analysis. Finally, the detector response was recorded for angular, temperature, and light intensity variations.

2. Materials and methods

2.1. Timepix3 detector and software

The Timepix3 [10] is an HPD developed by the Medipix3 [1] collaboration at CERN (see Fig. 1). This chip mounted on an electronic board has a pixel matrix of 256 × 256 square pixels of 55 μm pixel pitch that can process up to 40 Mhits/cm^2/s. The chip is bump-bonded to a 500 μm thick p-on-n silicon sensor by ADVACAM [11]. The sensor is covered by an aluminium protective layer of 500 nm to prevent light induced leakage currents in the sensor. The sensor was biased at 300 V. The aluminium layer reduces the number of ambient photons, and is effective for lights of wavelengths studied here, i.e. natural and artificial light present in the laboratory (590 lux). This allows the leakage current to easily correct the current induced by the constant light. On the other hand the strobe light induces a periodic current change. The current required for leakage current compensation is therefore modified. The base is not stable and the effective noise increase by counting lower energy photons.

Timepix3 detector was operated in data driven mode, which collects after each photon interaction (defined hereafter as "hit") the information on the arrival time, the charge deposit and the coordinates of each individual pixel triggered by incoming particles converted in the sensor layer of the detector. The total amount of charge deposit is calculated based on the time over threshold (ToT) information. For this study, we chose to analysed only information from single pixels, correction factor for pixel sharing was determined directly from measurements, by counting the amount of detected incoming photon with signal on a single pixel and on several pixels. Data were normalised accordingly with the calculated ratio. The detection efficiency of the Si layer was estimated by Monte Carlo simulation. Data were normalised accordingly.

The AdvaDAQ (Advacam, Prague, Czech republic) [11] readout system has been used for this study [12]. The software used to collect the data was Pixet 1.5.0.714 (Advacam, Prague, Czech republic).

2.2. Measurements

2.2.1. Calibration curve

The calibration curve converts the charge deposit information to absorbed photon energy. Each of the 65'536 pixels of the chip works independently from each other, it is crucial to calibrate each pixel separately.

The calibration curve was obtained following the method described by J. Jakubek [13]. We used a gamma source of Am-241 (35.6 MBq) and a source of Fe-55 (0.6 MBq) placed 2 cm from the detector. The Am source in encapsulated in a protective aluminium casing. The alpha component is thus fully absorbed and does not alter the detector response. We used characteristic fluorescence peaks generated with the Philips/PANalytical PW30/x0 x'pert pro device (Malvern Panalytical, Malvern, UK) using different metallic foils: Ag, Cu, Mo, Sn, Ti. Sources and fluorescence peak energies are presented in Table 1.

Fig. 1. Timepix3 detector [1].

Table 1
Correspondence of the energy to the associated source or metallic foil. *correspond to the energy of fluorescence of the metallic foil, when irradiated by an X-Ray source of 40 keV, 10 mA.

	Element	Energy [keV]
Sources	Fe-55	5.89
	Am-241	59.54
Metallic foil*	Cu	8.05
	Ti	4.51
	Mo	17.45
	Sn	25.20
	Zr	15.75
	Ar	22.16

The calibration curve is modelled by the following equation:

$$f(x) = ax + b - \frac{c}{x - t} \tag{1}$$

2.2.2. Energy resolution

The energy resolution R_E was calculated for the energies of each source and for each X-ray fluorescence according to Eq. (2) with the Full Width at Half Maximum (FWHM) and the energy E of the peak centroid.

$$R_E = \frac{FWHM}{E} \tag{2}$$

2.2.3. Angular variation

The angular variation measurements were carried out with the two radioactive sources (Table 1). Each source was placed facing the detector at 10 cm distance and rotated with angular steps of 15° from −90° or −60° (due to the thickness of the readout system for horizontal axis rotation as seen Fig. 2) to +90°, 0° being right in from the chip. An irradiation time of 10 min per position was chosen in order to obtain a significant number of hits per pixel (over 1000). Each measurement was carried out 3 times. The mean value is presented. The chip is mounted on an electronic board, which gives a clear asymmetry. The response of the chip was tested for a left/right angular variation along the vertical axis of the board (Fig. 3A) then for an up/down angular variation along the horizontal axis of the board in the same conditions (Fig. 3B).

2.2.4. Temperature

The temperature measurements were carried out in an environmental test chamber EXCAL 1423 – HA (Climats, St Médard d'Eyrans, France). The humidity was set to be stable at 0% (k = 0.1%). An Am-241 source was used for the measurements and placed facing the detector at 1.55 cm distance. A source meter Keithley 2400 (Tektronix, Beaverton, Oregon, USA) is used for bias current. The irradiation time was set to 10 min for each measurement. The measurements were

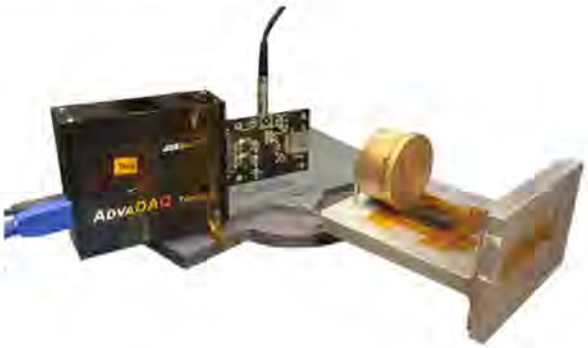

Fig. 2. Setup for the horizontal axis rotation.

carried out from 0 °C to 36 °C, with 2 °C increment. The temperature range was chosen with the Medipix team to protect the electronic and avoid condensation at a low-temperature or melting any components at a high-temperature.

2.2.5. Light variation

For the light measurement, the detector was irradiated using a source of Am-241 placed at a 10 cm distance, under different light intensity conditions. Each measurement was carried out 3 times and for a duration of 10 min; only the mean value is presented. Light variation measurements were performed with both artificial and natural light sources. The artificial source was placed next the Am-241 source and illuminating the detector. The sources of light came from the room lighting, the sunlight entering through windows, and a DP-021 AA-C lamp (De.power, Zhongshan, GD, China) providing different intensities of continuous light as well as a pulsed light mode. The intensity was then measured by placing a lux-metre CL 200 (Konica Minolta, Tokyo, Japan) in the detector position in the same conditions. The lux values are presented in Table 2.

3. Results

3.1. Calibration curve

Fig. 4 represents the mean calibration curve obtained for the 65'536 pixels of the Timepix3. The lower energy represented is 2 keV. The first part of the curve presents a shoulder, and the curve is linear between 8 keV and 60 keV.

Table 2
Summary of all the light sources used, and their corresponding lux intensity. *Mode 3 for the DP-021 AA-C lamp is a strobe mode with 100 ± 1 pulse by minute.

	Light intensity [lx]
Window shutter close; room light off	0.8
Room light + Sunlight entering through windows	587
DP – 021 AA-C Lamp – Mode 1	7000
DP – 021 AA-C Lamp – Mode 2	9000
DP – 021 AA-C Lamp – Mode 3*	0 to 5700

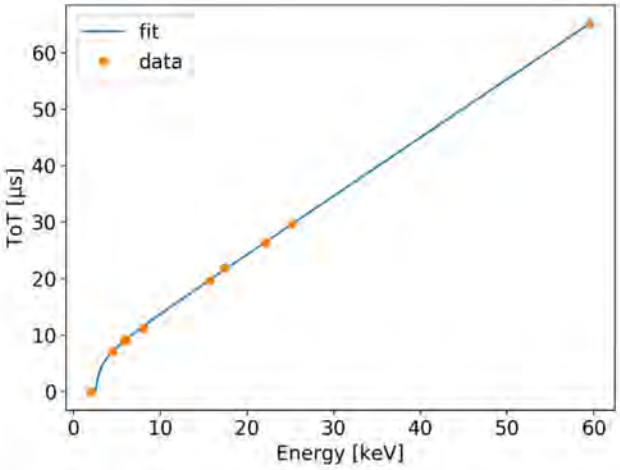

Fig. 4. Calibration curve (R^2 = 0.99991). Orange dots are data obtained by measurements, the blue line was obtained by fitting the equation [13].

3.2. Energy resolution

Fig. 5 shows the energy resolution for different energies. It shows that the energy resolution decreases with energy. Fig. 6 shows the fit and the FWHM of the Am-241 spectra.

3.3. Angular variation

Figs. 7 to 9 A show horizontal axis rotations, while Figs. 7 to 9 B show vertical axis rotations. Fig. 7 shows the photon counts on the chip normalised by the number of counts received for an angle of 0°. Fig. 8 shows the distribution of photon hits on the chip according to the angle.

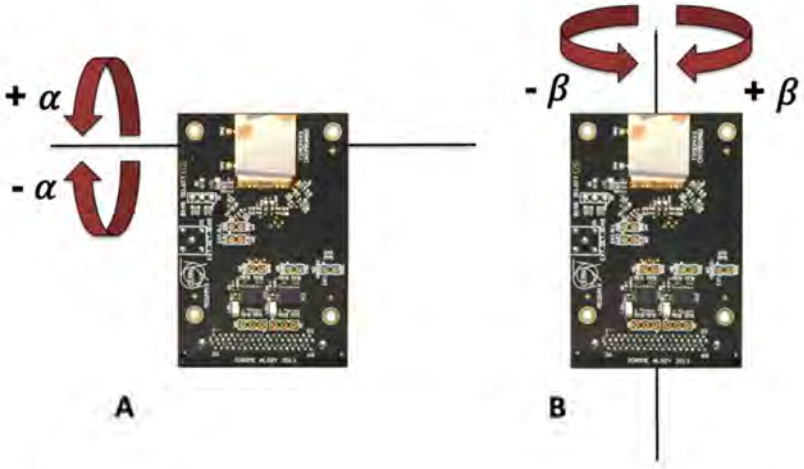

Fig. 3. Angular variation of the detector. A, Horizontal axis rotation. B, Vertical axis rotation.

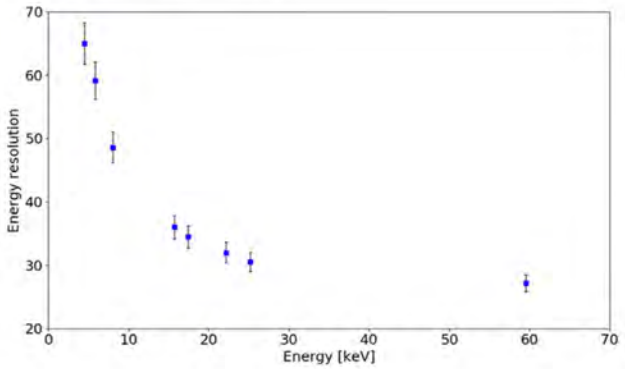

Fig. 5. Energy resolution as a function of the energy. The error bar corresponds on standard incertitude ($\sigma = 1$).

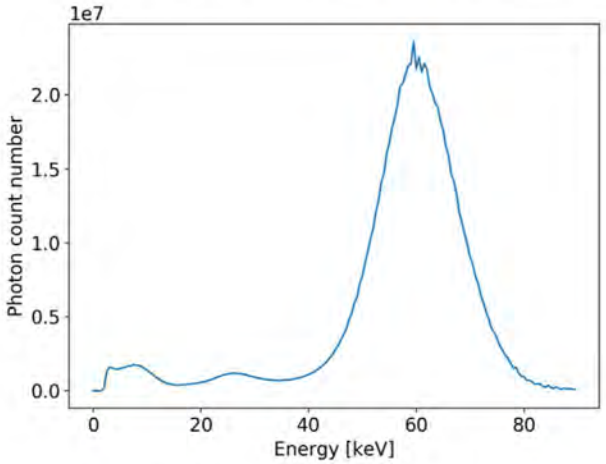

Fig. 6. Energy spectrum of Am 241.

Fig. 7A (horizontal axis rotation) shows values ranging from −60° to +90°. On this graphic, the photon count number for the Am241 is maximum at 0°. From +15° to +60°, only 80% of the photons will reach the detector compared to 0°. This number decreases to 50% for an angle of +90° and remains between 70% and 75% for angles from −15° to −60°. For the Fe-55, the maximum photon count number is for 0°. This number decreases to 46% at −60° and to 1.9% at +90°.

Fig. 7B (vertical axis rotation) for Am 241 shows a relatively constant photon count number from −75° to +75°, with a 6% maximum difference in relative count in this range. The photon count ratio decreases to 56.9% for an angle of +90°. The photon count number

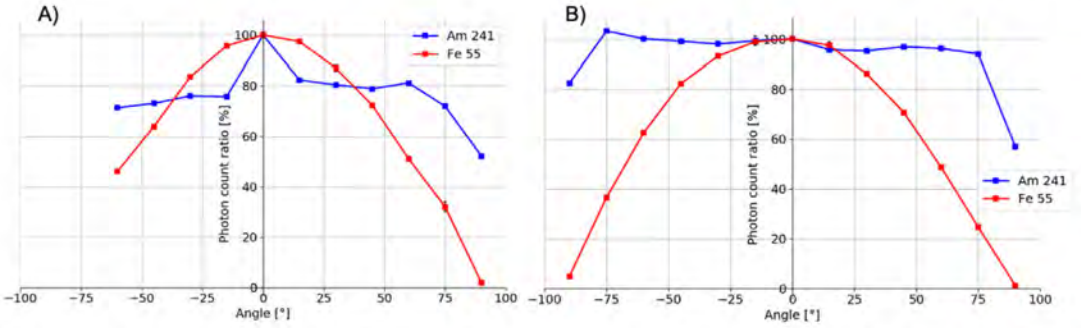

Fig. 7. Fluence as a function of the angle for the (A) horizontal axis rotation, (B) vertical axis. The blue curve represents the angular variation for an Am-241 source. The red curve represents the angular variation for a Fe-55 source. On the three values, only the mean value is presented. Error bars are too small to be visible. (For interpretation of the references to colour in this figure legend, the reader is referred to the web version of this article.)

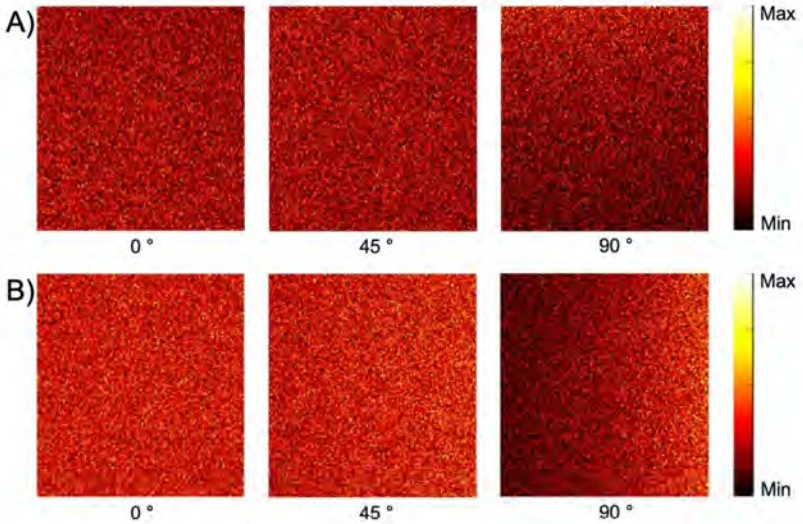

Fig. 8. This graphic shows the photon count number on the chip for angles of 0°, 45°, and 90° with an Am-241 source for (A) horizontal axis rotation, (B) vertical axis rotation. White represents the maximum photon count on a pixel, and black the minimum value.

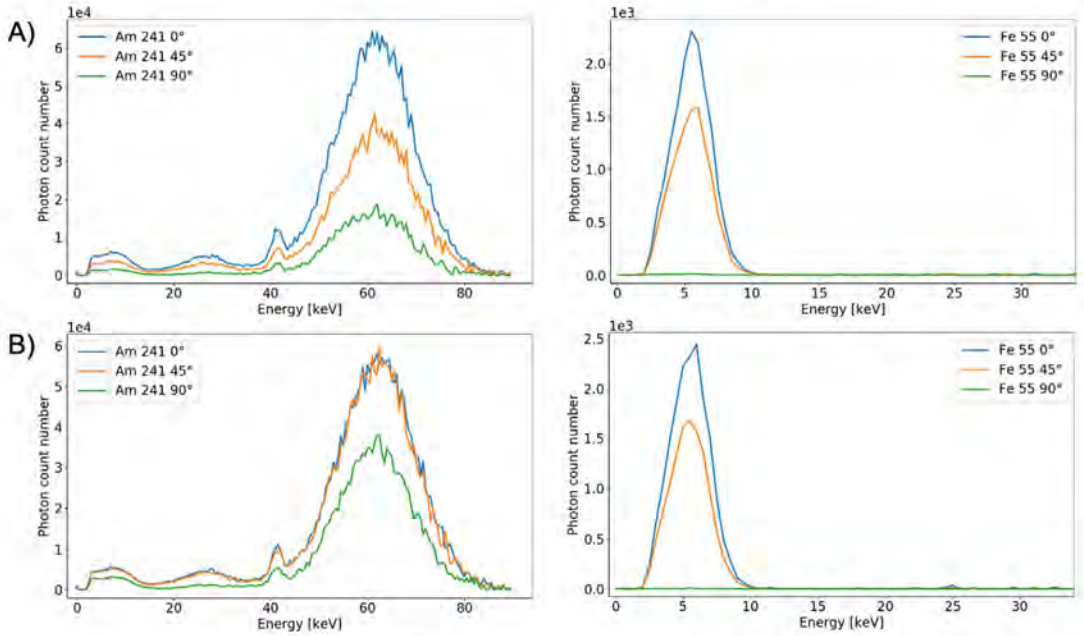

Fig. 9. Energy spectra of an Am-241 source (left) and Fe-55 source (right) for (A) horizontal axis rotation, (B) vertical axis rotation at 0°, 45° and 90°.

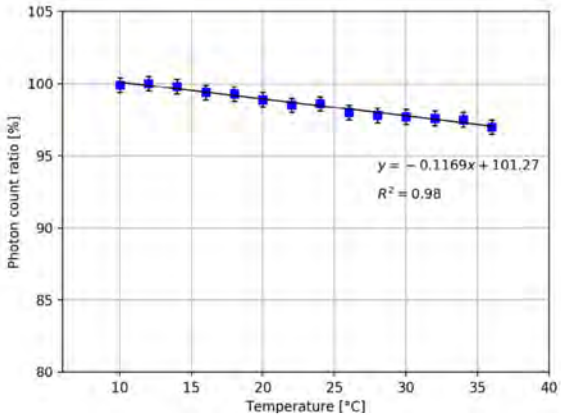

Fig. 10. Photon count ratio as a function of the temperature.

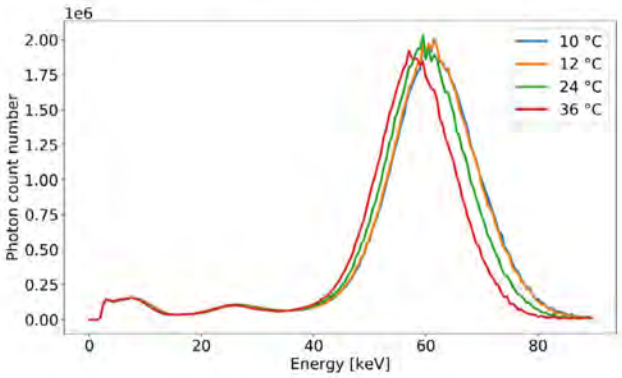

Fig. 11. Energy spectra of Am 241 for different temperatures.

received by the chip with the Fe-55 is maximum for an angle of 0° and decreases to reach only 1.6% at +90°.

3.4. Temperature

Fig. 10 shows the normalised photon count ratio received by the chip as a function of the climatic chamber temperature. The highest photon fluence is measured at 12 °C, and the lowest for 36 °C. A difference of 3% is calculated between 12 °C and 36 °C. The higher the temperature in the climatic chamber, the lower the number of photons captured by the chip. Fig. 11 shows a shift for the Am-241 peak to a lower energy when the temperature increases. Furthermore, the amplitude of the peak decreases with the temperature, this can be related to the missing photon count number seen on Fig. 10.

3.5. Light variation

Fig. 12 shows the photon count number variation as a function of the light intensity. The 4 first bars in the graph represent light intensity from 0.8 to 9000 lx, the last column represents a pulsed light with an intensity range from 0 to 5700 lx. A maximum photon count number difference of 0.6% was observed between the different continuous light measurements. While a 10.5% difference was observed between the photon count number obtained with various continuous light and pulsed light. Bias current increase with light intensity.

4. Discussion

The detector used in this experiment can measure photons with an energy as low as 2 keV. We have demonstrated that the correlation between the ToT and the energy is linear from 8 keV to 60 keV. The shape of the calibration curve is similar to the one obtained by J. Jakubek [13] with an anterior version of the HPD used in this study: the Timepix detector. Burian et al. [14], showed a calibration curve of a silicon Timepix3 detector, similar to the one obtained in this study. Calibration curves are intrinsic to each detector.

It is worth mentioning that Dach et al. [15] in their study presented a calibration curve for Si and GaAs similar to ours. They also showed that between a Si and GaAS detector, a slight shift in energy between the two detectors could be observed. They mention in particular that

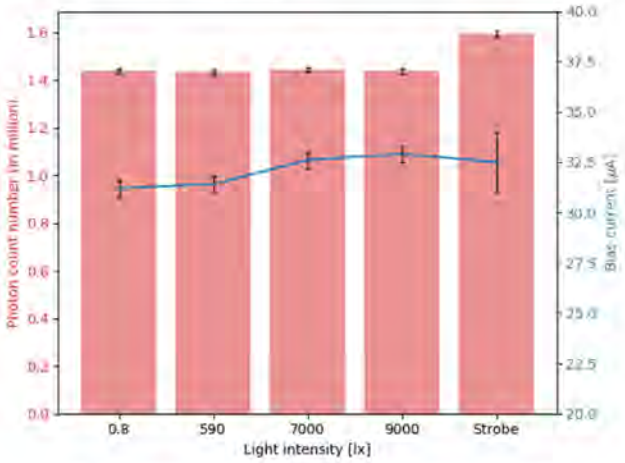

Fig. 12. Photon count number as a function of the light intensity.

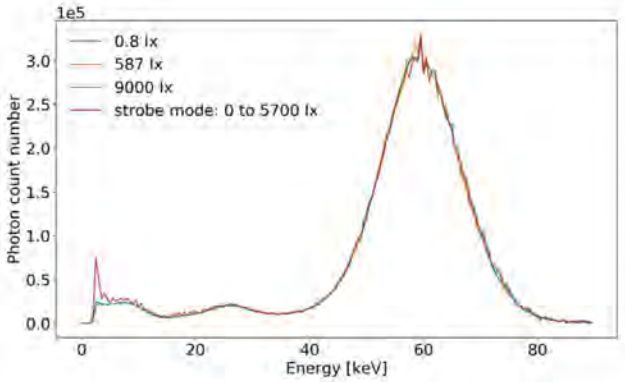

Fig. 13. Energy spectra of Am 241 for different light intensities.

GaAs is less radiation transparent than silicon and thus captures more photons of 12 keV or more. Also, the angular measurement in this study showed a good correlation between Si and GaAs. The shape of the spectra is similar between both detectors, but the amplitude of the spectrum is higher for GaAS. Conversely, in his thesis, E. Fröjdh [16] showed that silicon captures more photons at 24 keV than CZT or CdTE.

This study shows that the Timepix3 detector can be used at very low energy. In fact, the shape of the calibration curve reveals an energy range starting at 2 keV. This makes it a useful device for dosimetry. For comparison, in a medical environment using X-ray radiography, the energy range of the actual detector begins around 20 keV [12,17]. It is important to emphasise that the conclusions of this study is related to a detector with an Si sensor for a thickness of 500 μm. The response of the detectors to the environmental parameter bonded on a CdTe sensor or on different thickness sensor would present different characteristics.

The figure of angular variation (Fig. 7), shows that for energies of 60 keV, a decrease in fluence up to 52% can be recorded for an horizontal axis rotation. While a vertical axis rotation (from −75° to + 75°) will only result in a miss of information of maximum 6%. Fig. 6 shows that the decrease in fluence for Fe 55 is close to the expected cosine function. However, a difference is observable and is due to the angular variation. It is therefore important during measurements to place the detector facing the radiation source as much as possible in order to limit correction factors. Fig. 8 shows that it is possible from the fluence distribution on the detector to estimate the angle of the detector towards the source and therefore apply a correction factor. Fig. 9 compares the energy spectra for different angles and sources, no differences are noticed for the spectral pattern (between 0°, 45° and 90° angles), only the fluence is different. Angular variation impacts the fluence but not the shape of the energy spectra.

Measurements made with the Fe-55 source show a decrease of the number of photons as a function of the angle. The curve presented has a cosinusoidal shape. The low energy of the Fe-55 source, allows a detection efficiency of 100%, the cosine decrease of the photon number is explained by the steradian angle of the detector with the source [18]. In addition, the detection efficiency for the americium source is much lower (<5%). The decrease of photons linked to the angle of the detector with the source is in opposition to a longer path of photons in the Si sensor and therefore an increase in the probability of detection.

The measurements of temperature variations (Fig. 10) show a progressive decline in count ratio when temperatures increase with a 3% loss between 12 and 36 °C. In fact, the current loss is increasing with the temperature, so much so that the current caused a loss in the bias current in the 100 kΩ resistor (in series with the sensor). Another explanation would be that the high voltage generator could not provide enough power and so reduced the voltage. This led to a longer collection time, thus increasing the cluster number for 2, 3, 4, ... pixels and thus reducing the number of single pixels. Only single pixel data are analysed and a correction for sharing pixel is applied later, so the difference in measurement could also be explained by this explanation. It is therefore important to measure at constant temperatures or to apply a corrective factor.

On Fig. 11, a shift in energy can be observed for different temperatures which is similar to observations made by D. Turecek et al. We often do the characterisation of the chip under laboratory conditions, however it is important to note that fluctuations in the temperature of the measurement room may cause the observed shifts in the energy spectra. The sensitivity of the detector for the temperature change implies that it is not correct to use only one calibration curve for different temperatures. It is necessary to create a dedicated calibration for each condition. Despite being time consuming these sets of behaviour characterisation are a prerequisite for obtaining reliable data. However, it is possible to calculate correction factors following the method of D. Turecek et al. [19] method.

Fig. 12 shows that for a continuous light the photon count number detected by the chip is stable. The chip can be exposed to different light intensities without decrease in fluence. However, the data will be affected if a light near the source strobes (e.g. defective strobe light). It is important during measurements to take this into account and to avoid any pulsating lights. Fig. 13 shows the energy spectra for different light intensities. The spectra are similar for the different light intensities, but there is a noticeable difference for the pulsed light compared to the spectrum of continuous light. The aluminium layer filters background noise from stray light at constant light intensity, but loses its effectiveness in strobe mode, due to more delicate leakage current compensation. The stray light generates a constant background noise and can be easily controlled by adjusting the threshold. In the case of strobe light, the background noise fluctuates constantly, each flash ramps up sharply the background noise on a very short period of time which is converted into a very low energy photon. As a result, the measured fluence will be greater, and the spectrum appears noisy.

5. Conclusion

We characterised the response of the chip for various parameters. Results indicate that the Timepix chip offers interesting spectrometric features in the 2–60 keV energy range, demonstrating great potential for applications in the medical sector. Results show that it is important to keep a temperature measurement as close as possible to the calibration temperature in order to avoid correction factors that are time-consuming/difficult to calculate since they have to be determined from different calibration curves. For light and angular variation, it is also better to keep the detector as much as possible facing the

radiation source or the main field lines, and it is better to use a constant light level during the whole measurement period. Although for these parameters, correction factors can be easily deducted from this article. Should measurements be performed over a long period facing a variety of environment conditions, correction factors must be applied to the raw data. The Timepix3 chip can be used in a restricted angular range at low energies.

CRediT authorship contribution statement

M. Nowak: Collected the data, Performed the analysis, Wrote the paper. **L. Tlustos:** Contributed data or analysis tools, Performed the analysis. **P. Carbonez:** Conceived and designed the analysis, Wrote the paper. **F.R. Verdun:** Conceived and designed the analysis, Performed the analysis, Wrote the paper. **J. Damet:** Conceived and designed the analysis, Performed the analysis, Wrote the paper.

Declaration of competing interest

The authors declare that they have no known competing financial interests or personal relationships that could have appeared to influence the work reported in this paper.

Acknowledgements

The authors would like to thank Dr. M. Campbell, head of the Medipix group and the helpful advice on various technical issues given by J. Alozy from the Medipix group at CERN.

References

[1] Medipix3 Collaboration | Medipix n.d. https://medipix.web.cern.ch/collaboration/medipix3-collaboration. (Accessed 8 January 2019).
[2] F. Anghinolfi, P. Aspell, K. Bass, W. Beusch, L. Bosisio, C. Boutonnet, et al., A 1006 element hybrid silicon pixel detector with strobed binary output, IEEE Trans. Nucl. Sci. 39 (1992) 654–661, http://dx.doi.org/10.1109/23.159682.
[3] G. Alexeev, E. Andersen, A. Andrighetto, F. Antinori, N. Armenise, J. Ban, et al., First results from the 1994 lead beam run of WA97, Nuclear Phys. A 590 (1995) 139–146, http://dx.doi.org/10.1016/0375-9474(95)00232-P.
[4] P. Lujan, Technology used for 3D colour X-ray helps to monitor radiation at CMS | CMS Experiment n.d. https://cms.cern/news/technology-used-3d-colour-x-ray-helps-monitor-radiation-cms. (Accessed 17 January 2019).
[5] M.F. Walsh, A.M.T. Opie, J.P. Ronaldson, R.M.N. Doesburg, S.J. Nik, J.L. Mohr, et al., First CT using Medipix3 and the MARS-CT-3 spectral scanner, J. Instrum. 6 (2011) C01095, http://dx.doi.org/10.1088/1748-0221/6/01/C01095.
[6] L. Loaiza, G.A. Roque, C.A. Avila, L.M. Mendoza, R.J. Rueda, J.M. Racedo, Feasibility study of a TIMEPIX detector for mammography applications, in: J. Brieva, J.D. García, N. Lepore, E. Romero (Eds.), 13th Int. Conf. Med. Inf. Process. Anal., SPIE, San Andres Island, Colombia, 2017, p. 30, http://dx.doi.org/10.1117/12.2285910.
[7] J. Watt, D.W. Davidson, C. Johnston, C. Smith, L. Tlustos, B. Mikulec, et al., Dose reductions in dental X-ray imaging using Medipix, Nucl. Instrum. Methods Phys. Res. A 513 (2003) 65–69, http://dx.doi.org/10.1016/j.nima.2003.08.003.
[8] N. Stoffle, L. Pinsky, M. Kroupa, S. Hoang, J. Idarraga, C. Amberboy, et al., Timepix-based radiation environment monitor measurements aboard the international space station, Nucl. Instrum. Methods Phys. Res. A 782 (2015) 143–148, http://dx.doi.org/10.1016/j.nima.2015.02.016.
[9] M. Khalil, D. Turecek, J. Jakubek, J. Kehres, E.S. Dreier, U.L. Olsen, Intrinsic XRF corrections in Timepix3 CdTe spectral detectors, J. Instrum. 14 (2019) C01018, http://dx.doi.org/10.1088/1748-0221/14/01/C01018.
[10] X. Llopart, R. Ballabriga, M. Campbell, L. Tlustos, Wong W., Timepix, a 65k programmable pixel readout chip for arrival time, energy and/or photon counting measurements, Nucl. Instrum. Methods Phys. Res. A 581 (2007) 485–494, http://dx.doi.org/10.1016/j.nima.2007.08.079.
[11] ADVACAM ADVACAM - Imaging the unseen n.d. http://advacam.com/. (Accessed 2 August 2018).
[12] D. Turecek, J. Jakubek, P. Soukup, USB 3.0 readout and time-walk correction method for Timepix3 detector, J. Instrum. 11 (2016) C12065, http://dx.doi.org/10.1088/1748-0221/11/12/C12065.
[13] J. Jakubek, Precise energy calibration of pixel detector working in time-over-threshold mode, Nucl. Instrum. Methods Phys. Res. A 633 (2011) S262–S266, http://dx.doi.org/10.1016/j.nima.2010.06.183.
[14] P. Burian, P. Broulím, M. Jára, V. Georgiev, B. Bergmann, Katherine: Ethernet embedded readout interface for Timepix3, J. Instrum. 12 (2017) C11001, http://dx.doi.org/10.1088/1748-0221/12/11/C11001.
[15] F. Dachs, J. Alozy, N. Belyaev, B.L. Bergmann, M.van. Beuzekom, T.R.V. Billoud, et al., Transition radiation measurements with a Si and a GaAs pixel sensor on a Timepix3 chip, Nucl. Instrum. Methods Phys. Res. A (2019) http://dx.doi.org/10.1016/j.nima.2019.03.092.
[16] E. Fröjdh, Hybrid Pixel Detectors : Characterization and Optimization, 2015.
[17] Dosilab : Active dosimetry n.d. https://www.dosilab.ch/ch-fr/active-dosimetry. (Accessed 1 April 2019).
[18] J.D. Sullivan, Geometric factor and directional response of single and multi-element particle telescopes, Nucl. Instrum. Methods 95 (1971) 5–11, http://dx.doi.org/10.1016/0029-554X(71)90033-4.
[19] D. Turecek, J. Jakubek, Dependence on temperature and pixel threshold of the calibration for the Timepix detector and its correction method, J. Instrum. 8 (2013) C01010, http://dx.doi.org/10.1088/1748-0221/8/01/C01010.

Paper III

Characterisation and mapping of scattered radiation fields in interventional radiology theatres

Published in Scientific Reports (October 2020)

M. Nowak, P.Carbonez, M. Krauss, F.R. Verdun, J. Damet

scientific reports

Check for updates

OPEN

Characterisation and mapping of scattered radiation fields in interventional radiology theatres

M. Nowak[1,2]✉, P. Carbonez[1,3], M. Krauss[3,4], F. R. Verdun[2] & J. Damet[1,2,3]

We used the Timepix3 hybrid pixel detector technology in order to determine the exposure of medical personnel to ionizing radiation in an interventional radiology room. We measured the energy spectra of the scattered radiation generated by the patient during X-ray image-guided interventional procedures. We performed measurements at different positions and heights within the theatre. We first observed a difference in fluence for each staff member. As expected, we found that the person closest to the X-ray tube is the most exposed while the least exposed staff member is positioned at the patient's feet. Additionally, we observed a shift in energy from head to toe for practitioners, clearly indicating a non-homogenous energy exposure. The photon counting Timepix3 detector provides a new tool for radiation field characterisation that is easier-to-use and more compact than conventional X-ray spectrometers. The spectral information is particularly valuable for optimising the use of radiation protection gear and improving dosimetry surveillance programs. We also found the device very useful for training purposes to provide awareness and understanding about radiation protection principles among interventional radiology staff.

Proper evaluation of worker exposure is a major issue and current challenge in radiation protection. The effectiveness of worker protection greatly depends on an understanding of the radiation field to which the staff is exposed. A radiation field can be described by fundamental physical quantities: the particle fluence and the energy spectrum. Besides physics, evaluating worker exposure is based on current knowledge of the biological effects of ionizing radiation. The concept of equivalent dose for any given organ and effective dose was introduced for risk management purposes as well as to establish annual dose limits[1]. The effective dose cannot be measured. The calculation of the effective dose integrates factors related to biological effects observed in radiobiological and epidemiological studies[2].

The continuous improvement in understanding the underlying mechanisms of the health effects due to exposure to ionizing radiation motivates a regular re-evaluation of the annual limits.

In 2011, the International Commission on Radiological Radioprotection (ICRP) further restricted the annual eye lens dose limit, resulting in changes to the legal limits in Europe and Switzerland[2]. Before 2011, the annual dose limit for the eye lens was 150 mSv, this limit was set in order to prevent possible cataracts at the end of a career. It was agreed by consensus that if the annual effective dose limit was respected for the whole body it would also imply compliance to the eye lens dose limit[3]. The eye lens dose limit being relatively high, the probability of exceeding it was then quite low. Following a re-evaluation of the effects on the Hiroshima and Nagasaki cohort[4], the limit was then lowered from 150 to 20 mSv[5]. The division of the limit by a factor of 7 significantly changes the stakes, as a large number of staff members may be over this limit. Because of the introduction of this more restrictive limit, a new dedicated operational quantity ($H_p(3)$) was then proposed for managing eye lens exposure[6]. This prompted strong debate on the methods and means of measurements as well as calibration procedures for the measuring instruments.

The 2017 ICRP report also points out the need to revise the operational quantities for external exposure[7]. The ICRU sphere is not used anymore; direct conversion coefficients are instead given to the operational quantities from the fluence using anthropomorphic reference computational phantoms. In line with this new approach, we decided to characterise the radiation field in an interventional radiology (IR) theatre.

Our second reason for wanting to characterise the radiation field is related to the evolution of imaging systems. Medical imaging experts are permanently optimising the dose received by patients[8], as well as using

[1]CERN, European Organization for Nuclear Research, Geneva, Switzerland. [2]Institut of Radiation Physics, Lausanne University Hospital and University of Lausanne, Lausanne, Switzerland. [3]Department of Radiology, University of Otago, Christchurch, New Zealand. [4]Department of Interventional Radiology, Christchurch Hospital, Christchurch, New Zealand. ✉email: marie.nowak@cern.ch

increasingly sophisticated imaging systems and improved image reconstruction algorithms. Additional filters are used to optimise the procedures (patient morphology, paediatric, etc.). These changes influence the energy spectrum used to image the patient's body and thus the energy spectrum of the scattered radiation to which the medical staff is exposed. These changes are often accompanied by a decrease of the dose received by the hospital staff per procedure. Recent studies show that the development of more complex and longer procedures combined with the higher number of patients inevitably leads to an increase in exposure of hospital staff members[9]. Most procedures require staff to remain close to the patient during the image-guided procedures. A study by Sanchez et al.[10] carried out on radiologists shows that more than 50% of them receive a dose higher than the authorized annual limit of 20 mSv, sometimes going up to monthly doses higher than 20 mSv on apron. This means it is important to establish an accurate dosimetry surveillance program in order to avoid underestimating worker dose. Knowledge of the spectrum to which the medical staff is exposed would enable a more accurate calculation of the dose, but would also make it possible to retrospectively know the dose received by an organ and this despite the evolution over time of the operational quantities for external exposure.

The spectral composition of X-ray radiation has been studied for a long time. Although many studies have been carried out based on computer simulations of the spectrum, very few are based on direct measurements. The first studies of the spectral composition of beams from an X-Ray tube date back to the mid-30's[11,12]. The X-ray spectral information was first investigated by measuring attenuation curves. Forty years later, the first computer simulations on primary radiation were performed[13–15]. The first direct measurements of the spectrum were in 1969 by Peaple and Burt[16], later followed by Seelentag and Panzer[17] and Birch and Marshall[18] using crystal scintillator detectors (NaI) or a semiconductor detector (Ge). The measurement set-up leads to cumbersome experimental conditions and involved strong constraints such as concomitant cooling or reducing the counting rate with a distance of several meters to the source and high collimation. In 1983, Castro et al.[19] attempted to solve those problems, using a CdTe detector with a low detection efficiency. However, this kind of measurement requires long-term work along with a large number of corrections and is not suitable for rapid cumulative dose measurements for a procedure or a configuration. More recently, Miyajima et al.[20] used a CdZnTe detector for spectra measurement, with results compatible with those obtained by Monte-Carlo (MC) simulations. The detector has several problems such as poor charge transport properties and requires complex calculated corrections for the spectral distortion.

Adapting a detector to a routine dosimetry application would imply that the device could be used regardless of the radiation field, the collimation, or the position in the radiation field. A very challenging point is the acquisition speed of the data. Missing data can lead to a wrong estimation of the photon fluence and dose. Another challenge to negotiate is making the detector small enough to be comfortable for the user to wear.

With the introduction of new technologies, the measurement of the energy spectrum in hospital theatres can provide optimised radiation protection safety for workers. Since 1997, the CERN Medipix team has been developing novel photon detectors that are able to provide spatial, temporal, and energy information for each incoming photon. This means that these detectors are able to measure the energy spectrum in real time. In this work, we used the Timepix3 detector to measure the energy spectrum of the scattered radiation field in an IR theatre. Compared to other spectral detector[16–20], this detector has the advantage of coping with higher photon fluences and not requiring beam collimation with heavy pinhole shielding. It can be used at any distance from the radiation source in the scattered field and data are available instantaneously. This enabled us to compare the different spectra for different positions in the room, and for different heights. We then created a map of the scattered radiation field extracted directly from the energy spectra as received by a staff member around the X-ray tube.

Materials and methods

Timepix3 detector and software. The Timepix3 chip is a hybrid pixel detector (HPD) developed in the framework of the Medipix3 collaboration at CERN[21], and is a latest version of the Timepix family[22]. We used the Timepix3 chip with a 500 µm thick silicon sensor produced and bump bonded by ADVACAM (Prague, Czech Republic)[23]. We choose a Si sensor layer despite a low absorption efficiency (4% detection at 60 keV versus 87% for a 500 µm CdTe sensor)[24] as this is counterbalanced by a more stable Si response since the production of fluorescence photons is much higher in CdTe, from 80 to 90% versus less than 5% for Si. With a mean free path of fluorescence photons of 10 µm with Si and 110 µm with CdTe. The chip has a pixel matrix of 256×256 square pixels with 55 µm side and can process up to 40 Mhits/cm^2/s. Each pixel sensor is linked to his own readout. A 500 nm aluminium layer covers the sensor. The sensor was biased at 300 V. The data driven mode was selected to collect information on arrival time, charge deposit, and the coordinates of each pixel hit by a photon. The charge deposit was calculated based on the time over threshold value. Each pixel was calibrated independently using radioactive sources and fluorescence peaks of different material foils[25]. We choose to analyze data with signal collected with single pixels only. The choice was made to eliminate additional uncertainties on energy calculation for photons generating a signal on several pixels (pixel sharing correction). Single pixels data do indeed represent only a fraction of all detected photons. The data have thus been normalized taking into account the ratio between the number of photons with single pixel and multiple pixel signals. The overall correction includes the detector efficiency as well as for angular variation, temperature, and light variation, since calibration condition can be different than measurement conditions[26]. Uncertainties have been calculated for energy calibration, pixel sharing, detector efficiency, position, angular variation, temperature, and light variation.

In this study, the Timepix3 chip was connected to the AdvadDAQ (Advacam, Prague, Czech Republic) readout system and data was collected using the Pixet software, version 1.5.0.714 (Advacam, Prague, Czech Republic).

Measurement in interventional radiology theatre. All measurements were carried out in an IR theatre at Christchurch Hospital—New Zealand, using an X-ray imaging system ALLURA XPER FD 20 (Philips,

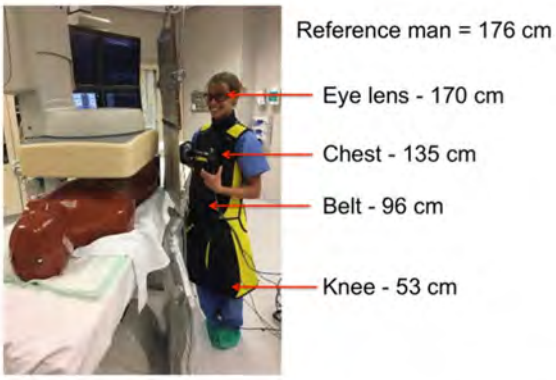

Figure 1. Measurements taken at four different heights in the IR theatre.

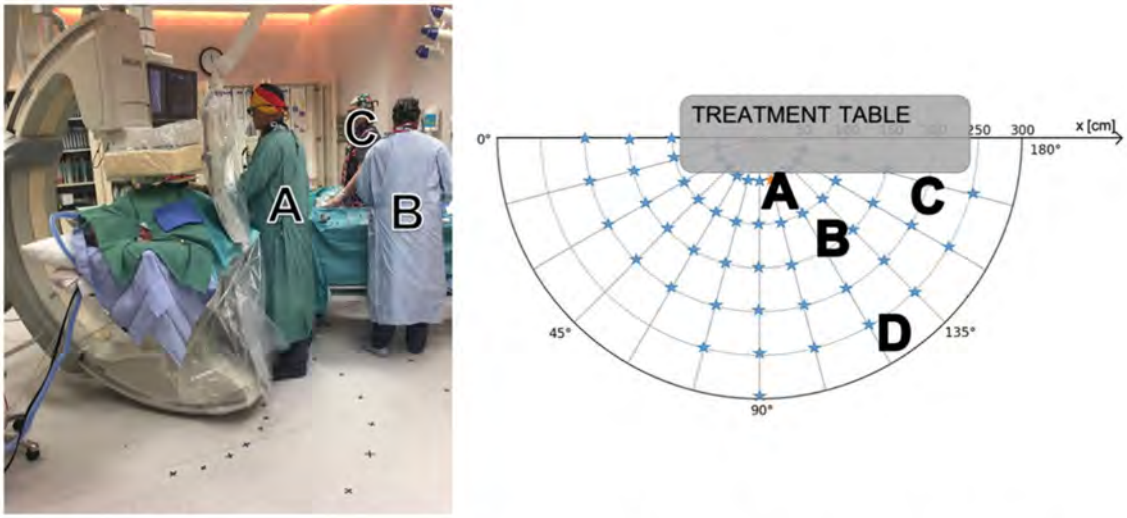

Figure 2. Left: positions of the different staff members in the IR room during procedure. Right: diagram of the different measurement positions (represented by red or blue stars) to create the scattered radiation map of the IR theatre.

Hamburg, Germany). An anthropomorphic male phantom (RSD, Long Beach, CA, USA) was used to simulate a patient lying on the radiotransparent carbon fiber table. Energy spectra of the scattered radiation field were acquired around the table with the Timepix3 detector. Measurements were taken in a 3 m radius half-sphere centered on the abdomen of the phantom and at four different heights corresponding to the eye lens, chest, belt and knee, respectively 170 cm, 135 cm, 96 cm and 53 cm of a 1.76 m medical staff member (Fig. 1). The chosen protocol was the default set-up for pelvis/iliac examinations with an image acquisition rate of 3 frames per seconds (fps), a tube voltage of 74 kVp with a current of 12.0 mA, using the mode of standard dose for a reference patient (70 kg), leading to a filtration of 0.4 mm Cu + 1 mm Al. The cumulative time of measurements depended on the position in the room and ranged from 1 min for the closest positions to 4 min for the furthest away. Each data acquisition point was repeated 3 times; in this article we will present only the mean value of the three measurements for each position. All data have been normalized on 4 min measurement.

A first series of measurements consisted in measuring the radiation field at the standard positions where the staff members stand during a routine procedure. After a period of observation and discussion with the team in place, we identified the four most common positions (see Fig. 2). Collective protection gear (suspended lead screen and lead table drape) were systematically used. We held the Timepix3 chip by hand above the lead apron, and we performed the measurements at the four heights successively in the four positions where the staff stand during the procedures, identified as A, B, C and D in the theatre on Fig. 2.

A second series of measurements consisted in measuring the energy spectra around the patient couch. Acquisitions were taken every 15°, on 180°, around the anthropomorphic phantom, every 50 cm (Fig. 2, right), for the four heights mentioned previously. The cumulative time of measurements depended on the position in the room and ranged from 1 min for the closest positions to 4 min for the furthest away. All data have been normalized on 4 min measurement. The Timepix3 chip was set on a metallic stand infusion holder. No specific means of protection were used. Moreover, the effect of the radiation protection gear (lead screen and lead table drape) was tested at a few positions in the room. On Fig. 2 right, each intersection between an arc and a line represents a position of measurement. The configuration of the room (walls, furniture) did not allow us to do all positions.

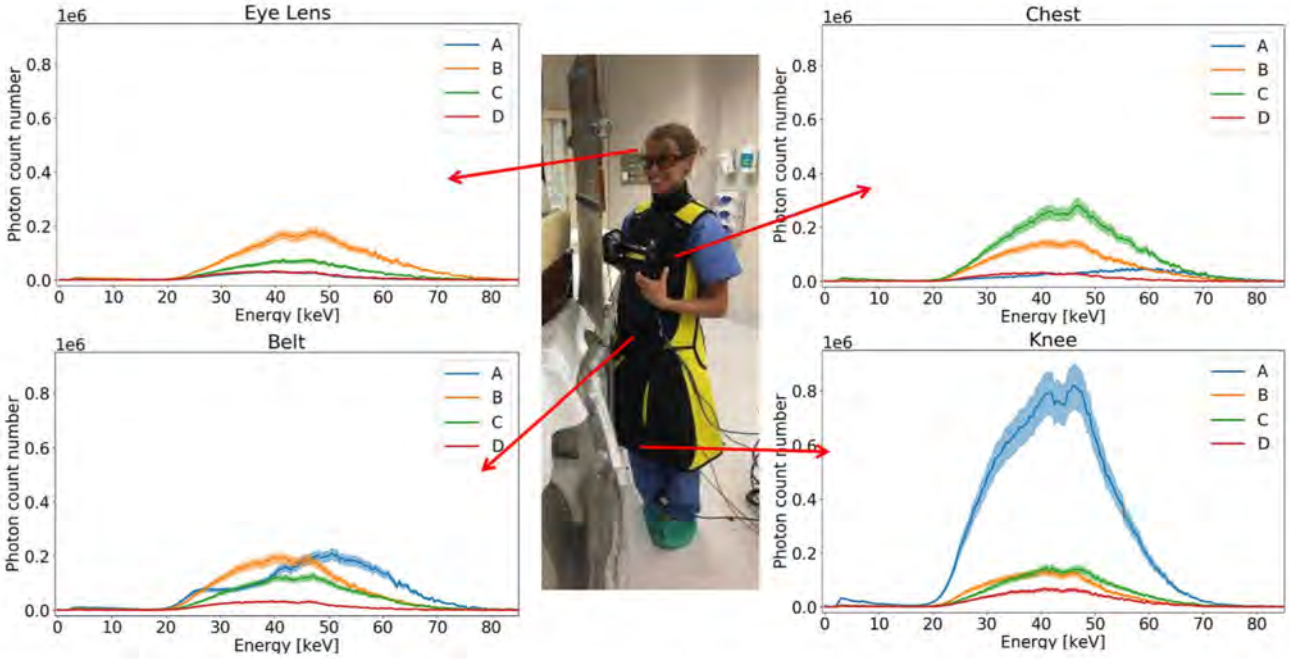

Figure 3. Energy spectra for each medical staff at a given height, with collective protections. Light curves represent the uncertainty.

Measurement points are represented by stars (blue or red). All measurements were performed after the surgery planned for the day. No measurement was done with a patient present in the theatre. These measurements were used to create a map of the theatre. Data has been corrected for pixel sharing and detection efficiency. Each spectrum obtained was segmented into energy bins, each multiplied with an energy-specific weighting factor. The values represented on the map are interpolated with a linear function between the measurement points.

Ethical approval. We confirm that all the methods in this study have been applied in accordance with national guidelines and regulations. The consent of each participant was obtained prior to measurements. Each participant was informed and aware of the risks associated with ionizing radiation. Experimental protocols were approved by CERN Radiation Protection group.

A written consent to publish was obtained by all human participants involved in the study.

Results

Figures 3 and 4 show the energy spectrum measured on a person holding the Timepix3 chip at four heights in the four standard positions of the medical staff. Both figures present the same dataset, in a different way. Figure 3 presents the spectrum measured for a given height for each staff member. On Fig. 3 scales have been adapted to make the comparison easier. Figure 4 shows the energy spectrum measured at four heights for a given staff member. Scales are position dependent.

Figure 5 shows the different energy spectra obtained with and without protective gear. Figure 6 shows the ionizing radiation levels at the 4 different heights in the IR theatre. Figure 7 represents the fluence as a function of the height, 50 cm away from the X-ray tube for an angle of 105° without protection gear. The energy spectrum is given for each of the four heights, i.e. eye lens, chest, belt, and knee.

Discussion

The available data on direct measurements of the scattered radiation field in IR is sparse. An overview of the literature indicates that almost all the studies are done with Monte Carlo simulations[13–15]. Our measurements provide information on the radiation fluence in the theatre as well as the energy spectrum of the scattered photon field. Those two combined pieces of information are helping to understand the exposure level of the medical staff and to evaluate the homogeneity of the field to which the different people are exposed. This approach is part of the needs of the ICRP and ICRU for fluence-based dosimetry[7]. The spectra presented here clearly show that we should need consideration of energy dependence of dosimeter to evaluate doses (Figs. 3 and 4). Since the X-ray spectrum changes depending on the measurement positions (Figs. 3 and 4), it is important to pay attention to the estimation procedure when attempting to estimate the exposure dose at other locations using the value of the exposure dose measured at a given position. Studying the position of the dosimeter is crucial to avoid underestimation of the dose measurement.

The energy threshold for the Timepix3 is 3 keV due to the calibration curve. Marshall et al.[27] measured the energy spectrum with a germanium detector with a higher detection threshold set at 20 keV, and Kalyvas et al. obtained a higher threshold set at 10 keV with an Amptek XR-10 CdTe[28].

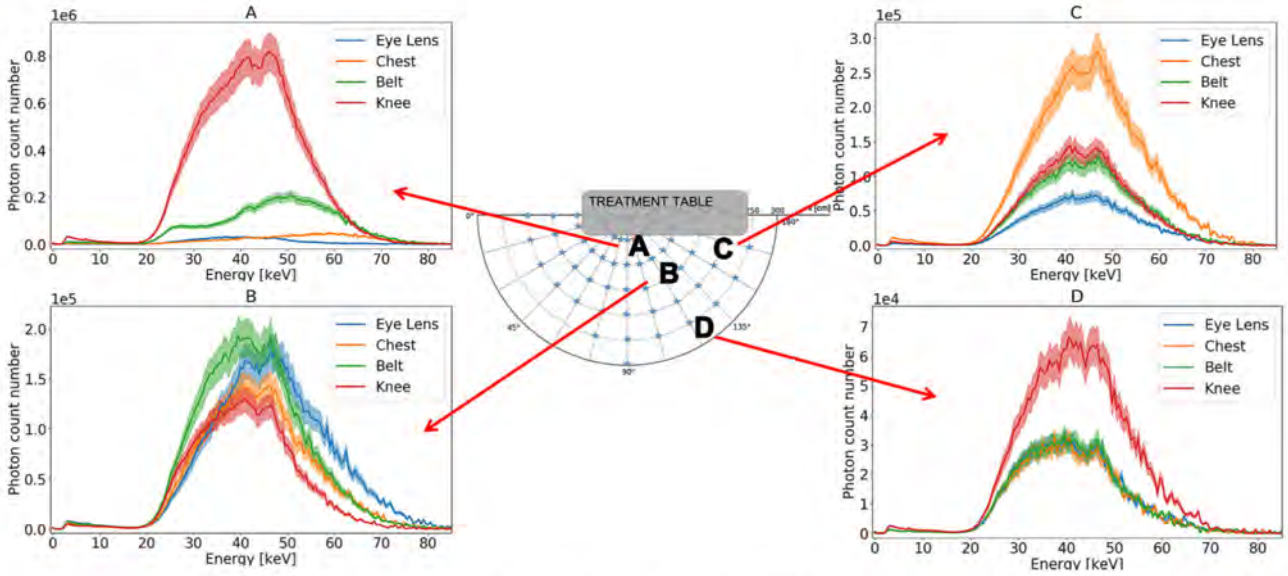

Figure 4. Energy spectra in absolute values for each height for a given person, with collective protections. Light curves represent the uncertainty.

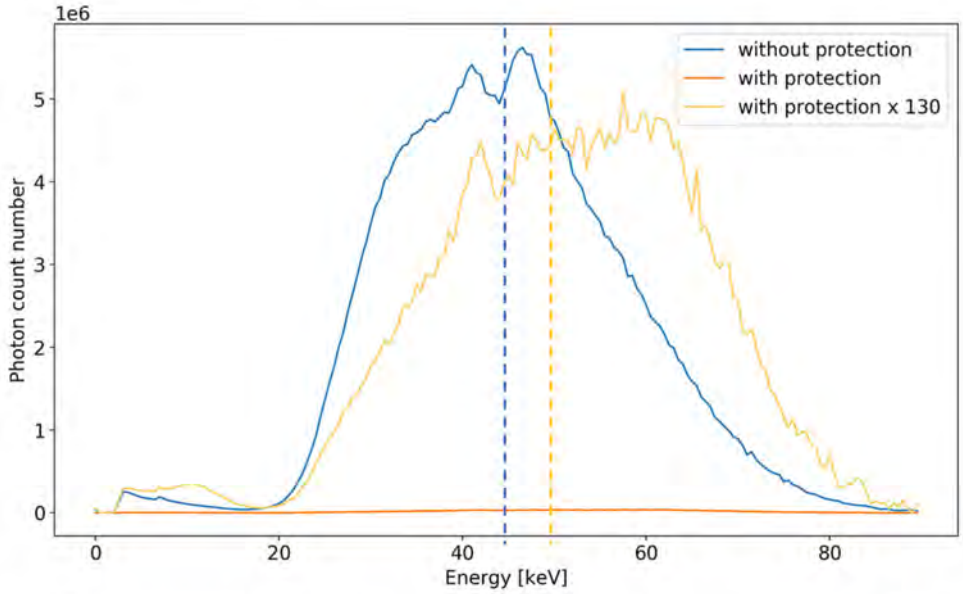

Figure 5. Energy spectra at 50 cm of the X-ray tube for an angle of 105° at 135 cm of height. Blue line represents the spectra without radiation protection gear, the orange line represents the spectra obtained with a lead screen and a lead table shield, the yellow line represents the data of the orange spectrum multiplied by 130. The dotted line represents the average energy.

The person in position A is the most exposed to ionizing radiations because of his or her proximity to the source of scattered radiation (*i.e.* the entry point of the primary beam in the patient body), even if standing right behind the protective shields (Fig. 3). The least exposed person is the one standing in the back of the theatre, at position D in Fig. 3.

In Fig. 4, the person at position A is less exposed at the level of the eye lens compared to the rest of the body. This can be explained by the fact that the person stands right behind the ceiling protective panels. Collected data also helps to highlight a shift in energy from head to toe at position A, indicating a non-homogenous exposure of the radiologist. The lower exposure level is observed at the level of the eye lens and the shift in energy indicates that if the eye lens dosimetry is performed using a dosimeter worn on the chest, the dose might be overestimated. A dedicated dosimeter would thus be recommended for a better monitoring.

Energy spectra show a more homogeneous exposure for staff standing in the back of the theatre, the spectra shape and fluence are very similar for eye lens, chest and belt. This can be explained by the fact that people stand

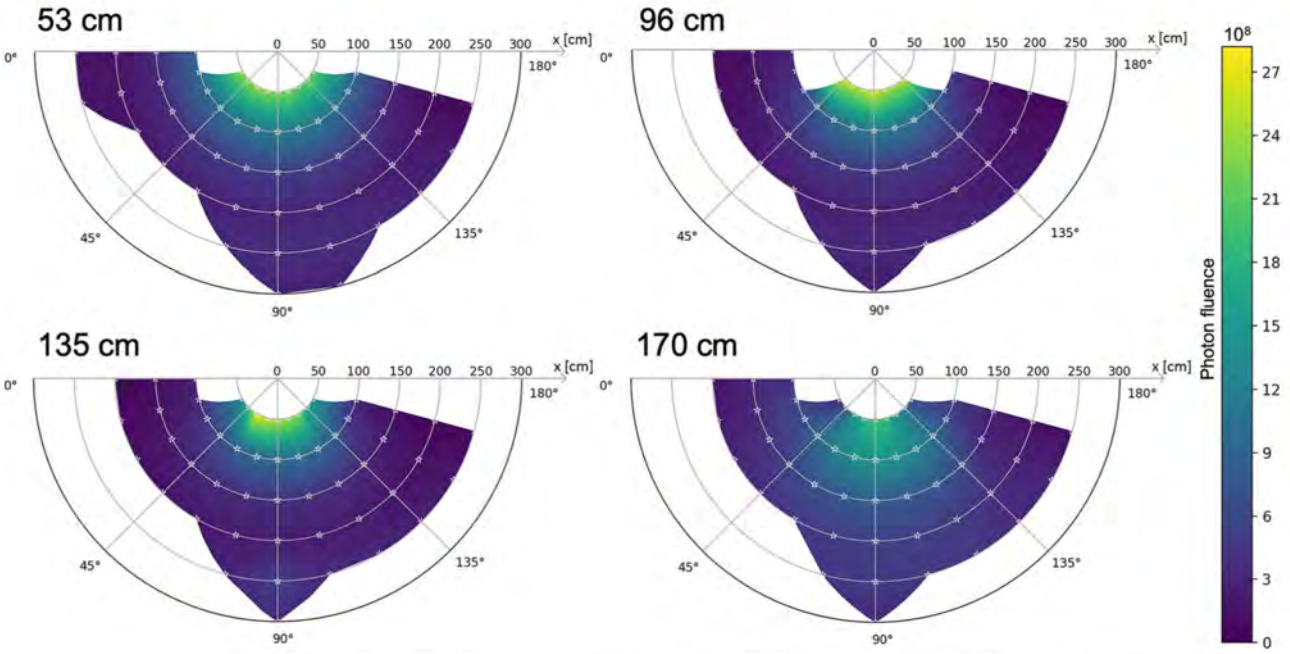

Figure 6. Colour maps of the photonic fluence in the theatre in the horizontal place at four heights, without collective protections.

farther away from the patient who generates the scattered radiation field. For those people, a dosimeter worn on the chest would provide a measurement that is representative of the whole body and of the eye lens exposure. Measured fluence above 74 keV can be due to pile up effect.

The highest exposure for position A and D is observed at the level of the knee. The same pattern was observed by Rehn[29] with a higher dose close at the knee level when using a C-arm tube, with the tube under the patient couch. An area with a higher scatter exposure rate is found close to the patient, in accordance with Fig. 6. The exposure of staff across a theatre shows that a dosimeter worn at chest level can overestimate the exposure of other organs (e.g. position C) or underestimate it (position A and B). The majority of workers are far from the annual dose limits. On the other hand, this could be a problem for a small fraction of workers, notably radiologists and cardiologists, who may reach dose limits on a dosimeter worn on the chest. Moreover, the articles of Ciraj-Bjelac et al.[30] and Hupe et al.[31] show that performance of many detectors decrease by using in pulsed field.

For pedagogical purposes, we investigated the effectiveness of the radiation protection gear. The use of a lead screen as well as a lead table shield reduces by more than a factor 130 the ionizing radiation field at chest level of a person standing 50 cm away from the tube at an angle of 105°. A spectrum hardening due to absorption by the protective material is clearly observed with a shift from a mean energy of 44 keV without the gear to 50 keV with gear (Fig. 5). Mori and McCaffrey[32,33] show that this difference in the mean energy can lead to a 12% higher X-ray transmission rate of protective aprons. Figure 5 was of particular interest when we presented the results to the staff and raised questions. It helped to increase awareness and understanding about radiation protection principles. In fact, the medical staff were interested to know how they could adapt their personal radiation protection gear, their positions in the room, or how to move or adapt the collective radiation protection gear. Medical staff were able to see and quantify the effectiveness of the protection, or the most irradiating position in the room. The radiation protection training program for the staff in IR in Lausanne University Hospital uses the DoseAware tool, and it is also very much appreciated by all participants. The Timepix chip shows great potential for offering further options and bringing additional information compared to other pedagogical tools available on the market. The Timepix3 chip provides information on the energy spectrum and opens possibilities to strengthen understanding of effective radiation protection. However, spectra presented are those measured by the sensitive layer of the detector and are not the energy spectra of the scattered radiation field in air. Full deconvolution of the spectrum will be needed before to relate to a dose. Experiences in classrooms have already demonstrated that the Timepix chip could be a valuable educational tool for learning about radiation[34,35]. Our experience demonstrates that the use of the chip as a pedagogical tool can be extended to the medical environment.

All data collected in the theatre was used to generate a coloured distribution map depicting the exposure levels in horizontal planes at four heights. As expected, the highest exposure levels were, for all four planes, next to the X-ray tube. The maximum exposure level was recorded on the horizontal plane at 135 cm (at chest level) on the left side of the tube, i.e. the side that is not covered by the protective gear. The radiologist stands on the right side, behind the gear. The exposure is higher on the two planes under the patient's bed where the tube is placed, as illustrated on the training video of the Federal office of public health in Switzerland[36]. The radiation distribution represents a specific distribution for the theatre in which we did the measurements and is an innovative and useful tool for the local radiation protection officer. The limitation of this study is the lack of measurements for other angles of the X-ray system.

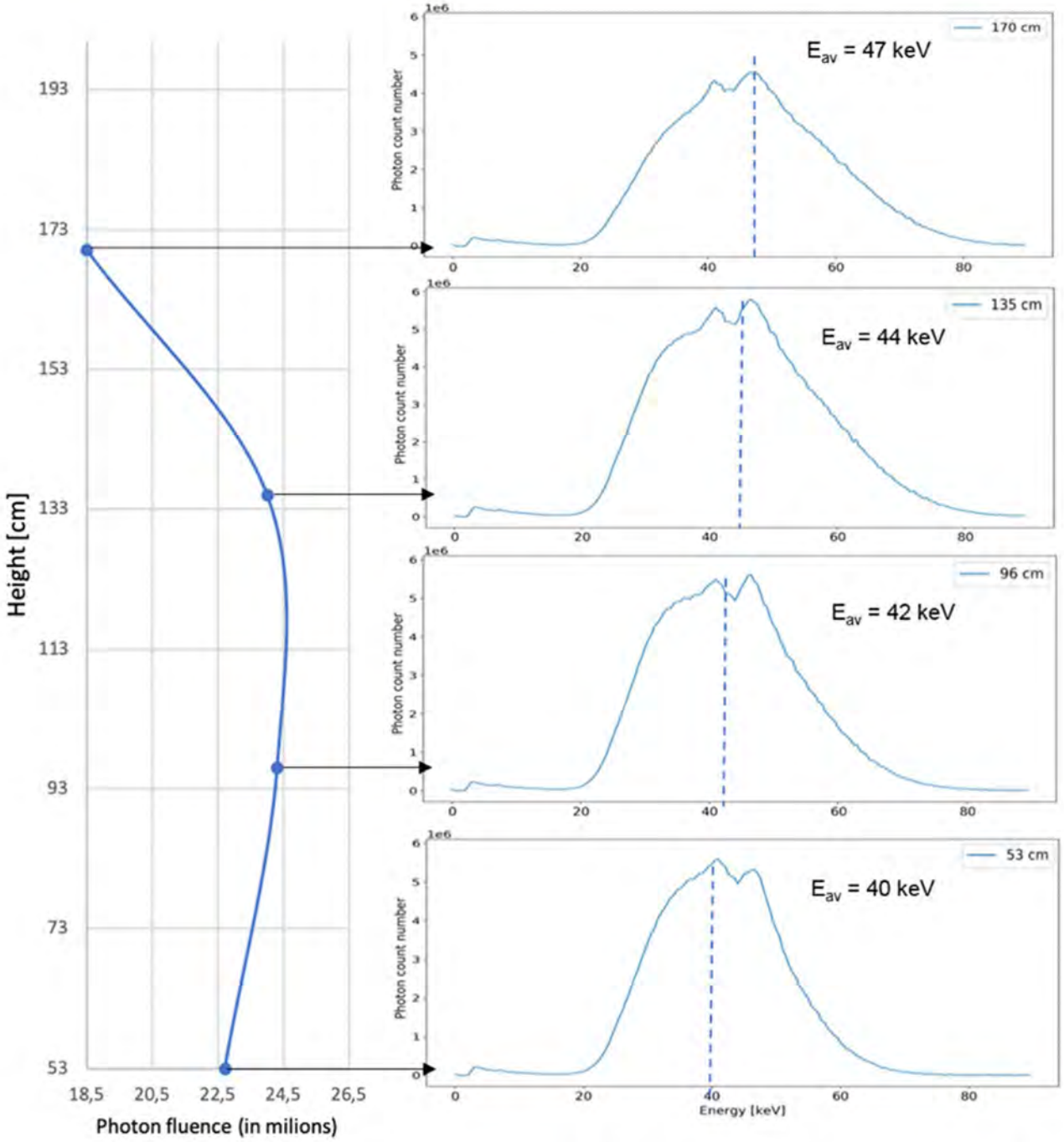

Figure 7. On the left part, the fluence multiplied by a factor energy-dependent as a function of the height, on the right part the energy spectra corresponding for each different height (from top to bottom: 170 cm, 135 cm, 96 cm, 53 cm). E_{av} represent the average energy.

Figure 7 shows that exposure to the body is height-dependent, therefore varies for the organs. The highest exposure for a person standing on the red star (see Fig. 2, right) is found at chest level. The shapes of the energy spectra are also different with the height. The maximum energy of the scattered radiation is higher at higher heights. Also, if the fluence for the eye lens is lower than for the rest of the body, the mean energy is higher. This information can be important since currently a chest dosimeter is considered sufficient to estimate eye lens exposure. But from this study we noticed the difference between all the energy spectra for different body parts. This confirms that the choice of the dosimeter position is important for an efficient dosimetry surveillance program. A dosimeter worn on the chest may not be representative of the eye lens exposure because of a different radiation exposure level and different energy spectrum.

If we consider the current dosimeters frequently used: TLD and OSL, their response in energy is not constant. TLDs present an energy response ranging from 0.8 to 1.5 up to 1000 keV[37], while OSL has a linear decreasing

response (from 1.07 to 0.85) between 0 and 120 keV[38]. The energy chosen for the calibration of the detector is important, as it is often very different from the energy received monthly. A correction factor must be taken into account[39]. However, this factor is based on an average theoretical energy received and not on the real exposure. In this sense, the Timepix3 brings a new performance and makes it possible to directly calibrate the detector for every possible energy.

Also, the energy correction factor may be different for the chest and the eye lens. A dedicated dosimeter may thus be recommended for eye lens exposure monitoring. Moreover, the radiation field becomes more homogenous the further from the patient while the dose rate decreases. The information collected with the Timepix3 chip in the theatre may also be important with respect to the new approach for dosimetry based on direct conversion coefficients given to the operational quantities from the fluence and energy. This provides us with new parameters for the radiation protection of medical staff.

Conclusion

Here we have demonstrated the feasibility of using the energy-resolving hybrid pixel detector, Timepix3, to measure X-ray information and characterize the scattered radiation field in an IR theatre. The radiation fields were characterised by measuring the fluence and energy spectra at different positions in an IR theatre. This new approach makes it possible to compare the different energy spectra to which staff members are exposed and thus guide the radiation protection officer in choosing appropriate radiation protection gear. As expected, the radiation fields to which members are exposed vary significantly with their position in the room. Moreover, for a given person, this new radiation detection technique provides information regarding the part of the body that is most exposed. The detector could also be used to correct practitioner practices, for example by accurately positioning the lead screens to improve their protection. Finally, the Timepix3 has demonstrated a great potential as a pedagogical tool to enhance understanding of the ionizing radiation hazards in an interventional theatre.

Received: 5 December 2019; Accepted: 30 September 2020
Published online: 30 October 2020

References

1. IXRPC. International recommendations for X-ray and radium protection. *Br. J. Radiol.* **7**, 695–699 (1934).
2. Stewart, F. A. *et al.* ICRP publication 118: ICRP statement on tissue reactions and early and late effects of radiation in normal tissues and organs–threshold doses for tissue reactions in a radiation protection context. *Ann. ICRP* **41**, 1–322 (2012).
3. Ciraj-Bjelac, O. *et al.* Occupational exposure of the eye lens in interventional procedures: how to assess and manage radiation dose. *J. Am. Coll. Radiol.* **13**, 1347–1353 (2016).
4. Minamoto, A. *et al.* Cataract in atomic bomb survivors. *Int. J. Radiat. Biol.* **80**, 339–345 (2004).
5. ICRP 2011 Statement on Tissue Reactions (n.d.)
6. Behrens, R. On the operational quantity Hp(3) for eye lens dosimetry. *J. Radiol. Prot.* **32**, 455–464 (2012).
7. ICRP. *Draft Joint Report of ICRU and ICRP for consultation: operational quantities for external radiation exposure.*
8. Racine, D. *et al.* Objective comparison of high-contrast spatial resolution and low-contrast detectability for various clinical protocols on multiple CT scanners. *Med. Phys.* **44**, e153–e163 (2017).
9. FOPH. *Audits in the OR-areas of Swiss Hospitals*. (2020).
10. Sánchez, R. M. *et al.* Staff doses in interventional radiology: a national survey. *J. Vasc. Interv. Radiol.* **23**, 1496–1501 (2012).
11. Silberstein, L. XXXIV. Spectral composition of an X-ray radiation determined from its filtration curve. *Lond. Edinb. Dublin Philos. Mag. J. Sci.* **15**, 375–394 (1933).
12. Mayneord, W. V. & Roberts, J. E. The "quality" of high voltage radiations. I.. *Br. J. Radiol.* **8**, 341–364 (1935).
13. Twidell, J. W. The determination of X-ray spectra using attenuation measurements and a computer program. *Phys. Med. Biol.* **15**, 529 (1970).
14. Sundararaman, V., Prasad, M. A. & Vora, R. B. Computed spectra from diagnostic and therapeutic X-ray tubes. *Phys. Med. Biol.* **18**, 208 (1973).
15. Stanton, L., Lightfoot, D. A. & Mann, S. A penetrameter method for field kV calibration of diagnostic X-ray machines. *Radiology* **87**, 87–98 (1966).
16. Peaple, L. H. J. & Burt, A. K. The measurement of spectra from X-ray machines. *Phys. Med. Biol.* **14**, 73 (1969).
17. Seelentag, W. W., Panzer, W., Drexler, G., Platz, L. & Santner, F. *A Catalogue of Spectra for the Calibration of Dosemeters*. https://inis.iaea.org/Search/search.aspx?orig_q=RN:11531730. (1979).
18. Birch, R. & Marshall, M. Computation of bremsstrahlung X-ray spectra and comparison with spectra measured with a Ge(Li) detector. *Phys. Med. Biol.* **24**, 505–517 (1979).
19. Castro, E. D., Pani, R., Pellegrini, R. & Bacci, C. The use of cadmium telluride detectors for the qualitative analysis of diagnostic X-ray spectra. *Phys. Med. Biol.* **29**, 1117–1131 (1984).
20. Miyajima, S., Imagawa, K. & Matsumoto, M. CdZnTe detector in diagnostic x-ray spectroscopy. *Med. Phys.* **29**, 1421–1429 (2002).
21. Medipix collaboration. Medipix website, *Medipix* (2017).
22. Llopart, X., Ballabriga, R., Campbell, M., Tlustos, L. & Wong, W. Timepix, a 65k programmable pixel readout chip for arrival time, energy and/or photon counting measurements. *Nucl. Instrum. Methods Phys. Res.* **581**, 485–494 (2007).
23. ADVACAM. ADVACAM: Imaging the unseen. https://advacam.com/.
24. Ballabriga, R. *The Design and Implementation in 0.13 um CMOS of an Algorithm Permitting Spectroscopic Imaging with High Spatial Resolution for Hybrid Pixel Detectors*. (Universitat Ramon Llull, 2009).
25. Jakubek, J. Precise energy calibration of pixel detector working in time-over-threshold mode. *Nucl. Instrum. Methods Phys. Res.* **633**, S262–S266 (2011).
26. Nowak, M., Tlustos, L., Carbonez, P., Verdun, F. R. & Damet, J. Characterisation of the impacts of the environmental variables on Timepix3 Si sensor hybrid pixel detector performance. *Nucl. Instrum. Methods Phys. Res.* **981**, 164502 (2020).
27. Marshall, N. W., Faulkner, K. & Warren, H. Measured scattered x-ray energy spectra for simulated irradiation geometries in diagnostic radiology. *Med. Phys.* **23**, 1271–1276 (1996).
28. Kalyvas, N. Measurement of scatter radiation spectrum from radiographic units. *Med. Phys.* https://doi.org/10.1594/ECR2013/C-0309 (2013).
29. Rehn, E. *Modeling of Scatter Radiation During Interventional X-ray Procedures* (Linköping University, Linköping, 2015).
30. Ciraj-Bjelac, O., Carinou, E. & Vanhavere, F. Use of active personal dosimeters in hospitals: EURADOS survey. *J. Radiol. Prot.* **38**, 702–715 (2018).

31. Hupe, O., Friedrich, S., Vanhavere, F. & Brodecki, M. Determining the dose rate dependence of different active personal dosemeters in standardized pulsed and continuous radiation fields. *Radiat. Prot. Dosimetry* https://doi.org/10.1093/rpd/ncz173 (2019).
32. Mori, H., Koshida, K., Ishigamori, O. & Matsubara, K. Evaluation of the effectiveness of X-ray protective aprons in experimental and practical fields. *Radiol. Phys. Technol.* **7**, 158–166 (2014).
33. McCaffrey, J. P., Tessier, F. & Shen, H. Radiation shielding materials and radiation scatter effects for interventional radiology (IR) physicians: Radiation shielding materials and radiation scatter for IR. *Med. Phys.* **39**, 4537–4546 (2012).
34. Bott, O. J., Dresing, K., Wagner, M., Raab, B.-W. & Teistler, M. Informatics in radiology: use of a C-arm fluoroscopy simulator to support training in intraoperative radiography. *RadioGraphics* **31**, E65–E75 (2011).
35. Loy Rodas, N. A global radiation awareness system using augmented reality and Monte Carlo simulations. *RadioGraphics* https://doi.org/10.1594/ECR2018/C-1615 (2018).
36. O. fédéral de la santé publique. Vidéos de formation pour les établissements médicaux. https://www.bag.admin.ch/bag/fr/home/gesetze-und-bewilligungen/gesuche-bewilligungen/bewilligungen-aufsicht-im-strahlenschutz/informationen-fuer-medizinische-betriebe/schulungsfilme-medizinische-betriebe.html.
37. Duggan, L., Hood, C., Warren-Forward, H., Haque, M. & Kron, T. Variations in dose response with x-ray energy of LiF:Mg, Cu, P thermoluminescence dosimeters: implications for clinical dosimetry. *Phys. Med. Biol.* **49**, 3831–3845 (2004).
38. Al-Senan, R. M. & Hatab, M. R. Characteristics of an OSLD in the diagnostic energy range: characteristics of OSLDs in diagnostic energy range. *Med. Phys.* **38**, 4396–4405 (2011).
39. Asahara, T. *et al.* Exposure dose measurement during diagnostic pediatric X-ray examination using an optically stimulated luminescence (OSL) dosimeter based on precise dose calibration taking into consideration variation of X-ray spectra. *Radiat. Meas.* **119**, 209–219 (2018).

Acknowledgement

The authors would like to thank the Medipix3 collaboration. Authors are grateful to the interventional radiology team of Christchurch Hospital—NZ, for their kindness, technical support, and help during measurements.

Author contributions

M.N. wrote the main manuscript text. M.N., P.C., F.R.V., J.D. conceived and designed the analysis. M.N., P.C., J.D. collected the data. M.K. contributed data and analysis tools. M.N. performed the analysis. All authors reviewed the manuscript.

Competing interests

The authors declare no competing interests.

Additional information

Correspondence and requests for materials should be addressed to M.N.

Reprints and permissions information is available at www.nature.com/reprints.

Publisher's note Springer Nature remains neutral with regard to jurisdictional claims in published maps and institutional affiliations.

Annex 1 - Dose definition

In radiation protection, the dose or absorbed dose corresponds to the energy deposited (ΔE) by the ionizing radiation per unit of mass (Δm). The dose unit is the Gray (Gy) which corresponds to joule per kg. The absorbed dose led to the quantification of the energy deposited in a tissue to determine the deterministic effect.

$$D = \frac{\Delta E}{\Delta m}$$

However, when ionizing radiation is only photonic (as is the case in IR suites), the dose becomes the integration on the energy spectrum of the energy fluence differential in energy ($\Psi_E(E)$) multiplied by the energy absorption coefficient ($\left(\frac{\mu_{ab}(E)}{\rho}\right)$). The mathematical definition of the dose can therefore be expressed as in Equation 2:

$$D = \int_0^{E_{max}} \Psi_E(E) \left(\frac{\mu_{ab}(E)}{\rho}\right) dE$$

With the energy fluence

$$\Psi_E(E) = \frac{d\phi}{dE}(E)\, dE$$

Where ϕ is the fluence.

As shown in Equation 3, calculating the dose requires knowledge of the energy of each photon. Knowledge of the energy spectrum of a radiation field is essential in order to be able to precisely calculate the dose.

1 Dose calculation

The quantity needed for radiation protection is derived from the absorbed dose. What follows hereafter is a proposal to explain how to obtain the effective dose from the ionizing radiation.

1.1 Equivalent dose

The equivalent dose H is a quantity that was introduced to take into account the effect of ionizing radiation on biological tissues, and thus take into consideration the stochastic health risk. The equivalent dose is equal to the absorbed dose (Equation 1), multiplied by a weighting factor (w_R) specific to the type and energy of the particles. The unit is the sievert (Sv).

$$H = \sum_R w_R D_R$$

The value of the weighting factors is re-evaluated as knowledge of the effects improve. The most recent values were published in 2007 in ICRP Publication 103 [80]. However, this dose does not take into account the tissue considered. Jacobi therefore introduced the concept of effective dose in 1975 [52], which was adopted by the ICRP in 1977 [81].

1.2 Effective dose

The effective dose is a radiation protection quantity providing indications on the stochastic health risk to the whole body. Effective dose was first introduced by the ICRP to set limits for radiation protection and not to estimate cancer risk from specific sources of radiation exposure [51].

The effective dose is the sum of the equivalent dose of all impacted tissues multiplied by the associated weighting factor (w_T).

$$E = \sum_T w_T \, H_T$$

Leading to

$$E = \sum_T \sum_R w_T \, w_R D_{R,T}$$

With T the fraction of the radiological risk associated with the tissue or organ considered. As for the equivalent dose, the unit is the Sv.

All weighting factors that are recommended by the latest ICRP publication were implemented in the revised Swiss Radiological Protection Ordinance [82].

Figure 28 gives a schematic representation of the link between the different quantities.

Figure 28 - Relation between ionising radiation and effective dose.

Annex 2 - Interaction of photon X-ray with matter

This section reviews two fundamental concepts: the cross-section and the photon beam attenuation, followed by the different processes of photon interaction with matter: the photoelectric effect, Compton scattering, pair production and Rayleigh scattering.
The probability of each process is dependent on the energy of the photon, and the atomic number (Z) of the medium crossed. Figure 29 represents the regions of relative predominance of the three main forms of photon interaction with matter.

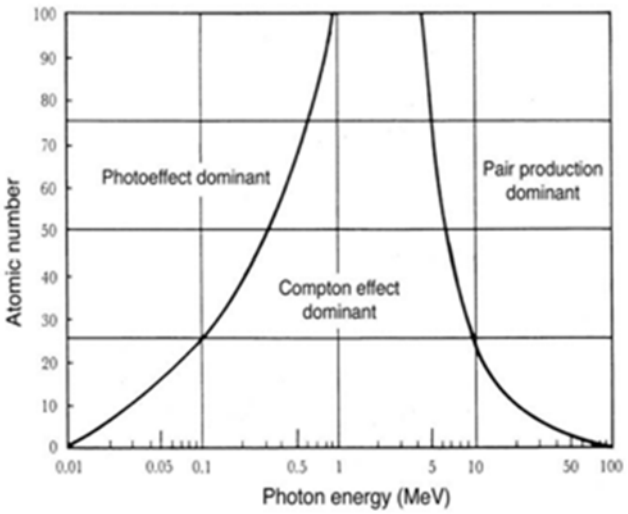

Figure 29 - Regions of predominance of photon interaction with matter. The left curve indicates that the cross-sections for the photoelectric effect and Compton effect are equal. The right curve indicates that the cross-sections for Compton effect and pair production are equal [83].

1 Photon beam attenuation

Photon beam attenuation is the progressive loss of energy of a beam through the matter. The intensity $I(x)$ of a narrow monoenergetic photon beam, attenuated by an attenuator of thickness x, is given as:

$$I(x) = I_0 e^{-\mu(h\nu,Z)x}$$

Where I_0 is the intensity of the beam before the attenuator and $\mu(h\nu, Z)$ is the linear attenuation coefficient, which depends on the energy of the photon $h\nu$, and the atomic number of the attenuator. This results in an exponential transmission curve for photon.

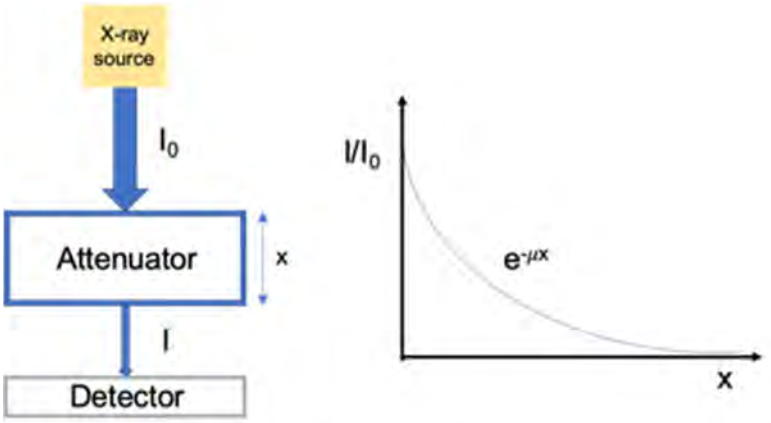

Figure 30 - On the left, photon beam attenuation. On the right, exponential transmission curve for photons.

2 Photoelectric effect

The photoelectric effect leads to the complete absorption of the incident photon by the substance subject to the action of radiation. When the photon collides with an electron of the interacting atom, the photon disappears, giving up all its energy to the environment. This energy is used to tear off the orbital electron and to eject it with a kinetic energy given as:

$$E_K = h\nu - E_b$$

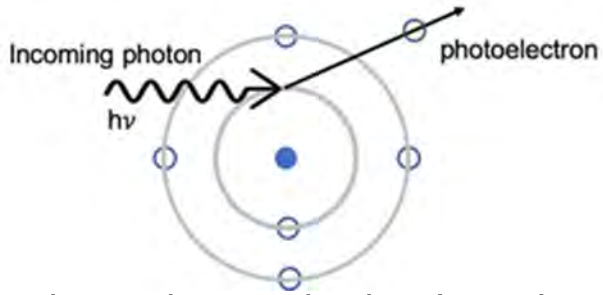

Figure 31 - Photoelectric absorption. The incoming photon hit an electron and ejects it as a photoelectron.

Where $h\nu$ is the incident photon energy and E_b is the binding energy of the electron. Here the atom is used to conserve momentum, this process cannot occur with a free electron.

After ejection of the orbital electron, a place is free on the atomic shell. An electron from an outer shell will fill this vacancy. The energy released is equal to the difference in bond between the electrons of the two shells and causes the emission of a photon or an electron. The emitted photon is called a characteristic X-ray. Its energy is determined by the shell and the atomic number of the atom. The electrons emitted after electronic rearrangement are called Auger electrons. Characteristic X-rays and Auger electrons are emitted isotropically.

The probability of the emission of a characteristic X-ray is called the fluorescence yield, ω. The fluorescence yield K decreases sharply with the decrease in the atomic number, and the fluorescence yields of the shells L and higher are considerably lower than those of the shell K. The values of the fluorescence K (ω_K) and the energies of the characteristic X-rays are given for some elements of the periodic table in Table *5*.
When an electron from a higher shell completes the K shell of a high atomic number atom, a cascade event can follow and leave the atom in a highly ionized state.

In general, the cross-section σ_{pe} for photoelectric absorption is inversely proportional to the energy of the photon. Figure 32 shows the cross-section for lead from a 10 keV to 10 MeV energy range photon.

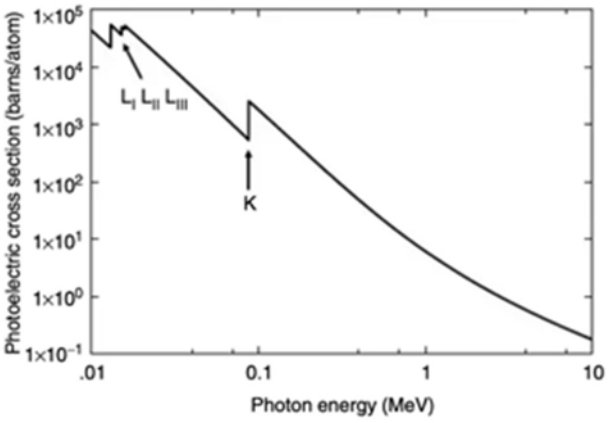

Figure 32 - The photoelectric cross-section as a function of the photon energy [83].

Table 5 – K-fluorescence yield and K X-ray energies for selected elements

Element	E_K (keV)
Ca	3.69
Ti	4.50
Mn	5.89
Cu	8.03
Zr	15.69
Mo	17.38
Ag	22.00
Sn	25.04

The cross-section for the photoelectric absorption effect is highly dependent on the atomic number. It increases to the fourth power of the atomic number and is inversely proportional to

the third power of the energy of the photon. The effect is more important at low energy and a high atomic number.

$$\sigma_{pe} \cong kZ^4 / (h\nu)^3$$

3 Compton scattering

Unlike the photoelectric effect where the photon disappears by giving up its energy to an electron, in the Compton effect, the photon partially transmits its energy to a target electron. The incident photon, of energy $h\nu$, strikes an electron of an atom, diffused with an energy $h\nu'$, lower than $h\nu$. The scattered photon is ejected with an angle θ, while the target electron is extracted from the procession at an angle φ and is called the Compton electron. This electron can ionize other atoms of the irradiated substance if its energy is sufficient.

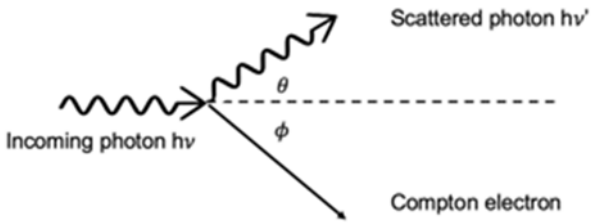

Figure 33 - Compton interaction. An incoming photon scatters to produce a scattered photon and a Compton electron.

The total cross-section for Compton scattering is known as the Klein and Nishina formula, and is obtained from integrating the differential Klein Nishina cross-section per electron:

$$\sigma_C = 2\pi r_e^2 \left(\frac{1+\alpha}{\alpha^2} \left[\frac{2(1+\alpha)}{1+2\alpha} - \frac{\ln(1+2\alpha)}{\alpha} \right] + \frac{\ln(1+2\alpha)}{2\alpha} - \frac{1+3\alpha}{(1+2\alpha)^2} \right)$$

Other effects like pair production or Rayleigh scattering are not presented in this work because the energy ranges used in this study do not produce its effects.

4 Interaction cross-section

The cross-section (σ) is a quantity expressing the probability of an interaction between two particles. In fact, photons can interact with different targets such as electrons, nuclei, atoms or molecules.

During interactions, photons generate absorbed or diffused processes. We speak of a full absorption process when the photon loses all of its energy, and this energy is transferred to the

target. This is the case, for example, during the photoelectric effect (σ_{pe}), the pair (σ_{pp}) or triplet (σ_{tp}) production. We speak of a full scattering process if the photon interacts with the target, but is not absorbed, the momentum and the energy of the photon can then be modified by respecting the laws of relativistic kinematics. We find this phenomenon during the Compton effect (σ_c), or the nuclear photo effect (σ_{phn}). The total interaction of the cross-section is the sum of the cross-sections for the phenomena taken individually.

$$\sigma = \sigma_{pe} + \sigma_c + \sigma_{pp} + \sigma_{tp} + \sigma_{phn}$$

5 Differential scattering cross section

In order to quantify some effects, the cross-section is considered a function of the solid angle (Ω). The differential cross-section is defined similarly to the total cross-section with $d\sigma/\mathrm{d}\Omega$ related to the probability that the photon diffuses through the solid angle dΩ. The differential scattering cross-section responds to the following equation:

$$\sigma = \int_{4\pi} \frac{d\sigma(\theta,\phi)}{\mathrm{d}\Omega}\mathrm{d}\Omega$$

Where θ is the scattering angle, and ϕ an azimuthal angle.

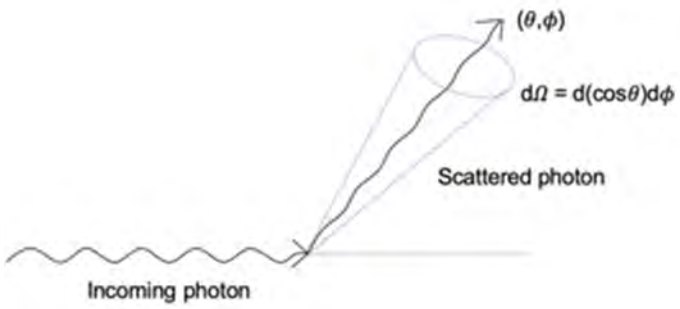

Figure 34 - Schema of the differential cross-section.

The cross-section has the dimensions of a surface. The probability of interaction of a given event depends on the particle, its energy, the intensity of the beam, the medium crossed, its thickness.

The total cross-section for silicon is represented by the following graph, where the sum of the contributions of the Compton (coherent and incoherent), as well as the photoelectric effect and the nuclear production pair is represented.

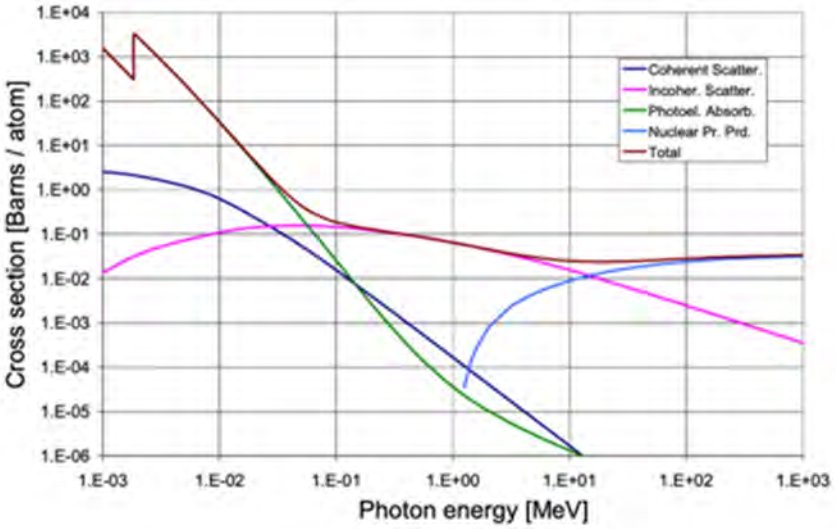

Figure 35 - Cross-section of silicon [84].

List of Publications

Thesis work publications:

Characterisation of the impacts of the environmental variables on Timepix3 Si sensor hybrid pixel detector performance

***M. Nowak**, L. Tlustos, P. Carbonez, F.R. Verdun, J. Damet*
Nuclear Instruments and Methods in Physics Research, November 2020,
doi: 10.1016/j.nima.2020.164502

Characterisation and mapping of scattered radiation fields in interventional radiology theatres

***M. Nowak**, P.Carbonez, M. Krauss, F.R. Verdun, J. Damet*
Scientific Reports, October 2020, doi: 10.1038/s41598-020-75257-5

Eye lens monitoring programme for medical staff involved in fluoroscopy guided interventional procedures in Switzerland

***M. Nowak**, M. Sans-Merce, C. Lemesre, R. Elmiger, J. Damet*
Physica Medica, January 2019, doi: 10.1016/j.ejmp.2018.12.001

Previous work:

Determination of the effective dose delivered by image guided radiotherapy in head & neck and breast treatments

*M. Conrad, G. Bolard, **M. Nowak**, B. De Bari, W. Jeanneret-Sozzi, J. Bourhis, J.F. Germond, F. Bochud, R. Moeckli*
Zeitschrift fur Medizinische Physik, December 2018, doi: 10.1016/j.zemedi.2018.01.001

Heat shock protein 70 regulates platelet integrin activation, granule secretion and aggregation

*A.R. Rigg, L.D. Healy, **M.S. Nowak**, J. Mallet, M.L. Thierheimer, J. Pang, O.J. McCarty, J.E. Aslan*
American Journal of Physiology - Cell Physiology, April 2016
doi:10.1152/ajpcell.00362.2015

Lysine acetyltransfer supports platelet function

*J.E. Aslan, R.A. Rigg, **M.S. Nowak**, C.P. Loren, S.M. Baker-Groberg, J. Pang, L.L. David, O.J. McCarty*
Journal of Thrombosis and Haemostasis, August 2015, doi: 10.1111/jth.13070

The BCR-ABL inhibitor ponatinib inhibits platelet immunoreceptor tyrosine-based activation motif (ITAM) signaling, platelet activation and aggregate formation under shear

*C.P. Loren, J.E. Aslan, R.A. Rigg, **M.S. Nowak**, L.D. Healy, A. Gruber, B.J. Druker, O.J. McCarty*
Thrombosis Research, January 2015, doi: 10.1016/j.thromres.2014.11.009

List of communications and conferences

Only posters and talks as a first author are indicated

Dosimetrie au cristallin

M. Nowak, N. Cherbuin, S. Medici, A Pitzschke, C. Lemesre, N. Meyer, J. Damet
Réunion annuelle d'information en radioprotection, Lausanne, 7 décembre 2016
(Oral communication)

Swiss approach for an eye lens monitoring programme for medical staff involved in fluoroscopy guided interventional procedures

M. Nowak, M. Sans-Merce, C. Lemesre, R. Elmiger, J. Damet
Groupe meeting FOHP, Bern, 28 February 2017
(Oral communication)

Preliminary results of the characterisation of scattered radiation field in interventional radiology theatres

M. Nowak, P. Carbonez, J. Damet
Interventional radiology group meeting Christchurch hospital, Christchurch - NZ, 8 December 2017
(Oral communication)

Characterisation of the radiation field for improved RP and dosimetry in IR theatres

M. Nowak, J. Damet, P. Carbonez
MARS Collaboration weekly meeting, Christchurch – NZ, 2 May 2018
(Oral communication)

Characterisation of scattered radiation field in interventional radiology theatres

M. Nowak, L. Tlustos, M. Campbell, P. Carbonez, F.R. Verdun, J. Damet
5th European IRPA congress, The Hague - NL, 4 – 8 June 2018
(Poster + pitch)

Characterisation of scattered radiation field in interventional radiology theatres

M. Nowak, L. Tlustos, J. Alozy, M. Campbell, P. Carbonez, J. Damet
Medipix meeting, Geneva, 19 September 2018
(Oral communication)

Characterisation of scattered radiation field in interventional radiology theatres

M. Nowak
Knowledge Transfer Seminars, Geneva, 16 October 2018
(Oral communication)

Characterisation of the radiation field for improved RP and dosimetry in IR theatres

M. Nowak, J. Damet, P. Carbonez
CERN Group meeting, Geneva, 25 October 2018
(Oral communication)

Energy spectrum map of the scattered radiation field in interventional radiology theatres with hybrid pixel detector

M. Nowak, P. Carbonez, F.R. Verdun, J. Damet
19th Solid State Dosimetry, Hiroshima - JP, 15 – 20 September 2019
(Poster + Oral communication)

Radiation field characterisation in hospital theatres using Timepix3 and eye lens dosimetry using Medipix3

M. Nowak
Knowledge Transfer Seminars, Geneva, 26 September 2019
(Oral communication)

Characterisation of the radiation field for improved RP and dosimetry in IR theatres

M. Nowak, J. Damet, P. Carbonez
EURADOS Working Group 12 (Dosimetry in medical imaging) meeting, Limerick - IE, 23 – 24 October 2019
(Oral communication)

Energy spectrum map of the scattered radiation field in interventional radiology with hybrid pixel detector

M. Nowak
CEA Leti, Grenoble - FR, 2 December 2019
(Oral communication)